



**University of
Zurich**^{UZH}

Re-analysis of ice deformation measurements in cold firn on Jungfraujoch

GEO 511 Master's Thesis

Author

Sarah Morard
15-211-915

Supervised by

Dr. Martin Lüthi

Faculty representative

Prof. Dr. Andreas Vieli

23.09.2020

Department of Geography, University of Zurich



**University of
Zurich** ^{UZH}

UNIVERSITY OF ZURICH
FACULTY OF SCIENCE
DEPARTMENT OF GEOGRAPHY

MASTER'S THESIS

**Re-analysis of ice deformation
measurements in cold firn on Jungfraujoch**

Sarah MORARD
Rte du Rawyl 16
3960 Sierre
sarah.morard@uzh.ch

Supervised by:
Dr. Martin LÜTHI

Zürich, the 22th September 2020

Abstract

The viscosity of ice plays a role in the flow processes of glaciers since the viscosity corresponds to the resistance of a material to flow. The viscosity depends on many parameters such as temperature and presence of water in the ice. Ice temperature is influenced by the increase of air temperature, especially for cold glaciers such as the ice cap of the Jungfrauoch. For temperate glaciers, the content of meltwater in ice accelerates the glacier flow and ice gets less viscous. In the 1950s, Prof. Haefeli was hired by the PTT for glaciological expertise during the construction of an ice gallery between the Jungfrauoch railway and the Ostgrat. During this period, he measured the deformations in different ice galleries and determined the ice viscosity. In this study, the deformations, measured in the 1950s, will be modelled with a creep model. This will be done with MOOSE, which uses the Finite-Element Methods.

Key words: cold ice, modelling, viscosity, Jungfrauoch, ice cap, MOOSE

Acknowledgements

I would like to thank Martin Lüthi for his help and his supervision during all the master's thesis. He always helped me and answered my questions. I would like to thank him to make me discover the secrets of the ice cap of the Jungfrauoch and its cold ice through the deformations in the ice gallery. I learned a lot. I would like to thank Andrea Walter and Diego Wasser for their help during the measurements at the Jungfrauoch. Further, I would like to thank the WGMS team (Michael Zemp, Samuel Nussbaumer, and Isabelle Gärtner-Roer) for answering my questions and adapting my internship to let me write my master's thesis. Finally, I would like to thank my father and my friends for their support.

Contents

1	Introduction	1
1.1	Introduction	1
1.2	Objectives	2
1.3	Research questions	2
1.4	Master's thesis structure	3
2	Theory	4
2.1	Glacial thermal regimes	4
2.1.1	Cold glacier	4
2.1.2	Temperate glacier	5
2.1.3	Polythermal glacier	5
2.2	Characteristics of glacier ice	5
2.2.1	Glacier ice	5
2.2.2	Movement of glacier ice	6
2.3	Stress, strain and strain rates	7
2.3.1	Stress	7
2.3.2	Strain	11
2.3.3	Strain rate	11
2.4	Rheology	12
2.4.1	Elasticity	12
2.4.2	Viscosity	13
2.4.3	Viscoelasticity	13
2.5	Collapse of a cylindrical hole	14
2.6	Modelling with MOOSE	14
2.6.1	Material	15
2.6.2	Modules/TensorMechanics/Master	16
3	Study site	17
3.1	Situation of the Jungfrauoch	17
3.2	Historical insight	17
3.3	Meteorological conditions	18
3.4	Particularity of the Jungfrauoch	19
3.5	Description of the infrastructure	22
3.6	Choice of the Jungfrauoch	26
4	Methodology	27
4.1	Deformation measurements	27
4.1.1	Description of the four circular profiles	27
4.1.2	Methodology	28
4.2	Temperature	31
4.3	Ice density	32
4.4	Modelling	32
4.4.1	Creation of the meshes for the circular profiles	32
4.4.2	Import of the mesh in MOOSE	33
4.4.3	Modelling	34
4.4.4	Comparison with the experimental data	34
4.4.5	Sensitivity of the parameters	35

5	Data	36
5.1	Profile K_1	36
5.1.1	Vertical deformation	37
5.1.2	Horizontal deformation	37
5.2	Profile K_2	37
5.2.1	Vertical deformation	38
5.2.2	Horizontal deformation	38
5.2.3	Oblique deformation	38
5.3	Profile K_3	40
5.3.1	Positions and displacements of the survey points	41
5.3.2	Vertical deformation	41
5.3.3	Horizontal deformation	41
5.3.4	Oblique deformation	41
5.4	Profile K_4	42
5.4.1	Positions and displacements of the survey points	43
5.4.2	Vertical deformation	43
5.4.3	Horizontal deformation	43
5.4.4	Oblique deformation	43
5.5	Temperature	44
5.5.1	Air temperature	44
5.5.2	Rock-ice contact temperature	44
5.5.3	Ice temperature	45
5.6	Ice density	47
5.7	Ice experiment	47
5.8	General data on the length of the galleries	48
5.9	Apparent viscosity	48
6	Results	50
6.1	Measurements	50
6.2	Influence of the parameters	51
6.2.1	Changing the width of the mesh	51
6.2.2	Changing Young's modulus	54
6.2.3	Changing n coefficient	56
6.2.4	Changing m coefficient	56
6.2.5	Changing A factor	60
6.3	Velocity in boundary conditions	63
6.4	Ice experiment	65
7	Analysis and discussion	66
7.1	Measurements	66
7.2	Influence of the parameters	67
7.2.1	Changing the width of the mesh	67
7.2.2	Changing Young's modulus	67
7.2.3	Changing n and m coefficient	67
7.2.4	Changing A factor	67
7.3	Velocity in BCs	68
7.4	Ice experiment	68
7.5	Modelling	68
7.5.1	Choice of the model	68
7.5.2	Choice of the units	69
7.5.3	Time steps	69
7.6	Density	69
7.7	Georeferencing	69
7.8	Discussion	69
8	Conclusion	71
	References	72

A Theory	75
A.1 Movement of glacier ice	75
A.2 Strain	76
A.3 Collapse of a cylindrical hole	76
B Study site	79
B.1 Particularity of the Jungfrauoch	79
B.2 Description of the infrastructure	81
B.3 Greenland	84
C Methodology	86
C.1 Profile K_3	89
C.2 Profile K_4	90
D Data	91
D.1 Profile K_1	91
D.1.1 Positions and displacements of the survey points	91
D.1.2 Vertical deformation	92
D.1.3 Horizontal deformation	92
D.1.4 Oblique deformation	93
D.2 Profile K_2	94
D.2.1 Positions and displacements of the survey points	94
D.2.2 Vertical deformation	95
D.2.3 Horizontal deformation	96
D.2.4 Oblique deformation	96

List of Figures

2.1	Snow crystals randomly stack up (left). The thermal gradient and the pressure, which are undergone by the névé, recrystallize the névé crystals and reorganize them (middle). Glacier ice shears under the basal planes when it flows (right). The top and the bottom of the ice crystal are called basal plane and the six faces of the ice crystal are called prismatic planes.	6
2.2	Graphical representation of the velocity vectors \vec{U}_{in} and \vec{U}_{out} (eq. A.1.1)	7
2.3	Representation of the shear stress in a plane yz . The velocity \vec{v} behaves differently according to the depth. There is more deformation at the surface than at the bottom. According to Hooke (2005, page 88), "the vertical velocity decreases linearly with depth".	7
2.4	Left: Representation of the different stresses in 2D (xz -plane). Right: Infinitesimal representation of the different stresses of the glacier in 3D	8
2.5	This graph represents the rate of contraction according the pressure in ice galleries	9
2.6	This graph represents the B according to different temperatures. They measured or estimated the minimum strain rate to determine the B factor. The upper dashed line gives strain rates double those of the strain rates represented by the solid line. The lower dashed line gives strain rates half those of the strain rates represented by the solid line.	10
2.7	Map of different deformations according to ice temperature and octahedral stress (Hooke, 2005, Fig. 4.16, page 64). This map was tested for a ice grain with a size of 1mm.	10
2.8	A factor at different temperatures with $n=3$	11
2.9	This graph represents the strain rate according to different temperatures. The stress remains constant during the experiment.	12
2.10	Stresses on the wall of a cylindrical hole in a weightless medium (adapted from Hooke (2005, Fig. 12.1, page 316 (left) and Fig. 12.2, page 317 (right))	14
3.1	Geographical situation of the Jungfrauoch and location of the main ice gallery. . .	17
3.2	Air temperature at Sphinx for 1950-1959 (blue line) and for 2010-2019 (orange line)	18
3.3	Different dividing lines in the ice cap of the Jungfrauoch	20
3.4	Infrastructures at the Jungfrauoch	21
3.5	Principal gallery	22
3.6	Principal gallery in 2019/2020	22
3.7	Horizontal displacement of the main tunnel axis	23
3.8	Tension zone and compression zone in the main tunnel	24
3.9	Simplified schema of the transversal Q100 with the velocity profiles at different locations in the ice cap and the tension distribution in the ice cap	25
4.1	Circular profile K_4 taken from the entrance of the gallery	28
4.2	Circular profile K_4 taken from the entrance of the gallery. Zoom on the survey points 2, 3, 5 and 6.	29
4.3	Ice temperature measurements in the wall and in the bottom of the main ice gallery	31
4.4	Mesh for the circular profile K_1 with a width of 60m.	33
4.5	Square mesh at the timestep $t=0.1$ year	34
4.6	Hole of the ice gallery. The points represent the nodes. The red line and points represent the horizontal deformation. The yellow line and points represent the vertical deformation.	34
5.1	Circular profile K_1 at three different time periods (20.02.1951, 13.09.1951, 08.01.1953)	36

5.2	Circular profile K_2 at four different time periods (29.08.1954, 04.11.1954, 06.09.1955, 07.02.1956)	38
5.3	Circular profile K_3 at two different time periods (04.12.2019 and 06.02.2020) . . .	40
5.4	Circular profile K_4 at two different time periods (04.12.2019 and 06.02.2020) . . .	42
5.5	Air temperature in the main ice gallery at the positions hm 1.00	45
5.6	Rock-ice contact temperature in the borehole at position hm 0.4 from 17.10.1958 to 10.11.1958	45
5.7	Temperature in the boreholes B1 to B10 from 31.10.1958 to 15.02.1959 in the rock	46
5.8	Temperature in the borehole B3 at different depth (0m = rock surface, 5m, 10m, and 15m = ice thickness above the rock)	46
5.9	Temperature in the ice walls on 17.10.1958 and 10.12.1958. Point 0m is the borehole B1. Negative values for x-axis are west of the ice gallery. Point -20m is the end of the ice gallery. Point 275m is the entrance of the ice gallery.	46
5.10	Temperature in the ice walls and ice gallery bottom on 06.02.2020 at different positions	47
5.11	Ice sample with a load of $\sigma = 1 \text{ kg/cm}^2$	47
5.12	Relation between the pressure and the specific strain rate for different load (1 kg/cm^2 , 3 kg/cm^2 , and 4 kg/cm^2)	48
6.1	Measurements for the four circular profiles (K_1 , K_2 , K_3 , and K_4)	50
6.2	Different modellings for the circular profile K_1 with different mesh widths (60m, 100m, and 120m)	52
6.3	Different modellings for the circular profile K_2 with different mesh widths (60m, 100m, and 120m)	52
6.4	Different modellings for the circular profile K_3 with different mesh widths (10m, 20m, 60m, and 100m)	53
6.5	Different modellings for the circular profile K_4 with different mesh widths (10m, 20m, 60m, and 100m)	53
6.6	Different modellings for the circular profile K_1 with different Young's modulus (8.7, 87, 870, and 8700)	54
6.7	Different modellings for the circular profile K_2 with different Young's modulus (8.7, 87, 870, and 8700)	55
6.8	Different modellings for the circular profile K_3 with different Young's modulus (8.7, 87, 870, and 8700)	55
6.9	Different modellings for the circular profile K_4 with different Young's modulus (8.7, 87, 870, and 8700)	56
6.10	Different modellings for the circular profile K_1 with different n coefficients (3 and 4)	57
6.11	Different modellings for the circular profile K_2 with different n coefficients (3 and 4)	57
6.12	Different modellings for the circular profile K_3 with different n coefficients (3 and 4)	58
6.13	Different modellings for the circular profile K_4 with different n coefficients (3 and 4)	58
6.14	Different modellings for the circular profile K_1 with different m coefficients (0, 1, 2, and 3)	59
6.15	Different modellings for the circular profile K_2 with different m coefficients (0, 1, 2, and 3)	59
6.16	Different modellings for the circular profile K_3 with different m coefficients (0, 1, 2, and 3)	60
6.17	Different modellings for the circular profile K_4 with different m coefficients (0, 1, 2, and 3)	60
6.18	Different modellings for the circular profile K_1 with different A factors (10, 30, 50, and 65)	61
6.19	Different modellings for the circular profile K_2 with different A factors (10, 30, 50, and 65)	61
6.20	Different modellings for the circular profile K_3 with different A factors (10, 30, 50, and 65)	62
6.21	Different modellings for the circular profile K_4 with different A factors (10, 30, 50, and 65)	62
6.22	Modellings of the circular profile without and with velocity applied to boundary conditions (Profile K_1 .)	63
6.23	Modellings of the circular profile without and with velocity applied to boundary conditions (Profile K_2 .)	64
6.24	Modellings of the circular profile without and with velocity applied to boundary conditions (Profile K_3 .)	64

6.25	Modellings of the circular profile without and with velocity applied to boundary conditions (Profile K_4 .)	65
6.26	Results from the modelling for an ice sample with a load of $\sigma = 1kg/cm^2$	65
A.1	Representation of the velocity u in a cylindrical hole (adapted from Hooke (2005, Fig. 12.3, page 318))	77
B.1	Applied stresses (σ_x , σ_y and σ_z) in the three directions (resp. x-, y- and z-direction) in the ice cap of the Jungfraujoeh	79
B.2	Emptying of a water-filled crevasse on 06.02.2020 (photo taken by S. Morard) . . .	80
B.3	Schema of the transversal tunnel Q120	81
B.4	Schema of the transversal tunnel Q120 in the ice cap	81
B.5	Schema of the transversal tunnel Q100	82
B.6	Crevasse	82
B.7	Position of the different boreholes. In the figure A), the borehole B9 situates 4.9m south of the borehole 3. The bedrock shape for the three figures dates from 1950/51. The boreholes B1 to B11 reach the bedrock.	83
B.8	Location of the boreholes B1 to B10	84
B.9	Measurements at the Station Centrale	85
C.1	Code of the mesh, written by Martin Lüthi, for the circular profile K_1 with a width of 60m.	86
C.2	Part of the model used for the results of Chapter 6.2. The block PostProcessor is missing in the script here.	87
C.3	Part modified of Fig. C.2 for the results of Chapter 6.3.	88
C.4	Model used for the ice experiment.	89

List of Tables

4.1	Summary of the mesh size	32
5.1	Profile K_1 : Measured vertical deformation from 20.02.1951 to 08.01.1953	37
5.2	Profile K_1 : Measured horizontal deformation from 20.02.1951 to 08.01.1953	37
5.3	Profile K_2 : Measured vertical deformation from 09.09.1955 to 15.04.1957	39
5.4	Profile K_2 : Measured horizontal deformation from 04.11.1954 to 15.04.1957	39
5.5	Profile K_2 : Measured oblique deformation between the survey points 1 and 4 from 04.11.1954 to 15.04.1957	39
5.6	Profile K_2 : Measured oblique deformation between the survey points 2 and 6 from 04.11.1954 to 15.04.1957	40
5.7	Profile K_3 : Coordinates, displacements and velocity of displacements of the survey points of the circular profile K_3 at two different time periods (04.12.2019 and 06.02.2020)	41
5.8	Profile K_3 : Measured vertical deformation from 04.12.19 to 06.02.20	41
5.9	Profile K_3 : Measured horizontal deformation from 04.12.19 to 06.02.20	41
5.10	Profile K_3 : Measured oblique deformation from 04.12.19 to 06.02.20	42
5.11	Profile K_3 : Measured oblique deformation from 04.12.19 to 06.02.20	42
5.12	Profile K_3 : Measured oblique deformation from 04.12.19 to 06.02.20	42
5.13	Profile K_4 : Coordinates, displacements and velocity of displacements of the survey points of the circular profile K_4 at two different time periods (04.12.2019 and 06.02.2020)	43
5.14	Profile K_4 : Measured vertical deformation from 04.12.19 to 06.02.20	43
5.15	Profile K_4 : Measured horizontal deformation from 04.12.19 to 06.02.20	43
5.16	Profile K_4 : Measured oblique deformation from 04.12.19 to 06.02.20	44
5.17	Profile K_4 : Measured oblique deformation from 04.12.19 to 06.02.20	44
5.18	Profile K_4 : Measured oblique deformation from 04.12.19 to 06.02.20	44
5.19	Apparent viscosity in the main gallery determined from the change in the width of the gallery from 13.11.1953 to 22.01.1954, from 22.01.1954 to 22.07.1955, and from 22.07.1955 to 17.10.1956	49
6.1	Comparison between the different measurements of each circular profile (K_1 , K_2 , K_3 , and K_4)	50
6.2	B and A factors for the different circular profiles. T_p are temperature values taken from Paterson (1999) and T_{CP} are temperature values taken from Cuffey and Paterson (2010).	51
C.1	Profile K_3 : Mean measurements of distance from 04.12.19 to 06.02.20	89
C.2	Profile K_4 : Mean measurements of distance from 04.12.19 to 06.02.20	90
D.1	Coordinates of the survey points of the circular profile K_1 at three different time periods (20.02.1951, 13.09.1951, 08.01.1953).	91
D.2	Profile K_1 : Displacements, velocity of displacement of each survey points from 20.02.1951 to 13.09.1951.	91
D.3	Profile K_1 : Displacements, velocity of displacement, strain and strain rate of each survey points from 13.09.1951 to 08.01.1953.	92
D.4	Profile K_1 : Displacements, velocity of displacement, strain and strain rate of each survey points from 20.02.1951 to 08.01.1953.	92
D.5	Profile K_1 : Vertical deformation determined from the digitization from 20.02.1951 to 08.01.1953	93

D.6	Profile K_1 : Horizontal deformation determined from the digitization from 20.02.1951 to 08.01.1953	93
D.7	Profile K_1 : Oblique deformation determined from the digitization from 20.02.1951 to 08.01.1953	94
D.8	Coordinates of the survey points of the circular profile K_2 at four different time periods (29.08.1954, 04.01.1954, 06.09.1955, 07.02.1956).	94
D.9	Profile K_2 : Displacements and velocity of displacement of each survey points from 29.08.1954 to 04.11.1954.	94
D.10	Profile K_2 : Displacements and velocity of displacement of each survey points from 04.11.1954 to 06.09.1955.	95
D.11	Profile K_2 : Displacements and velocity of displacement of each survey points from 06.09.1955 to 07.02.1956.	95
D.12	Profile K_2 : Displacements and velocity of displacement of each survey points from 29.08.1954 to 07.02.1956.	95
D.13	Profile K_2 : Vertical deformation determined from the digitisation from 04.11.1954 to 07.02.1956	96
D.14	Profile K_2 : Horizontal deformation determined from the digitisation from 29.08.1954 to 07.02.1956	97
D.15	Profile K_2 : Oblique deformation determined from the digitization from 04.11.1954 to 07.02.1956	97
D.16	Profile K_2 : Oblique deformation determined from the digitisation from 29.08.1954 to 07.02.1956	97

Glossary

CTS Cold-temperate Transition Surface. 5

FEM Finite-Element Methods. 14, 15

MOOSE Multiphysics Object-Oriented Simulation Environment. 2, 15, 16, 33–35, 67–69, 71

NTC Negative Temperature Coefficient. 31

PTT Postal, Telegraph, and Telephone. 2, 17, 18, 23

Chapter 1

Introduction

1.1 Introduction

Viscosity corresponds to the resistance of a material to flow (Barnes et al., 1989). Since the viscosity of ice impacts the flow properties of glaciers (Deeley & Parr, 1913), a better knowledge of viscosity plays a significant role in the understanding of glacier motion (Fowler, 1997). So, the flow properties of glaciers and ice sheets can be described with the flow properties of highly viscous fluids (Fowler, 1997; Perutz, 1947). To give some idea of comparative orders of magnitude, the viscosity of ice is approximately more than 10^{12} Pa·s. Ice is 10^{15} times more viscous than water¹. The glacier motion can be compared to a river that flows very slowly due to its large viscosity (Fowler, 1997).

The apparent viscosity of ice depends on many factors, such as the temperature (Deeley & Parr, 1913; Höppler, 1941), the applied shear stress, and the crystal orientation (Höppler, 1941). Deeley and Parr (1913) hypothesized in some experiments² that a colder temperature implied a larger viscosity. It had been noticed that the Hintereis glacier moved faster in summer than in winter (Deeley & Parr, 1913). Weinberg (1907) explained this phenomenon by the presence of water in the upper part of the glacier tongue. The water resulted from the melt of ice and snow at the surface of the glacier. Perutz (1947) also declared that the viscosity was considerably reduced by water. The water weakens the resistance between the ice crystals. These observations emphasize the influence of the ice temperature on the ice viscosity. Different viscosities in the glacier can be detected at different depths in summer, and viscosity is different in winter and summer due to seasonal thermal change (Deeley & Parr, 1913). Many experiments were conducted by Höppler (1941) to determine the dependence of the viscosity with the temperature, the applied shear stress, and the crystal orientation. He concluded that the viscosity of ice at -20°C was 1000 times greater than at a temperature of -1°C with a constant shear stress. The viscosity for a shear stress of $10 \frac{\text{kg}}{\text{cm}^2}$ was 200 times smaller than the viscosity for a shear stress of $63 \frac{\text{kg}}{\text{cm}^2}$ at a constant temperature. In a preferred crystal orientation with crystal glide planes parallel to the direction of shear was the apparent viscosity 70 times greater than in case of no preferred crystal orientation. Nevertheless, Perutz (1947) reproached Höppler that its experiments did not determine the viscosity at the pressure melting point. Moreover, Perutz (1947) assumed a change in viscosity according to the depth due to hydrostatic pressure, which was not considered by Höppler (1941). Perutz (1947) and Deeley and Parr (1913) stated that the plastic behavior of glaciers ensued from the regelation, and Perutz (1947) added that the “relative motion of individual ice crystals plays” a role in the plastic behavior of glacier.

In the 1950s, continuous measurements were undertaken inside of the tunnels excavated in the ice cap at the Jungfraujoch to determine the ice motion, the deformations, and the viscosity conditions in cold ice. These measurements aimed to get a better understanding of the motion processes. Moreover, they investigated the temperature distribution along a vertical profile in the ice cap. The ice cap behaves differently than other Alpine temperate glaciers due to its cold ice. Cold ice is more brittle and less plastic than temperate ice. The length changes and the deformations observed in the different ice tunnels enabled the analysis of the plastic behavior of the ice. They tried during this period to explain qualitatively the deformations, the fissures, and the

1. Water viscosity is $1.8 \cdot 10^{-3}$ Pa·s at 0°C (CRM, 2012, page 172).

2. For more details, read the paper of Deeley and Parr (1913).

observed crevasses in the ice cap. The results of these measurements could be compared with the one done in the ice caps of the Arctic and the Antarctic. Another characteristic of the ice cap at the Jungfrauoch is its flow separation. A part of the ice flows in the northern direction and the other part in the southern direction (Haefeli & Brentani, 1955).

The measurements, the observations, and the investigation of the viscosity conditions in cold ice ensued from the building of a relay station in the 1950s by the PTT (Postal Telegraph and Telephone, now Swisscom) (Volmar, 1962) at 3'750 m. a.s.l. (Ostgrat) (Wegmann, 1998). An access tunnel was built to link the Jungfrauoch railway station to the relay station. In October 1950, a water-filled crevasse threatened the main tunnel. This crevasse was not apparent from the surface and should be drained. For one of these reasons, they installed two cross-tunnels. The formation of a possible longitudinal crevasse would be rapidly observable, and so they could quickly react if water was filling a crevasse (Haefeli & Brentani, 1955).

Since the completion of the railway to the Jungfrauoch (3'454 m a.s.l) in 1912 (Jungfrau, 2019), the Jungfrauoch railway has directly been a tremendous success (Volmar, 1962). Its construction was a technical challenge due to the topography, the technical, environmental, and financial difficulties. In the beginning, the project planned to reach 4'100 m a.s.l., but due to a financial motive, this idea was later abandoned (Volmar, 1962). The railway has facilitated access to the high alpine environment, and it was an advantage for research and science. It was possible to install a research station (HFSJG, 2019) and to reach it by train. During the general meeting of May 14th, 2018 (Jungfrau Holding AG, 2018) Jungfraubahn decided to extend the tour from the Jungfrauoch station up to the Ostgrat. The project realization will be on a time horizon of 2030 (Jungfrau Holding AG, 2018). One possibility to transport all the future tourists from the Jungfrauoch up to the Ostgrat is to reuse the ice tunnel constructed in the 1950s by the PTT.

Investigating the viscosity of glaciers is relevant because it gives a better understanding of the flow properties of glaciers and will enable to determine the motion of glaciers. Moreover, the glaciers react to temperature changes, and their viscosities also change. Deeley (1908) declared that ascertaining the glacier viscosity was complicated. Then, the Jungfrauochbahn SA plans to build transport for tourists in this ice tunnel. It is necessary to have a better understanding of the ice behavior in the ice tunnel for the infrastructures. Nye (1953) stated that the tunnels would close up if there was any artificial support under the pressure of the overlying ice and added that "their rate of collapse is directly related to the flow law ice" (Nye, 1953). A comparison with the past measurements and the present situation can be achieved. Since the shear stress varies with the ice overlying layer thickness and the temperature change, it might be possible to estimate the impact on the shear stress.

1.2 Objectives

The main goal of this master's thesis is to evaluate the ice deformation measurements from the 1950s with today's possibilities of highly detailed ice flow models. This will be realized with MOOSE (Multiphysics Object-Oriented Simulation Environment), which "is a finite-element, multiphysics framework" (MOOSE Framework, 2020).

Firstly, the experiment, done by Haefeli (1963, page 172), will be reproduced. It is a uniaxial compression on an ice cylinder realized in the ice laboratory. Then, the experiment done in the past by Haefeli and Brentani (1955) will be reproduced with an ice flow model by modeling the figure 8 of the report of Haefeli and Brentani (1955, page 403), and for the three other profiles measured in the ice galleries between 1950 and 2020.

1.3 Research questions

As seen in chapter 1.1, there are no studies on the modelling of past experiments done at the Jungfrauoch, and the gathered data have not been investigated more in detail nowadays. Moreover, viscosity depends on many factors, and comparing two different periods can emphasize the effects and the influence of these factors on viscosity.

The research questions governing this master's thesis for the modelling of ice tunnels at the Jungfrauoch are:

- Which ice rheological parameters are suitable to reproduce the measured deformations of the ice tunnels at the Jungfraujoch?
- What differences and similarities are there between the observations and interpretations done 70 years ago and the results of the model?
- How does the glacier flow in the ice tunnels in the Jungfraufirn?

A summary of the different reports will be realised to have a better understanding of the processes in the ice cap. To answer these different questions, a model will be created. Then, different parameters will be tuned to reproduce the measured vertical and horizontal deformations. Finally, the values will be compared and interpreted.

1.4 Master's thesis structure

This thesis's master has been divided into 8 parts. The function of each chapter is explained below.

The first chapter *Introduction* introduces the subject and the current knowledge in the scientific literature. It states the problem and presents the research questions developed in this study.

The second chapter *Theory* defines the theoretical concepts to understand the processes involved in the modeling part and to interpret the data and the results.

The third chapter *Study site* describes the Jungfraujoch area, the different galleries, and the infrastructure. It also describes the particularity of the Jungfraujoch ice cap. It summarises the different reports of the 1950s.

The fourth chapter *Methodology* describes and explains how the measurements were carried out, how the data were gathered, and how the galleries were modelled.

The fifth chapter *Data* presents and describes the different data gathered and useful for the modelling.

The sixth chapter *Results* presents and describes the results obtained in the modelling.

The seventh chapter *Analysis* analyses the data, the results, the model, and the modelling.

The eighth chapter *Conclusion* resumes the thesis's master and conclude the research.

Chapter 2

Theory

2.1 Glacial thermal regimes

Climatic variations change the glacier size and volume. This change in the mass is visible by the retreating of glaciers or by their advance. Climatic variations also change the internal temperature and liquid water content. This change in the internal energy influences the glacial dynamic and the internal hydrology (Gilbert, 2013). The internal temperature, namely the thermal structure of a glacier, depends on the heat balance (Paterson, 1994; Gilbert, 2013), which is controlled by intrinsic and extrinsic factors (Paterson, 1994), through the processes of conduction, advection, and latent heat transfer (Paterson, 1994; Gilbert, 2013) on different time scales (Irvine-Fynn et al., 2011, page 3). The thermal response time for large ice masses is longer compared to the environmental change. Irvine-Fynn et al. (2011, page 3) emphasize that “the thermal structure of a polar ice mass has a significant memory that is largely inherited”. The thermal regime influences the ice quality and characteristic (Gilbert, 2013). To gain some knowledge on the thermal regime of a glacier is important due to the close connection between the temperature and the deformation rate of ice. For example, if the ice is cooling from $-10^{\circ}C$ to $-25^{\circ}C$, the viscosity increases by a factor of five. Moreover, a change in the thermal state of a glacier affects its advance. For example, if the bed was in the past frozen, the glacier starts to slip when the ice at its base reaches the melting point. The ice surface temperature is determined by the climate. Moreover, ice deformation and refreezing of meltwater warm the interior of the glacier (Cuffey & Paterson, 2010) due to the latent heat¹. Many factors depend indirectly on temperature such as density (Cuffey & Paterson, 2010), snow texture² (Adams & Sato, 1993), thermal and mechanical properties of firn, viscosity, deformation rates, and flow field (Lüthi & Funk, 2001). The response time of glacier surface temperature to the air temperature variations is not linear (Gilbert, 2013). “From 10-15m depth, the ice temperature is no more sensitive to the intra-annual variability of surface temperature” (Gilbert, 2013, page 37, translated from the French). The energy balance influences the temperature response when this latter is modified by percolation, by freezing of meltwater, or by reaching the melting point (Gilbert, 2013).

Glacial thermal regimes determine the ice temperature and the liquid water content of a glacier. It exists three types of thermal regimes: cold, temperate, and polythermal (Gilbert, 2013; Cuffey & Paterson, 2010; Irvine-Fynn et al., 2011). Knowing the thermal regime of a glacier gives a source of information about the quality of the ice and the available quantity in water.

2.1.1 Cold glacier

Cold ice is when glacier ice is below the melting point (Irvine-Fynn et al., 2011; Greve & Blatter, 2009; Cuffey & Paterson, 2010). The glacier is called cold glacier (Greve & Blatter, 2009). The rock substrate is considered as frozen, which ensures a “high adhesive strength” (Irvine-Fynn et al., 2011, page 3), and it implies no basal slide (Hooke, 2005). If the ice is below but close to the melting point, it means temperatures between $-3^{\circ}C$ and $-1^{\circ}C$, a climatic variation could change the thermal regime in some years or maybe decades. Cold glacier can transform in temperate glacier (Gilbert, 2013) (see chapter 2.1.2). “Small and cold high-altitude glaciers react sensitively

1. Hooke(2005, page 21) gives the following example: "Most of the warming of alpine snow pack is a result of the release of latent heat during refreezing of the first water to infiltrate. Freezing of 1kg of water can warm 160kg of snow $1^{\circ}C$."

2. Snow texture “influences the area of contact between adjacent ice grains” (Adams & Sato, 1993).

to variations in the surface energy balance" (Lüthi & Funk, 2001, page 314). For example a thin ice layer of 50-100m with a high accumulation rates of "typically $0.2-5 \text{ ma}^{-1}$ *w.e.* rapidly advects temperature changes of the firm near the surface into the body of the glacier" (Lüthi & Funk, 2001, page 314).

According to Irvine-Fynn et al. (2011), cold ice is practically impermeable, and interstitial water in cold ice is negligible unless existing channels and fractures letting liquid water going through (Boon & Sharp, 2003). It means that the penetration of meltwater to the glacier bed and the entrainment of subglacial sediments by meltwater runoff are restricted (Irvine-Fynn et al., 2011). Nevertheless, due to low rates of ice deformation and meltwater draining into crevasses, the presence of crevasses and moulins are rare (Copland et al., 2003, Irvine-Fynn et al., 2011) compared to temperate glaciers (Gilbert, 2013). In cold glacier, the permeability has another scale as in temperate glacier. The permeability is originating from the crevasses and moulins (Copland et al., 2003). According to Hutter et al. (1988), cold ice has the three following characteristics: It behaves like a viscous fluid. It conducts the heat and is incompressible.

2.1.2 Temperate glacier

Temperate ice is ice at the ice melting point (Hutter et al., 1988; Pettersson et al., 2004; Haefeli, 1953), and is considered as a mix of ice and water (Hutter et al., 1988; Pettersson et al., 2004; Cuffey & Paterson, 2010; Greve & Blatter, 2009). The glacier is called temperate glacier (Greve & Blatter, 2009). The content of interstitial liquid could reach up to 9% by volume, and measured water contents in temperate ice are generally less than 3% (Pettersson et al., 2004). "Temperate ice contains a certain amount of water, [...] which takes the role as the main thermodynamic quantity instead of the temperature" (Greve & Blatter, 2009, page 237).

Cold ice and temperate ice do not react similarly to a change in heat content. If some heat is brought in cold ice, the temperature of cold ice will change and increase. If some heat is brought in temperate ice, the water content will increase (Greve & Blatter, 2009). Temperate ice is more permeable than cold ice. Channels formation is thus easier (Gilbert, 2013). As the channels could easily reach the glacier base, the meltwater could effectively flow away (Fountain & Walder, 1998). The content of water in the ice influences the flow properties of temperate ice (Greve & Blatter, 2009). It is important to emphasize that temperate ice does not only contain water and ice, but also "air, salts, and carbon dioxide" (Cuffey & Paterson, 2010, page 405). The impurities are more present in water than in ice, which also affects the equilibrium temperature (Cuffey & Paterson, 2010). "For a glacier to be temperate, it must contain heat sources and sinks. These are provided by the freezing of small quantities of water and the melting of small quantities of ice" (Cuffey & Paterson, 2010, page 407). Generally, the temperate glacier found at lower latitudes, but could have a cold temporary surface layer in winter (Greve & Blatter, 2009) (see chapter 2.1.3).

2.1.3 Polythermal glacier

Polythermal glaciers are partially cold and partially temperate at the same time (Blatter & Hutter, 1991; Fowler & Larson, 1978; Greve & Blatter, 2009). The cold part is separated from the temperate part by the cold-temperate transition surface (CTS), which "constitutes the phase-change surface between the cold and the temperate regions of the glacier" (Greve & Blatter, 2009, page 242). "Most glaciers are seasonally polythermal" because the surface layer in temperate glaciers could be cooled in winter, and in cold glaciers, the surface layer could be warmed in summer (Greve & Blatter, 2009, page 253). In the case of polythermal glaciers, the spatial distribution of water content for the temperate part of the glacier and temperature for the cold part is relevant (Greve & Blatter, 2009).

2.2 Characteristics of glacier ice

2.2.1 Glacier ice

Glacier ice results from the diagenesis of accumulated snow (Fig. 2.1, left). This snow transforms into ice by orthogonal recrystallization to the thermal gradient. Ice crystallizes in normal pressure conditions in a hexagonal system (Van Vliet-Lanoë, 2005) (Fig. 2.1). Glacier ice is thus polycrystalline, i.e., "an aggregate of many individual ice crystals" (Cuffey & Paterson, 2010, page 30) (Fig. 2.1). The deformation of glacier ice is strongly related to the growth of crystals, the

alignment of crystals along preferred orientations. An ice crystal does not deform in all planes. Thus, the orientation of applied stress affects the ability of an ice crystal to deform. Shear stress applied to the basal planes easily causes shear deformation (Cuffey & Paterson, 2010). McConnell (1891) compares ice planes with a deck of cards (Fig. 2.1, right). The card faces correspond to the basal planes of the ice crystal. The ice crystals slip easily on basal planes (Cuffey & Paterson, 2010) (Fig. 2.1, right). Trying to deform an ice crystal in another plane than the basal planes is three or four times harder (Duval et al., 1983). Since an individual ice crystal is easily deformed if the shear stress is applied on the basal planes, the polycrystalline ice also deforms if shear stress is applied on the basal planes (Cuffey & Paterson, 2010). The weight of the glacier creates normal stress on the ice, and the slope of the glacier creates shear stress. Shear stress depends on the thickness and the slope of the glacier. Bigger is the glacier thickness and the slope, higher is the shear stress (Van Vliet-Lanoë, 2005).

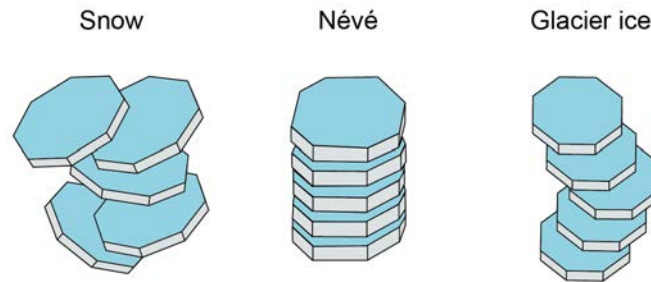


Figure 2.1 – Snow crystals randomly stack up (left). The thermal gradient and the pressure, which are undergone by the névé, recrystallize the névé crystals and reorganize them (middle). Glacier ice shears under the basal planes when it flows (right) (adapted from Van Vliet-Lanoë (2005, page 148, Fig. 9.7)). The top and the bottom of the ice crystal are called basal plane and the six lateral faces of the ice crystal are called prismatic planes (Hooke, 2005).

2.2.2 Movement of glacier ice

The glacier ice creeps. It means that “it slowly and continuously deforms under an applied stress” since “ice behaves as a thick viscous fluid” (Cuffey & Paterson, 2010, page 29). The process of creep plays an important role in the closure of ice tunnels (Cuffey & Paterson, 2010). To describe the creep of ice, a formula, called creep relation, connects the rate and orientation of creep deformation and the applied stress. The creep relation depends on the material property and is defined empirically. To ensure this, laboratory experiments and analyses of field measurements should be combined. Laboratory experiments systematically provide a general in situ behavior of the material. In laboratory experiments, all parameters (pressure, temperature) are under controlled conditions. In the laboratory, experiments were conducted on a single crystal. These experiments show that the shear strain rate $\dot{\epsilon}$ depends on the shear stress τ (Duval et al., 1983). The shear stress τ acts on basal planes. When glacier ice is deforming, preferred crystal orientations develop (Cuffey & Paterson, 2010). Field measurements show how concrete ice behaves in situ, however, not systematically. It was noticed, that the creep relation is influenced by grain-scale structural properties, fabric, and texture (Cuffey & Paterson, 2010). For example, Cuffey and Paterson (2010) emphasize that in temperate ice, ice grains are very coarse and deform less rapidly compared to cold ice.

The term $\frac{\partial v}{\partial y}$ corresponds to the velocity gradient in x-direction through the volume V . In other words, it is the shear rate (Fig. 2.3). The velocity does not constantly evolve with depth (Fig. 2.3). The term $\frac{\partial u}{\partial x} dx$ (Fig. 2.2) corresponds to the change in velocity through the volume (Hooke, 2005, page 9) in the x-direction.

Since ice is considered as incompressible, there is no change in mass with time. It means $\frac{\partial m}{\partial t} = 0$. In Appendix A.1, $\frac{\partial m}{\partial t}$ is determined by means of the velocity in volume \vec{U}_{in} and out the volume \vec{U}_{out} (eq. A.1.1) (see the chapter A.1 to obtain the equation (2.2.1)). By adding all the mass fluxes of the figure 2.2, the following relation is obtained:

$$-\frac{1}{\rho \cdot dx \cdot dy \cdot dz} \frac{\partial m}{\partial t} = \frac{\partial u}{\partial x} + \frac{\partial v}{\partial y} + \frac{\partial w}{\partial z} = \vec{\nabla} \cdot \vec{U}_{in} = 0 \quad (2.2.1)$$

The equation (2.2.1) is multiplied by $-\frac{1}{\rho \cdot dx \cdot dy \cdot dz}$. The change in mass with time $\frac{\partial m}{\partial t}$ can be rewritten as following:

$$\frac{\partial m}{\partial t} = \frac{\partial u}{\partial x} + \frac{\partial v}{\partial y} + \frac{\partial w}{\partial z} = \vec{\nabla} \cdot \vec{U}_{in} = 0 \quad (2.2.2)$$

Since the mass does not change, the density ρ does not change (Hooke, 2005, page 10).

To describe the deformation of glaciers, the power-law creep is applied. The strain rate $\dot{\epsilon}$ is proportional to the stress σ . With all experiments and tests already done, the strain rate is empirically proportional to the cubic of the stress. Hooke (2005) emphasises that the processes, acting in power-law creep, are dislocation glide and climb.

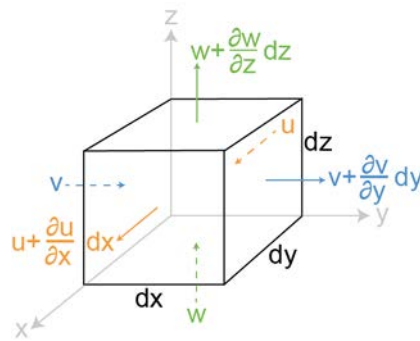


Figure 2.2 – Graphical representation of the velocity vectors \vec{U}_{in} and \vec{U}_{out} (eq. A.1.1) (adapted from Hooke (2005, Fig. 2.2 page 9))

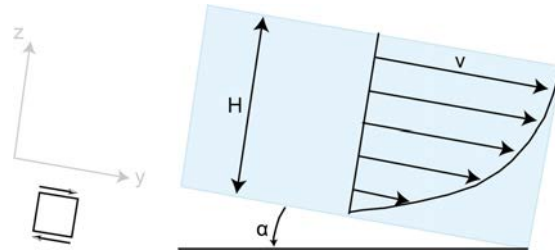


Figure 2.3 – Representation of the shear stress in a plane yz . The velocity \vec{v} behaves differently according to the depth. There is more deformation at the surface than at the bottom. According to Hooke (2005, page 88), "the vertical velocity decreases linearly with depth". (adapted from Greve and Blatter (2009, Fig. 3.11, page 62) and Hooke (2005, Fig. 2.4, page 11))

2.3 Stress, strain and strain rates

2.3.1 Stress

The dimension of stress is $\frac{N}{m^2}$ or Pa . The stress represents the force applied on a surface (eq. 2.3.1). Since there is a force, the stress is a vector and possesses a magnitude and a direction. It exists two kinds of stress: normal stress and shear stress. Normal stress represents stress, which is applied normal to the surface. Shear stress represents stress, which is applied parallel to the surface (Hooke, 2005). On Figure 2.4 (left), the indices of the shear stress σ_{xz} indicates that the shear stress is perpendicular to the plane x (i.e., the stress acts on the plane x) and parallel to the plane z (i.e., the stress goes in the direction of the plane z). According to the definition of

the different normal vector \hat{n} , normal or shear stress will be positive or negative according to their direction. Positive stress is called tension, and negative stress is called compression (Hooke, 2005).

$$\text{Stress [Pa]: } \sigma = \frac{F}{A} \quad (2.3.1)$$

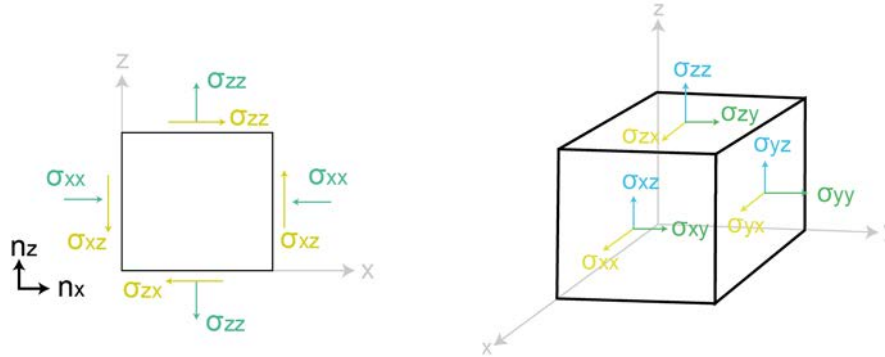


Figure 2.4 – Left: Representation of the different stresses in 2D (xz-plane) (adapted from Hooke (2005, Fig. 2.3, page 11)). Right: Infinitesimal representation of the different stresses of the glacier in 3D (adapted from Hooke (2005, Fig. 2.5, page 12)).

On Figure 2.4 (right), the stresses on three faces are represented. The stresses are similar to the six other faces. However, the direction of the stresses changes. According Hooke (2005), "stresses on any given face can be regarded as uniformly distributed and constant".

The state of stress can be described by a second-rank tensor and possesses nine components (eq. 2.3.2).

$$\sigma = \begin{bmatrix} \sigma_{xx} & \sigma_{xy} & \sigma_{xz} \\ \sigma_{yx} & \sigma_{yy} & \sigma_{yz} \\ \sigma_{zx} & \sigma_{zy} & \sigma_{zz} \end{bmatrix} \quad (2.3.2)$$

It exists many different stresses. For example, the hydrostatic pressure corresponds to the weight of the ice (eq. 2.3.3). This stress linearly increases with depth.

$$\text{Hydrostatic pressure [Pa]: } P = \rho \cdot g \cdot h \quad (2.3.3)$$

For an high depth, the deformation will be high. According to Hooke (2005), hydrostatic pressure (eq. 2.3.3) is not the only stress that deforms ice. The deviatoric stress tensor is necessary. The stress (eq. 2.3.4), described by the second-rank tensor (2.3.2), is composed of the deviatoric stress σ' and the hydrostatic stress tensor σ_{hyd} .

$$\text{Stress tensor : } \sigma = \sigma' + \sigma_{hyd} \quad (2.3.4)$$

The mean hydrostatic stress σ_{hyd} is defined by the equations (2.3.5) and (2.3.6).

$$\sigma_{hyd} = \frac{1}{3}(\sigma_{xx} + \sigma_{yy} + \sigma_{zz}) \quad (2.3.5)$$

The hydrostatic stress tensor σ_{hyd} is defined by:

$$\sigma_{hyd} = \begin{bmatrix} \sigma_{xx} & 0 & 0 \\ 0 & \sigma_{yy} & 0 \\ 0 & 0 & \sigma_{zz} \end{bmatrix} \quad (2.3.6)$$

The first deformation, when the ice is loaded with stress, is elastic. Then, ice begins to creep. This creep is directly applied to good-oriented ice crystals. Ice crystals slip on the basal plane.

Then, the creep begins for ice crystals that are not favorably oriented. For these crystals, the stress can be high, so that they slip (Hooke, 2005). Due to the ice incompressibility, ice deformation does not depend on mean hydrostatic stress, but on deviatoric stresses. The deviatoric stresses for shear stress are the same as the non-deviatoric stresses. The deviatoric stresses for normal stress are thus different from non-deviatoric stresses (Hooke, 2005). According Hooke (2005, page 257), "In general, deformation depends only on these non-hydrostatic components of the stress field".

The yield criterion is an important concept to know when the material will deform. If the left part (eq. 2.3.7) is smaller than the constant k , the material will not deform. The constant k is empirically defined (Hooke, 2005). It exists different yield criteria. Here is that of von Mises (Hooke, 2005):

$$\text{Yield criterion of Von Mises : } |(\sigma_1 - \sigma_2)^2 + (\sigma_2 - \sigma_3)^2 + (\sigma_3 - \sigma_1)^2| \geq k \quad (2.3.7)$$

If the material is considered as perfectly plastic, the material will respect the yield criterion (eq. 2.3.7), and will not deform, if the left part (eq. 2.3.7) is smaller than the constant k . When the left part reaches the constant k (eq. 2.3.7), it corresponds to the start of the deformation (Hooke, 2005). In the case of perfectly plastic material, the n exponent of Glen's flow law (eq. 2.3.8) goes to infinite. In other words, σ should equal B to deform the material. B corresponds to the viscosity. If B is large, the ice is stiff. The stiffness decreases with a lower B . For a viscoplastic material, the material will deform when the yield stress is reached (eq. 2.3.7). This deformation is proportional to the applied stress (Glen, 1955) (eq. 2.3.8).

$$\text{Glen's flow law : } \dot{\epsilon} = \left(\frac{\sigma}{B}\right)^n \quad (2.3.8)$$

The n coefficient is experimentally defined as 3 for glaciers (Hooke, 1981, 2005) (Fig. 2.5). On Figure 2.5, the rate of contraction evolves more or less linearly according to the pressure (except for the glacier of Arolla) with n coefficient of 3.11 and B factor of $0.18 \text{ MPa} \cdot \text{a}^{1/n}$.

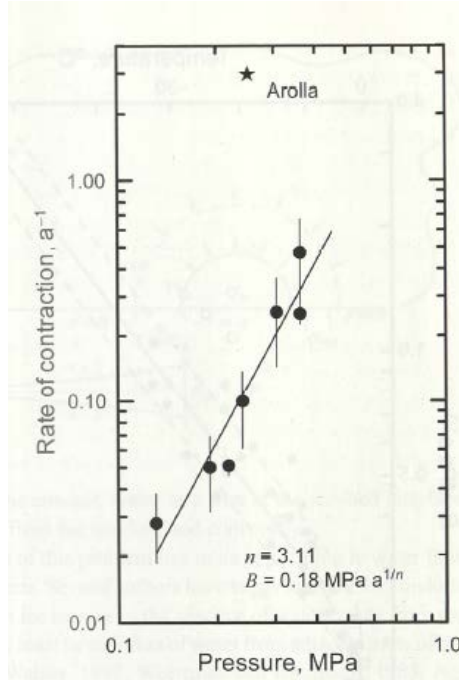


Figure 2.5 – This graph represents the rate of contraction according the pressure in ice galleries (Hooke, 2005, Fig. 12.4, page 323)

It is possible to apply another flow law (eq. 2.3.9). The unit of the A factor is $\text{a}^{-1} \text{MPa}^{-n}$ and the unit of the B factor is $\text{a}^{\frac{1}{n}} \text{MPa}$.

$$\text{Flow law : } \dot{\epsilon} = A \cdot \sigma^n. \quad (2.3.9)$$

The both factors A and B are proportional by the following relation:

$$A = \left(\frac{1}{B}\right)^n \quad (2.3.10)$$

According to Glen (1958), the flow law with A factor (eq. 2.3.9) is better adapted to describe ice rheology, when Glen's flow law (eq. 2.3.8) is better adapted for fluid mechanics. Cuffey and Paterson (2010) give some values for A factor in Figure 2.8.

On Figure 2.6, the B factor, which represents the viscosity, depends on temperature.

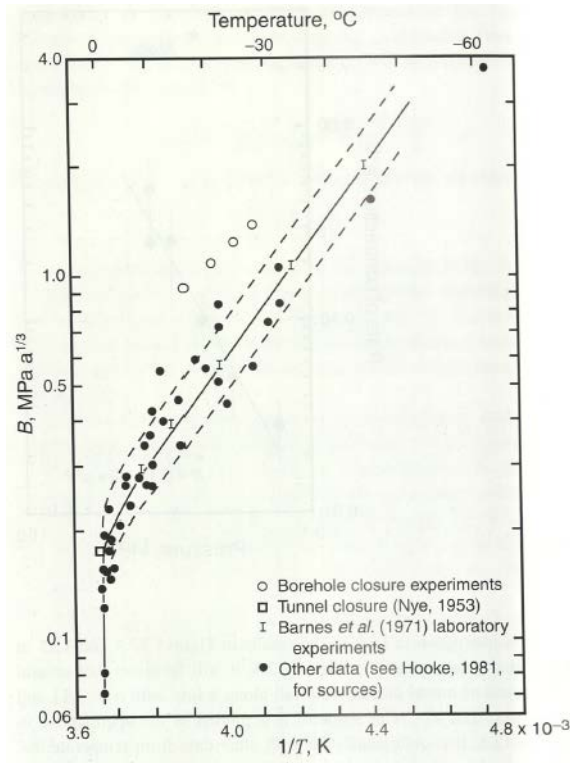


Figure 2.6 – This graph represents the B according to different temperatures. They measured or estimated the minimum strain rate to determine the B factor. The upper dashed line gives strain rates double those of the strain rates represented by the solid line. The lower dashed line gives strain rates half those of the strain rates represented by the solid line (Hooke, 2005, Fig. 12.5, page 324).

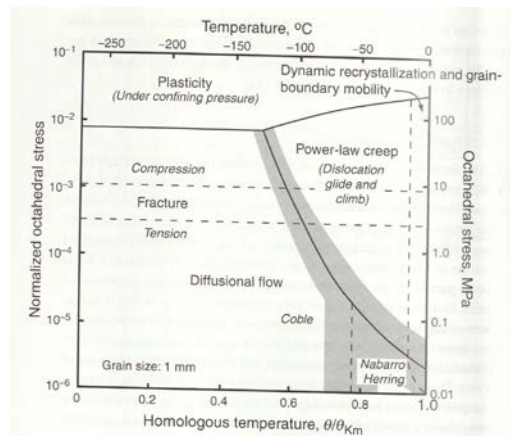


Figure 2.7 – Map of different deformations according to ice temperature and octahedral stress (Hooke, 2005, Fig. 4.16, page 64). This map was tested for a ice grain with a size of 1mm.

$T(^{\circ}\text{C})$	$A(\text{s}^{-1}\text{Pa}^{-3})$
0	2.4×10^{-24}
-2	1.7×10^{-24}
-5	9.3×10^{-25}
-10	3.5

Figure 2.8 – A factor at different temperatures with $n=3$ (Cuffey and Paterson, 2010, page 75)

On Figure 2.7, the kind of law to describe the glacier motion depends on the temperature and the pressure. For temperature close to 0°C and stress between 0.1 and 100 MPa, the better law to describe glacier motion is power-law creep.

In accumulation zone, flow has an extensive behavior, when in ablation zone, flow has a compressive behavior (Hooke, 2005). High stress also affects the creation of crevasses. Crevasses are opened by tensile stresses. On the other hand, the weight of ice closes the crevasses (Hooke, 2005).

2.3.2 Strain

A consequence of stress is a deformation for a deformable medium, called strain ϵ . It is the length change Δl divided by the initial length l_0 (eq. 2.3.11). Ice is a material where the deformation is so low at low stresses (Hooke, 2005).

$$\text{Strain [-]: } \epsilon = \frac{\Delta l}{l_0} \quad (2.3.11)$$

To simplify the modelling, the deformation can be described by the concept of plane strain. It means, that the deformations exist in two directions and are nonexistent in the third direction (Hooke, 2005). In Appendix A.2, the strains have been defined for different directions.

In the modelling (see chapter 2.6.2), the strain is defined as finite. "Finite strain accounts for the compounding effects of cumulative deformation on further strain" (Cuffey & Paterson, 2010, page 434). In the case of simple shear and large strains, the length L linearly increases or decreases as a function of $\dot{\epsilon} \cdot \Delta t$ (Cuffey & Paterson, 2010).

2.3.3 Strain rate

The strain rate $\dot{\epsilon}$ (eq. 2.3.12 and 2.3.13) corresponds to the deformation velocity of a deformable medium (Hooke, 2005).

$$\text{Strain rate for } \dot{\epsilon}_{xx} [s^{-1}]: \dot{\epsilon}_{xx} = \frac{\partial u}{\partial x} \quad (2.3.12)$$

$$\text{Strain rate for } \dot{\epsilon}_{xy} [s^{-1}]: \dot{\epsilon}_{xy} = \frac{1}{2} \left(\frac{\partial u}{\partial y} + \frac{\partial v}{\partial x} \right) \quad (2.3.13)$$

The incompressibility condition can be also written as:

$$\text{Incompressibility condition : } \dot{\epsilon}_{xx} + \dot{\epsilon}_{yy} + \dot{\epsilon}_{zz} = 0 \quad (2.3.14)$$

To satisfy "the condition that the principal axes of stress and strain rate coincide" (Hooke, 2005, page 267), strain rate $\dot{\epsilon}$ is linked to stress σ with a scalar λ . The advantage of the characteristics of the scalar λ is the independence of stress directions. The scalar λ emphasizes the isotropic behavior and the incompressible characteristic of ice. This condition is written : $\dot{\epsilon}_{ij} = \lambda \cdot \sigma_{ij}$. According to the kind of fluid, the definition of λ differs. If ice is considered as a Newtonian fluid, $\lambda = \frac{1}{\eta}$. The parameter η corresponds to the Newtonian viscosity. If ice is considered as a power-law

fluid, $\lambda = \frac{\sigma^{n-1}}{B^n}$. The parameter B depends on temperature, density, crystal size and orientation. If ice is considered as a perfect material, $\lambda = 0$ if $\sigma < k$ and $\lambda = f(\dot{\epsilon})$ (Hooke, 2005).

On Figure 2.9, strain rate $\dot{\epsilon}$ depends on temperature for a constant stress. From 0°C to -20°C , the velocity of deformation rapidly decreases. From -20°C to -60°C , the deformation evolves a little bit slower.

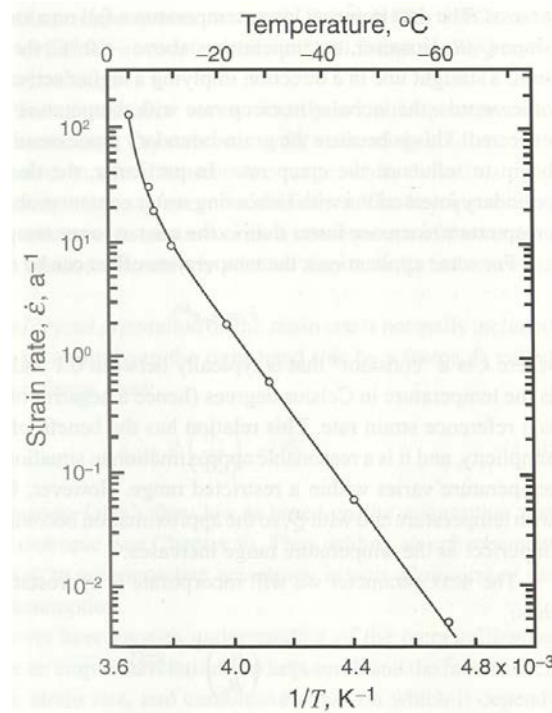


Figure 2.9 – This graph represents the strain rate according to different temperatures. The stress is constant during the experiment (Hooke, 2005, Fig. 4.17, page 67).

2.4 Rheology

According to the kind of material, the deformations behave differently. Some materials can behave like a solid or a fluid. It depends on the applied stresses. If the material is solid, it possesses a shear stress limit. When this limit is reached, the material will crack (Amiroudine & Battaglia, 2014). The ice behaves like a solid with its crevasses. When the applied shear stresses are under this limit, the processes are the plasticity and the elasticity (Amiroudine & Battaglia, 2014). The material stops to deform when there are no more applied stresses. With comparison to a solid, a fluid continually deforms but cannot find its initial form again (Amiroudine & Battaglia, 2014). The ice behaves like a fluid with its glacier flow. Rheology studies the deformation and the flow of solid or liquid material (Barnes, Hutton, & Walters, 1989).

2.4.1 Elasticity

The behavior of elastic solids, called Hookean solid (Tanner, 2002), can be described with a linear relation, which links the applied force F to the extension $(F = -kx)^3$ (Moyer, 1977). If shear stress τ is applied, it results in an immediate deformation. The constitutive equation is $\tau = G\gamma$, where G is the rigidity modulus and γ the strain. In case of uniaxial load, i.e. $\sigma_x = \sigma_y = 0$, the relation between normal stress σ and strain ϵ can be calculated with Hooke's law (eq. 2.4.1) (Timoshenko & Goodier, 1970).

$$\text{Hooke's law : } \sigma_z = E \cdot \epsilon_z \quad (2.4.1)$$

- σ_z = normal stress in z-direction [Pa]

3. F is the force, x the elongation and k the force constant of spring

- E = Young's modulus [Pa]
- ϵ_z = strain in z-direction [-]

2.4.2 Viscosity

The behavior of viscous liquids, called Newtonian fluid (Tanner, 2002), can be described with a relation, which links the shear stress to the shear rate. The viscosity η corresponds to the internal friction and measures the resistance to flow. For most liquids, the viscosity η is not a coefficient but depends on the strain rate $\dot{\gamma}$ and is referred to as the apparent viscosity or shear-dependant viscosity (eq. 2.4.2). The viscosity can be described in Poise. The unit is ten times bigger than the SI-unit $Pa \cdot s$ (Barnes et al., 1989).

$$\text{Shear-rate - dependent viscosity : } \tau = \eta \cdot \dot{\gamma} \quad (2.4.2)$$

- τ = shear stress [Pa]
- η = coefficient of viscosity [$Pa \cdot s$]
- $\dot{\gamma}$ = strain rate [s^{-1}]

Viscosity changes with strain rate, which depends on the applied stress, the temperature, the pressure, and the time of shearing. The strain rate $\dot{\gamma}$ can be approximated by dividing the average velocity of the flowing liquid by the thickness of a sheared layer. The relation between the viscosity and the temperature in Newtonian liquids can be approximated with the Arrhenius relationship (eq. 2.4.3) (Barnes et al., 1989).

$$\text{Arrhenius relationship : } \eta = A \cdot \exp -\frac{B}{T} \quad (2.4.3)$$

- A and B = constant of the liquid
- T = absolute temperature

2.4.3 Viscoelasticity

However, not all materials can be described by Hooke's law or Newton's law alone. In 1835, Weber carried out experimentally with not perfectly elastic elements like a silk thread. He applied a longitudinal load to the thread and firstly noticed an immediate extension. This immediate extension corresponds to the elastic behavior of a solid. Then, a slower extension continued with time. After removing the load, Weber noticed immediate contraction, and then the fiber continued to shorten with time until it reached its original length (Barnes et al., 1989; Tanner, 2002). Some materials are solid-like but react like a liquid-like material. These materials can be described with viscoelasticity (Barnes et al., 1989).

The material properties are described with the rigidity modulus G (elasticity) and the coefficient of viscosity η (viscosity). The change of material properties and the dominance of the property depend on the stress applied and the period of time (instantaneously or over a long period). The results of this change can be an increase or a decrease in the material parameters. According to the stress applied and the period of time, it is possible to observe liquid-like properties in solids and solid-like properties in liquids (Barnes et al., 1989). Viscoelasticity described the behavior of materials between Hookean elastic response and Newtonian viscous behavior.

A viscoelastic material can be described by three different models: the Kelvin-Voigt model, the Maxwell model, and the Burger model. These three models put together springs and dampers in different configurations. The Kelvin-Voigt model puts the spring and the damper in parallel. The Maxwell model puts the spring and the damper in series. The Burger model is a system of two parts. The first part corresponds to the Kelvin-Voigt model with a spring and a damper in parallel. The second part is a damper (Giorla, 2017).

2.5 Collapse of a cylindrical hole

Nye (1953) studied the closure of a cylindrical hole in ice galleries. The goal of this study was to estimate values for the constants of Glen's flow law. Hooke (2005) firstly simplifies the problem of the closure of a cylindrical hole in an ice gallery to an infinite weightless medium (Fig. 2.10). The hole has a radius r and a length a .

The development of the following equations finds in Appendix A.3 and it is recommended to read the chapter 12 of Hooke (2005) for more details. The effective strain rate is $\dot{\epsilon} = \frac{c}{r^2} = f(\sigma)$ (eq. A.3.9). From Glen's flow law (eq. 2.3.9), the following relation can be written:

$$\dot{\epsilon} = f(\sigma) = \left(\frac{\sigma}{B}\right)^n = \frac{c}{r^2} \quad (2.5.1)$$

From equation (A.3.13), the radial stress σ_{rr} is n -times bigger than the effective stress σ . Now, the radial stress $\sigma_{rr} = n \cdot B \left(\frac{c}{r^2}\right)^{\frac{1}{n}}$ and the stress on the wall $\sigma_a = n \cdot B \left(\frac{c}{a^2}\right)^{\frac{1}{n}}$ are put in relation:

$$\frac{\sigma_{rr}}{\sigma_a} = \left(\frac{a}{r}\right)^{\frac{2}{n}} \quad (2.5.2)$$

The pressure of the overlying ice is taking into account. The hydrostatic pressure is defined as $P_h = \rho \cdot g \cdot h$ and $\sigma_a = P_h$. The particularity of the hydrostatic pressure is that it equally influences all stresses. The effective stress can be rewritten as $\sigma = \frac{P_h}{n}$.

The closure rate is related to the B factor.

$$-\frac{u_a}{a} = \left(\frac{P_h}{n \cdot B}\right)^n \quad (2.5.3)$$

Hooke (2005) plots the data of Nye (1953) and notices that n has a value of 3.11 and B has a value of $0.13 \text{ MPa} \cdot a^{\frac{1}{n}}$ for temperate glaciers (Fig. 2.5).

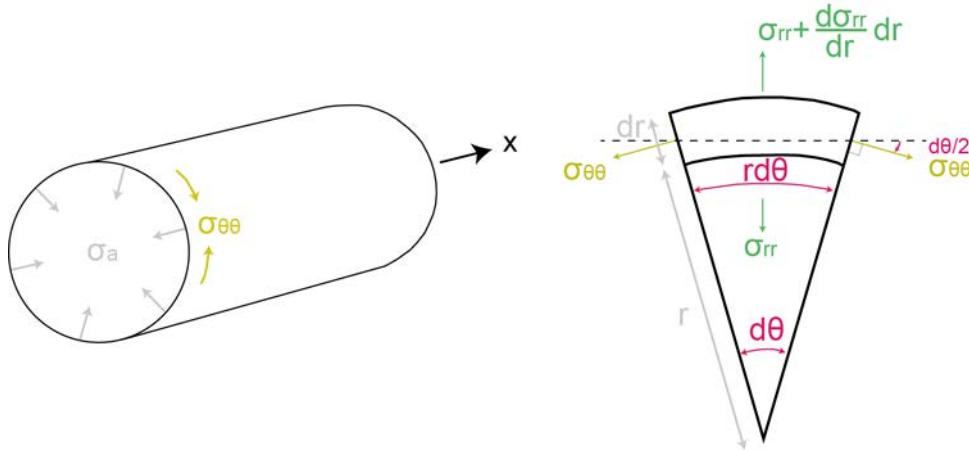


Figure 2.10 – Stresses on the wall of a cylindrical hole in a weightless medium (adapted from Hooke (2005, Fig. 12.1, page 316 (left) and Fig. 12.2, page 317 (right)))

2.6 Modelling with MOOSE

Finite-Element Methods (FEM) enable to resolve complicated problems for which analytical methods cannot solve. Numerical models enable to determine or to find the most appropriate values to solve the problems. In FEM, the glacier is described with a mesh (Fig. 4.4). The model will compute a solution for each node in the mesh (Hooke, 2005). According to Strang and Fix (1973), FEM should be more stable than Finite-Differences Methods numerically. Advantages with

FEM are the possibility to generate a mesh with cells of different sizes (as on figure 4.4). The cells must not be everywhere a square or a triangle of the same size (as on figure 4.5). Moreover, the boundary conditions could be "complex, non-uniform, and variable" (Hooke, 2005, page 298).

MOOSE enables the creation of a multiphysics code. So, to model the deformation in an ice gallery, the *Tensor Mechanics* Modules of MOOSE are used. It is a library with simulation tools for solving problems of continuum mechanics. This module is useful for problems that use linear and finite strain mechanics such as creep and also elasticity and plasticity (MOOSE Framework, 2020). MOOSE works in system of different blocks. In this chapter, only the blocks *Material* and *Modules/TensorMechanics/Master* will be described and explained because all the physics find in these both blocks. The other blocks define the parameters (input and output), the mesh, the variables.

2.6.1 Material

The *Material* block defines the model and properties of the material (here ice), such as the creep and the elasticity. The block defines the applied equations (MOOSE Framework, 2020).

Compute Isotropic Elasticity Tensor

This block computes the isotropic elasticity tensor (eq. 2.6.1) given by a 6x6 matrix (Malvern, 1969). For that, MOOSE needs two constants as input. It could be Lamé constant λ , the shear modulus μ , the bulk modulus K, Young's modulus E, or Poisson's ratio ν (MOOSE Framework, 2020).

$$C_{ijkl} = \begin{pmatrix} \lambda + 2\mu & \lambda & \lambda & 0 & 0 & 0 \\ \lambda & \lambda + 2\mu & \lambda & 0 & 0 & 0 \\ \lambda & \lambda & \lambda + 2\mu & 0 & 0 & 0 \\ 0 & 0 & 0 & \mu & 0 & 0 \\ 0 & 0 & 0 & 0 & \mu & 0 \\ 0 & 0 & 0 & 0 & 0 & \mu \end{pmatrix} \quad (2.6.1)$$

As seen in the matrix (eq. 2.6.1), MOOSE described the matrix with Lamé parameters λ and μ . If the user provides the Young's modulus E and the Poisson's ratio ν , MOOSE does the conversion (MOOSE Framework, 2020)⁴. For this study, Young's modulus and Poisson's ratio are chosen. According to Hutter (1983), Young's modulus of ice is 8'700 MPa, and Poisson's ratio of ice is 0.31.

Compute Multiple Inelastic Stress

This block computes the stress, the tangent operator, "and a decomposition of the strain into elastic and inelastic components" for an inelastic material model such as creep. The elastic strain $\Delta\epsilon_{el}$ is the difference between the mechanical strain increment tensor $\Delta\epsilon_{mec}$ and the computed inelastic strain increment $\Delta\epsilon_{inel}$ (MOOSE Framework, 2020).

The required input is the inelastic model (*inelastic_models*). This inelastic model enables to calculate stress and inelastic strains. It can be a creep model or a plasticity model (MOOSE Framework, 2020). In this work, a creep model is applied. The creep model will be later defined in another block.

Then, the tangent operator (*tangent_operator*) is defined. There are two options: elastic or inelastic. The elastic tangent operator returns the elasticity tensor. The parameters *max_iterations* and *absolute_tolerance* are necessary for "the stress update iterations over the stress change after all update materials are called" (MOOSE Framework, 2020). *Max_iterations* defines the maximum number of iterations. *Absolute_tolerance* is the absolute convergence tolerance. *Combined_inelastic_strain_weights* weights the different models. If there is only one model, the parameter equals 1 (MOOSE Framework, 2020).⁵

4. For more details, read Slaughter (2012) for more details.

5. For more details about the process and the computation, read <https://www.mooseframework.org/source/materials/ComputeMultipleInelasticStress.html>.

Power Law Creep Stress Update

This block corresponds to the creep model cited in the part **Compute Multiple Inelastic Stress**. This block works as follows. At each time increment, a trial stress σ_{trial} is calculated (MOOSE Framework, 2020) (eq. 2.6.2).

$$\sigma_{trial} = C_{ijkl}(\Delta\sigma_{assumed_elastic} + \sigma_{old,elastic}) \quad (2.6.2)$$

MOOSE tries to determine the stress in the yield surface. If stress finds outside of the yield surface, which is a circle, the inelastic strain is recalculated (MOOSE Framework, 2020).

$$\text{Iterative effective inelastic strain : } \Delta p^{t+1} = \Delta p^t + d\Delta p \quad (2.6.3)$$

$$\text{Creep strain rate : } \dot{\epsilon} = (\sigma_{trial,eff} - 3G\Delta p)^n \exp \frac{-Q}{RT} (t - t_0)^m \quad (2.6.4)$$

- $\sigma_{trial,eff}$ = Von Mises trial stress
- G = isotropic shear modulus
- Q = activation energy
- T = temperature
- R = universal gas constant
- t = current time
- t_0 = initial time
- n,m = exponent values

In this block, the coefficient corresponds to the A factor of the power-law creep equation (eq. 2.3.9). The n exponent acts on effective stress and has generally a value of 3. The m exponent acts on time and has generally a value of 0. Here, the activation energy is considered as 0.

Generic Constant Material

This block defines the density of ice. It is related to the block *Gravity* in the *Kernels*.

Compute Eigenstrain From Initial Stress

This block computes the eigenstrain ϵ . The input is the initial stress $\sigma_{initial}$, which is a matrix of 3x3. The eigenstrain ϵ and the initial stress are related by this equation: $\sigma_{initial} = E \cdot \epsilon$ with the elasticity tensor E. This block is related to block *Modules/TensorMechanics/Master* in order to add this eigenstrain to the mechanical strain on the first time step.

Here, the initial stress results from the weight force.

$$\sigma_{initial} = \begin{pmatrix} 0 & 0 & 0 \\ 0 & 0 & 0 \\ 0 & 0 & \rho \cdot g \cdot (z_{max} - z) \end{pmatrix} \quad (2.6.5)$$

2.6.2 Modules/TensorMechanics/Master

The block *Modules/TensorMechanics/Master* adds strain calculation with the optional parameters *strain*. Here the strain is chosen finite (see chapter 2.3.2). The strain is also incremental. It sets the use of displaced mesh.

Chapter 3

Study site

3.1 Situation of the Jungfraujoch

The Jungfraujoch (coord.: 641'468, 155'262) is a saddle, situated in the Bernese Alps at an altitude of 3'465m a.s.l. and located at the frontier between the canton of the Valais and the canton of Bern (Fig. 3.1). To its northeast lies the Mönch (4'110m a.s.l.) and to its southwest the Jungfrau (4'158 m a.s.l.). A small cold ice cap (Haefeli, 1963; Haefeli & Brentani, 1954a, page 2) of a thickness of 50m (Haefeli & Brentani, 1954b, page 394; 1954a, page 1) covers the saddle (Fig. 3.5). The ice cap of the Jungfraujoch is separated in its southeast from the Grosser Aletsch Gletscher (Jungfraujochfirn) by a bergschrund (Haefeli & Brentani, 1954b, page 2). The ice cap goes down 200m until the Guggigletscher (Haefeli & Brentani, 1954b, page 2) to the northwest (Fig. 3.1).

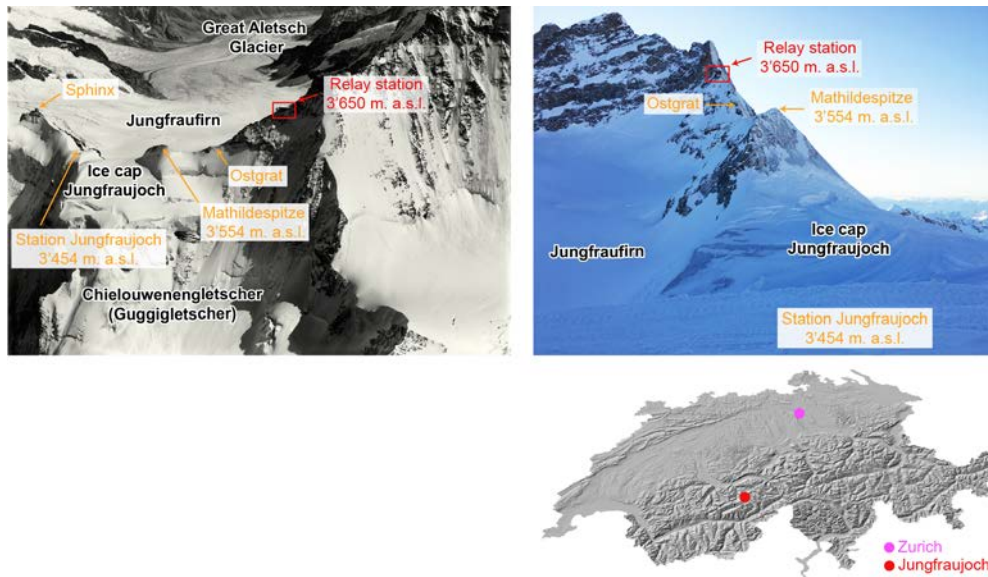


Figure 3.1 – Geographical situation of the Jungfraujoch and location of the main ice gallery. (Source of picture top left: ETHZ(1964). Source of picture top right: Morard(2020). Source picture down right: Swisstopo(2019).

3.2 Historical insight

In the 1950s, the PTT installed a relay station (Volmar, 1962) at 3'650 m. a.s.l. (Ostgrat) (Wegmann, 1998) (Fig. 3.1). To link the Jungfraujoch railway station to the relay station, they built a tunnel in the rock and the ice (Haefeli & Brentani, 1954a) (Fig. 3.4, 3.5, 3.6, 3.8). In October 1950, Prof. Dr. R. Haefeli was hired by the PTT as an expert in glaciology firstly due to water-filled crevasses and secondly for the control of the ice tunnel and to investigate the deformations and the ice plasticity (Haefeli & Schnitter, 1954, page 1; Haefeli, 1956, page 1). The

department of earthwork VAWE was involved in the project by Haefeli for the installation of the measuring devices and the analyses of the measurements (Haefeli & Schnitter, 1954, page 1) and Prof. Müller (Schnitter & Kasser, 1958, page 2). The engineer Brentani conducted the periodical measurements (Haefeli & Schnitter, 1954, page 1; Haefeli, 1956, page 1) and then the engineer Ramseier (Haefeli, 1957, page 1). Both engineers worked for the engineer buro “Firma Rothpletz, Lienhard und Cie” (Haefeli & Schnitter, 1954, page 1; Haefeli, 1957, page 1). Haefeli and Brentani (1954b) observed and quantified in their study deformations in the ice tunnel. Two tunnels were dug perpendicularly to the main tunnel (Fig. 3.4) for reasons of safety and control, and they observed and measured the process of movement, the formation of water-filled crevasses, and the relationships of viscosity (Haefeli & Schnitter, 1954, page 1; Haefeli & Brentani, 1954b). Until 1953, the PTT wished to shift the ice tunnel in the rock. After analyzing the costs and the technical issues, they decided to continue with the main ice tunnel and to discuss again the relocation in 1960 when they will have gathered more information on the ice deformation and temperatures. The cost of the relocation of the ice tunnel in the rock would be between 330'000 and 520'000 CHF (Haefeli & Schnitter, 1954, page 2). The period of time 1950-1954 aimed to observe the ice cap. Then, they extrapolated the results for the period of time 1954-1960 (Haefeli & Schnitter, 1954, page 9).

3.3 Meteorological conditions

The Jungfrauoch “is exposed to all the northwestern and southern” gusts (Haefeli, 1963, page 163). The yearly air temperature measured on the Sphinx is -7.9°C from 01.01.1950 to 31.12.1959 and -6.5°C from 01.01.2010 to 31.12.2019 (MeteoSwiss, 2020) (Fig. 3.2).

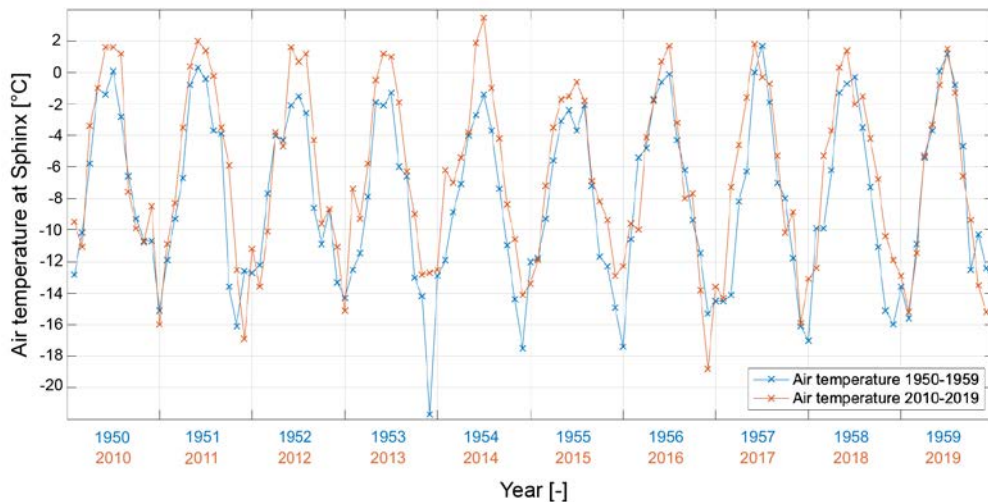


Figure 3.2 – Air temperature at Sphinx for 1950-1959 (blue line) and for 2010-2019 (orange line) (Data from MeteoSwiss (2020))

The average air temperature in the ice tunnel was -5°C in the 1950s. The air temperature in the ice tunnel is approximately 3°C warmer than the air temperature outside. The time shift between the minima and maxima air temperatures in the ice tunnel in comparison to the outside air temperatures is of 2 to 3 months (Haefeli, 1963, 1956). For example, in July, the air temperature reaches the maximal monthly value at the Sphinx. The maximal air temperature in the ice tunnel reaches its maximal monthly value only in October. For example, from the end of July to mid-September until mid-November, the tunnel air temperature goes from -5°C to -2°C due to the seasonal variations. The minimal air temperature measured in the tunnel is -8°C on January 9th, 1956. They noticed that the maximal monthly air temperature in the tunnel is only a few degrees Celsius different from the maximal monthly air temperature at the Sphinx. However, they noticed that the minimum monthly air temperature in the gallery could be 10°C warmer than the minimum monthly air temperature at Sphinx (Haefeli, 1956). In 1955, they observed a temperature variation of $\pm 3^{\circ}\text{C}$, and in 1956, of $\pm 4^{\circ}\text{C}$ in the ice galleries (Haefeli, 1957, page 16). The first meters under the bottom of the ice gallery are influenced by the heating system of the galleries

(Schnitter & Kasser, 1958, page 12). The cold center lies 10m above the bedrock (Schnitter & Kasser, 1958, page 12). The higher temperature variations are noticed at the ice-rock contact at the end of the tunnel (Vöggtli, 1959, page 21).

3.4 Particularity of the Jungfraujoch

The ice cap of the Jungfraujoch consists of cold ice. The ice temperature is below 0°C , and the ice is more brittle and less porous than tempered ice (see chapter 2.1). The crevasses of the ice cap, due to the impermeability of cold ice, are filled with meltwater (Haefeli, 1953, 1963; Haefeli & Schnitter, 1954). In winter, all the meltwater cannot freeze. Then, in summer, the crevasses are covered by a snow cover. The water cannot evaporate or freeze (Haefeli, 1953, page 4, 1963; Haefeli & Brentani, 1954a, page 403, 1954b, page 10). The water in the crevasse applies a hydrostatic pressure on the crevasse walls (Haefeli, 1953, 1963; Haefeli & Schnitter, 1954). In Appendix B.1, there are more information on the crevasses formation at the Jungfraujoch. Very locally, meltwater filling the crevasses modifies the regime, and ice temperature reaches the melting point (Haefeli, 1953, page 3, 1963). With comparison to temperate glaciers, the cold ice flowage is slower (Haefeli & Kasser, 1948). For many years, ice observations were gathered in the ice palace of the Jungfraujoch. This ice palace lies in a calm area of the ice cap. The ice cover is thinner than the ice cover above the tunnel, and the ice temperature is colder than the one at the ice tunnel (Haefeli & Schnitter, 1954, page 3).

Moreover, the ice cap moves in two different directions. A part of the ice cap moves to the north (Haefeli, 1953, page 3, 1956, page 15) (positions hm 1.30 – 1.60) (Haefeli, 1957, page 2) and another part is moving to the south (Haefeli, 1953, page 3, 1956, page 15) (positions hm 0.30 – 1.30 hm) (Haefeli, 1957, page 2) (Fig. 3.7, 3.8, B.5). The maximal southern displacement lies at position hm 1.10. The maximal northern shift lies at position hm 1.40 (Haefeli, 1957). At the position hm 1.40, a lateral buckling is visible in the direction of the north (Haefeli, 1957, page 2). These two parts (north and south) are divided by a dividing line (Haefeli, 1953, page 3, 1956, page 15) (Fig. 3.3). This definition corresponds to a geometric location. This geometric location is a complicated curved surface. Its location cannot be precisely determined, but they define it as a zero surface. It may be probable that this zero surface links the culmination line of the firn surface with the culmination line of the bedrock (Haefeli, 1956). At this fictive line, the deformation is only vertical (Haefeli, 1953, page 3, 1956, page 15). The dividing line lies from 4 to 8 meters north of the central region of the ice cap (hm 1.0 – hm 1.3) (Haefeli & Schnitter, 1954, page 5). The zero surface lies approximately at 15-20m north of the main tunnel in the tunnel Q100 (Haefeli, 1956, page 17). They define a part of the dividing line at a distance of 26m south from the main tunnel (Haefeli & Brentani, 1954a, page 395). Due to the observed asymmetrical boundary conditions, there are three dividing parts: motion divide, ice divide, and water divide (Fig. 3.3). In the ice divide, the horizontal displacements are small. The water divide corresponds to a line, and the ice divide corresponds to a curved surface. However, the ice divide and the motion divide are not similar due to their asymmetrical behaviors (Haefeli, 1957, page 14). However, they assume that the motion divide is better for the position of a tunnel (Haefeli, 1957, page 16).

The ice cap lies on permafrost (Haefeli, 1953, 1963; Haefeli & Schnitter, 1954; Haefeli & Brentani, 1954a, page 403, 1954b) (Fig. 3.9). The temperature of the contact zone between ice and rock goes from -2.5°C to -2.0°C almost everywhere in the tunnel. At the west of the tunnel, the temperature of the contact zone between ice and rock is -3.4°C . This should be caused by the bergschrund. The bergschrund increases the cooling of the contact surface (Haefeli, 1963). The temperature of the contact zone between ice and rock is measured with eight borings. They drilled ice with hot water boreholes. These eight borings are installed along the axis of the main ice tunnel. It enabled them to determine the position of the bedrock (Haefeli, 1963) (Fig. B.7 and B.8).

The measured ice temperature varies approximately between -1°C and -0.3°C (Haefeli, 1953, page 4, Haefeli & Brentani, 1954b). However, ice temperature, measured at the proximity of the tunnels and crevasses, is modified by the water-filled crevasses and by the air circulation of the tunnels (Haefeli, 1953, page 4). The upper part of the ice surface is influenced by the sun radiation, the air humidity, the air temperature. This influence diminishes with depth (Haefeli, 1953, page 3). To not increase the ice plasticity and the velocity deformation of ice, it is essential to install cold air ventilation (Haefeli, 1953, page 4; Haefeli & Schnitter, 1954, page 10; (Haefeli & Brentani, 1954b, page 10)). With air ventilation, they tried to keep the ice temperature at least

1°C under the freezing point (Haefeli & Schnitter, 1954, page 10). However, in November 1954, the air temperature in the tunnels varies between -2°C and -6°C . At the beginning of April, the mean ice temperature reaches -6.5°C . This temperature diminution increases the brittleness of ice (Haefeli, 1956, page 35).

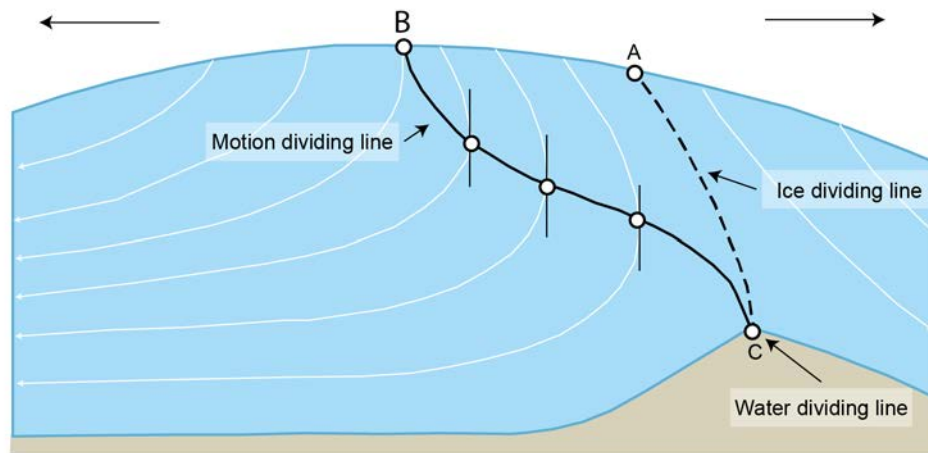
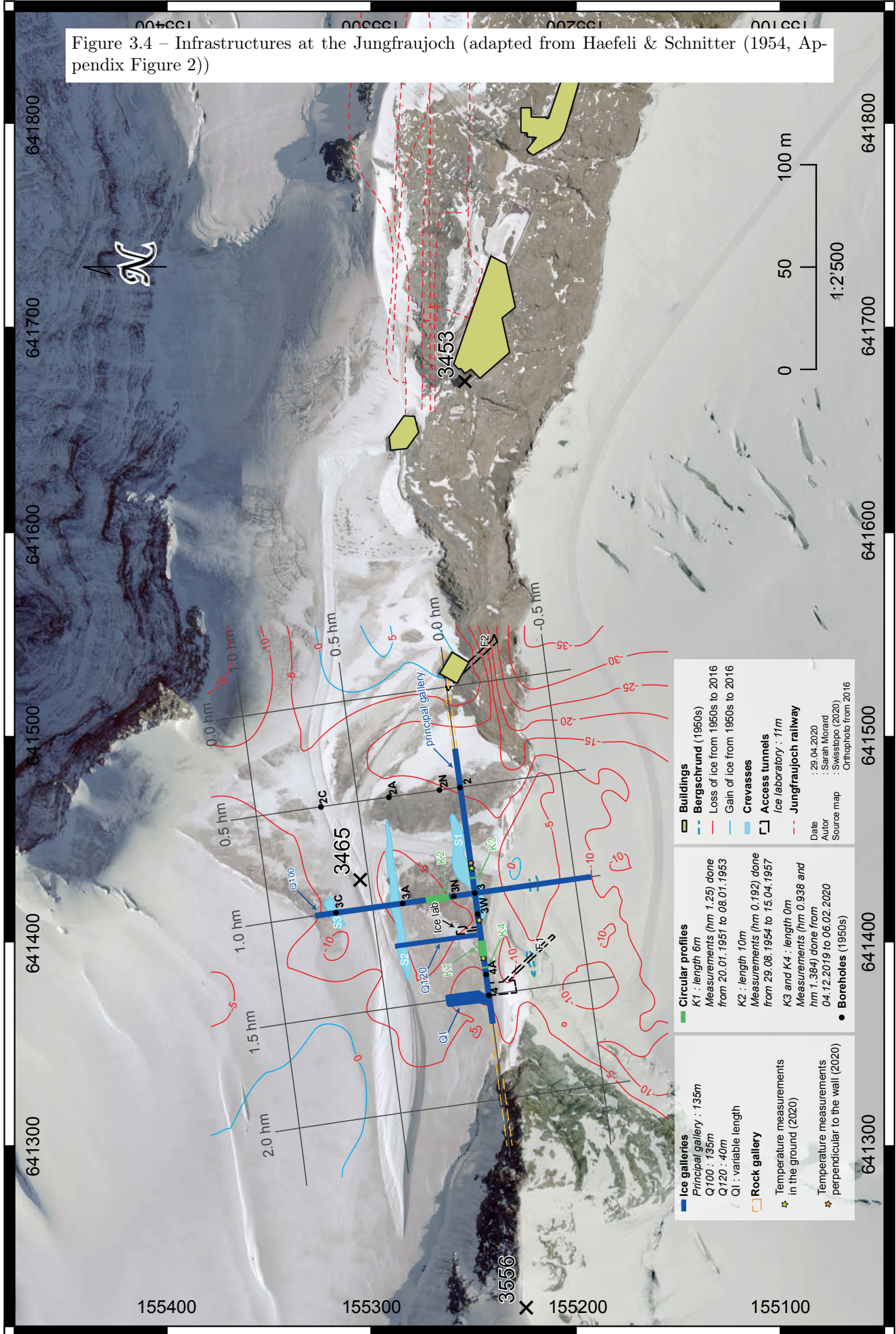


Figure 3.3 – Different dividing lines in the ice cap of the Jungfrauoch (adapted from Haefeli (1957, Appendix 8))

Figure 3.4 – Infrastructures at the Jungfrauoch (adapted from Haefeli & Schnitter (1954, Appendix Figure 2))



The construction plan of the different tunnels comes from the report written by Haefeli and Brentani (1954). The plan has been completed with additional measurements done during the time period 04.12.2019 - 06.02.2020.

3.5 Description of the infrastructure

The infrastructure in the ice cap of the Jungfrauoch consists of the main ice gallery, three transversal ice tunnels, an ice laboratory, two access ice tunnels, boreholes, and circular profiles (Fig. 3.4). The purpose of this infrastructure is the observation and the control of ice motion, ice deformation, and temperature (Haefeli, 1953, page 5) (Fig. 3.4, B.6).

The main ice tunnel links the railway station Jungfrauoch to the Ostgrat (Fig. 3.4). It has a length of 135m. The entrance of the tunnel lies at position hm 0.3, and the exit lies at position hm 1.65. In 1953, the maximal thickness of the ice cap was 52m and laid at position hm 1.00. Its elevation at the surface of the ice cap is 3'470m a.s.l. The ice thickness above the ice gallery at position hm 1.0 is 28m. The maximal ice thickness above the ice gallery lies at position hm 1.65 and reaches a depth of approximately 40m.

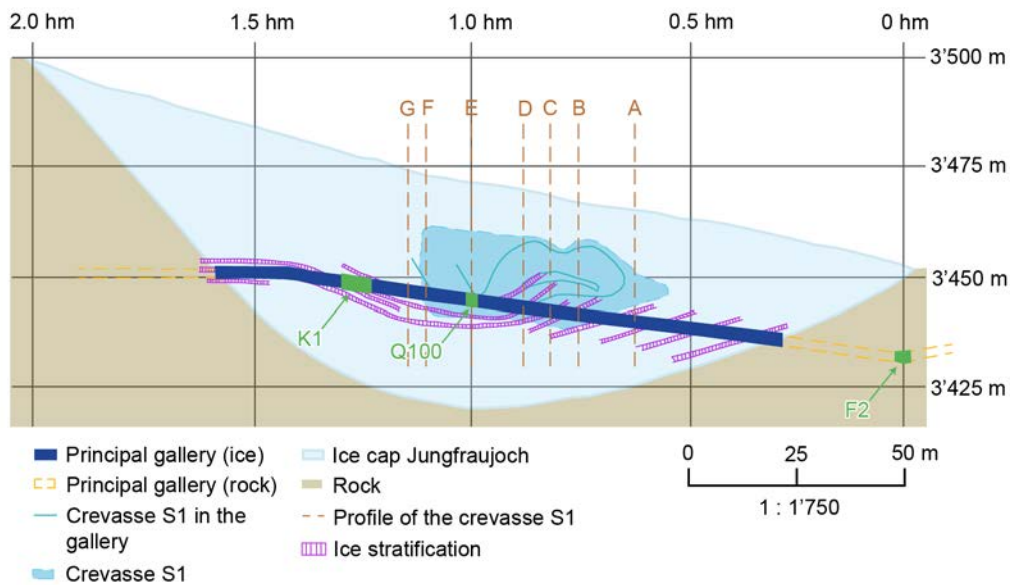


Figure 3.5 – Principal gallery (adapted from Haefeli & Schnitter (1954, Appendix Figure 2))

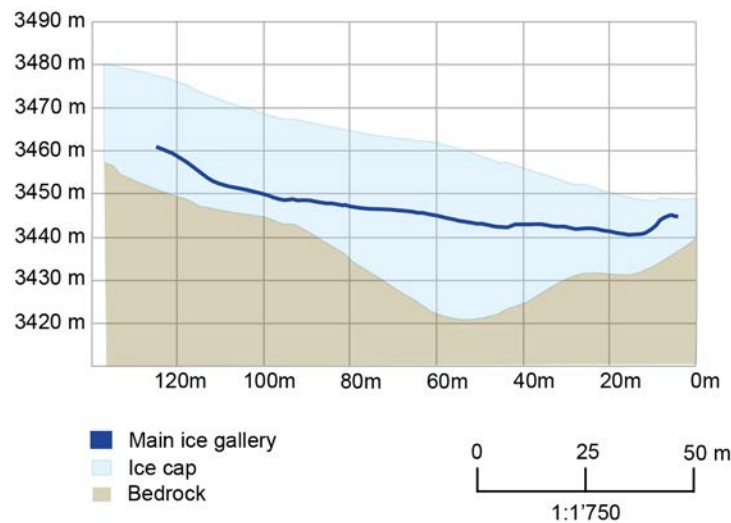


Figure 3.6 – Principal gallery in 2019/2020 (adapted from ETHZ(2019))

The PTT had the idea to change the position of the gallery between the railway and the relay station. The PTT wanted to dig a gallery in the rock. In 1953, they abandoned this idea and announced that the main ice tunnel would be, at least until 1960, the single entrance for the relay station (Haefeli, 1953, page 1). In the beginning, the main ice gallery should operate at least during a period of 10 years to accommodate some infrastructure for the PTT (Haefeli & Brentani, 1954b, page 1). At this time, the main ice tunnel (Fig. 3.6) is still existing. In 1954, the maximal shift from north to south of the main gallery was 33 cm/year (Haefeli & Schnitter, 1954, page 5). The maximal displacement in the southern direction can reach between 3.3 and 4.5m in 1960 (Haefeli & Schnitter, 1954, page 6, Haefeli, 1956, page 17) (Fig. 3.7). The ground of the ice tunnel between the positions hm 1.1 and hm 1.4 sinks at most 10 cm/year. Without adjustment, the ice tunnel ground will be lowered approximately 1 meter in 1960. The length of the main tunnel also varies (Haefeli & Schnitter, 1954).

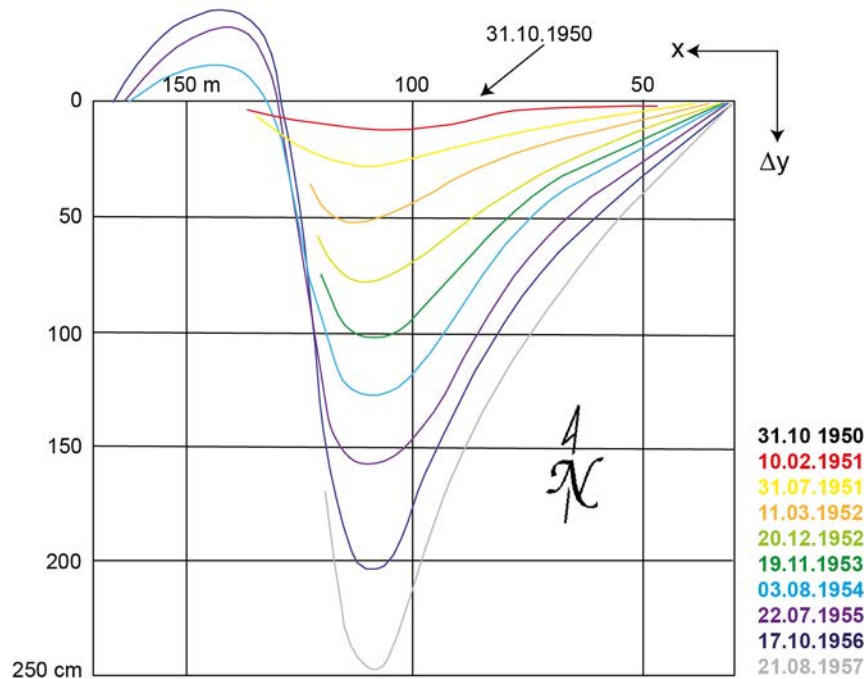


Figure 3.7 – Horizontal displacement of the main tunnel axis (adapted from Haefeli (1963, p.170))

The half part of the main tunnel, which lies in the west (Fig. 3.8), lies in a tension zone between (Haefeli & Schnitter, 1954, page 6) hm 1.2 and hm 1.6 (Haefeli, 1956, page 17). It implies the length is lengthening (Haefeli & Schnitter, 1954, page 6; Haefeli, 1956, page 17, 1957, page 15). The lengthening can reach until 1%/year, and it implies an adaptation for the system of the cable attachment (Haefeli, 1956, page 17). The half part of the main gallery, which lies in the east, (Fig. 3.8) lies in the compression zone. It implies the length is shortening. It is thus necessary to fix the wheel tracks of the little mountain railway in the rock at east and west of the main gallery because the tracks do not support the length change of the main ice gallery (Haefeli & Schnitter, 1954, page 6). Since at the west the ice cap is in tension zone, the ice mass is detaching at the connection between the ice and the rock (Haefeli & Schnitter, 1954, page 7; Haefeli, 1956, page 17). In 1955, an ice mass of approximately 120 m³ detached from the tunnel roof (position hm 1.40-1.55) due to the openness of a crevasse. This event strips the timber support system (Haefeli, 1956). They should find a solution against these ice blocks (Haefeli, 1956, page 6). This change in length of the main tunnel enables to investigate the plastic behavior of cold ice (Haefeli & Brentani, 1954b, page 29). The formation of crevasses highlights a transverse displacement in the direction of the north. It means that the main ice tunnel cuts the dividing line between the positions hm 1.3 and hm 1.6 (Haefeli & Schnitter, 1954, page 7). In 1958, they drilled 12 boreholes each 10m in the main tunnel. However, 4 of these 12 boreholes were already drilled in 1950 (Schnitter & Kasser, 1958, page 3) (Fig. B.7).

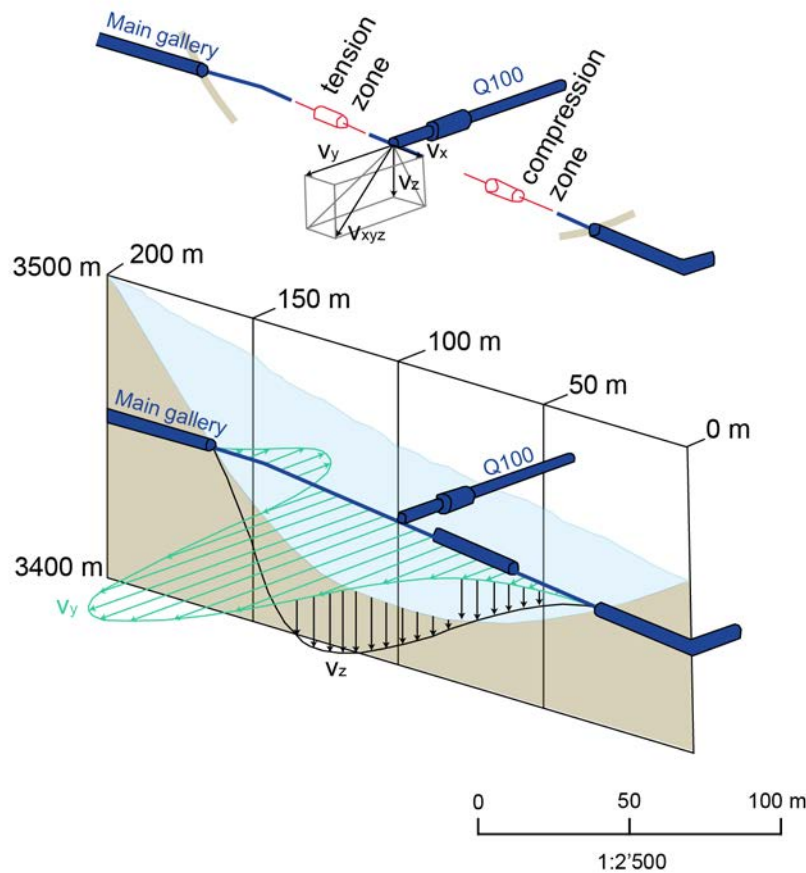


Figure 3.8 – Tension zone and compression zone in the main tunnel (adapted from Haefeli (1963, p. 169))

The ice laboratory (Fig. 3.4) lies at position hm 1.165 and has a length of 11m. In the ice laboratory, they did do growing ice and realized experiment of loading test to complete some theoretical studies (Haefeli & Brentani, 1954a, p. 394, Haefeli & Brentani, 1954b, p. 1). In the ice laboratory, they noticed the evaporation of ice on the bottom of the tunnel and the formation of white frost on the top of the tunnel due to the air circulation (Haefeli & Brentani, 1954a, p. 403, Haefeli & Brentani, 1954b, p. 10).

In 1953, there are only two transversal ice galleries, named transversal gallery I and transversal gallery III (Fig. 3.4). The transversal gallery I lies at position hm 1.50, and its length is variable. On the building plan, its length is 20 m. According to the original building plan, the purpose of this gallery is to extract ice (Haefeli, 1953, page 5). The transversal gallery III lies at position hm 1.20 and has a length of 40 m (Haefeli, 1953, page 5; Haefeli & Brentani, 1954a, page 401). This gallery is called Q120 on the most recent building plan (Haefeli, 1953, page 5). The gallery Q120 (Fig. B.3) is finalized at the beginning of 1953 (Haefeli & Brentani, 1954a, page 401; 1954b, page 6). In this tunnel, they measured air temperature reaching temperatures of -0.6°C due to the heating system (Haefeli, 1956, page 11). In 1955, the transversal gallery Q120 underwent a sharp contraction and lost some measurement points, that they decide to abandon this tunnel and to conserve only the tunnel Q100 (Haefeli, 1956).

In 1953, they decide to dig a new transversal tunnel, called Q100 (Haefeli, 1953, page 5; Haefeli & Brentani, 1954a, p. 401) (Fig. B.4, B.5, 3.9). They finalized it mid-1954 (Haefeli & Brentani, 1954b, page 6). Its purpose is to investigate ice motion in the cross-section of the ice cap and to discover the dividing line of the ice cap (Haefeli, 1953, page 5; 1956, page 7) and to get a tunnel of observation for the crevasses too (Haefeli & Brentani, 1954b, page 3; Haefeli, 1956, page 18) and to

drain the water-filled crevasses lied at the north, which means crevasses S2 and S3 (Haefeli, 1956) (Fig. B.5). The drainage enables to avoid water invasion and to diminish the motion pressure against the south (Haefeli, 1956, page 18). The tunnel Q100 lies at position hm 1.00, which means in the middle of the ice cap. Some boreholes are already bored along the future axis of the tunnel Q100. The tunnel Q100 (Fig.B.5) lies at the north and south of the main tunnel (Haefeli, 1953, page 5; 1956, page 7). They decide to dig the tunnel Q100 at the south too until the bergschrund because the main tunnel progressively shifts to the bergschrund (Haefeli, 1953, page 5; Haefeli & Brentani, 1954b, page 7). They observed there a large vertical velocity (Haefeli & Brentani, 1954b, page 7). They want to determine its position and to observe it. The main tunnel should never reach the bergschrund. The southern part of the ice tunnel Q100 has approximately a length of 40m, and the northern part is at least 80m long. The northern part of the tunnel Q100 (Fig. B.8) reaches approximately the boreholes 3C. The total length of the tunnel Q100 is 120m (Haefeli, 1953, page 5). The tunnel width is at least 1.20 m, and the height 2.00 m. In case of fear meeting some water-filled crevasses, they recommend predrilling to observe some presence of water and to drain the possible crevasses (Haefeli, 1953, page 6). The main goals of the transversal tunnels Q120 and Q100 were to determine a calmer area in the ice cap to relocate the main ice tunnel and to drain the water-filled crevasses (Haefeli & Schnitter, 1954, page 2). In 1955, they noticed a quick lengthening of the northern part of the tunnel Q100, which means a speed of 9cm/month. At the end of the tunnel, the northern motion was too big, that a crevasse has opened up in the bottom of the tunnel. However, the deformation visible in the circular profile K2 behaves normally (Haefeli, 1956, page 35). In 1958, they decided to drill four boreholes in the transversal tunnel, 2 in the northern part, and 1 or 2 in the southern part (Schnitter & Kasser, 1958, Appendix 1).

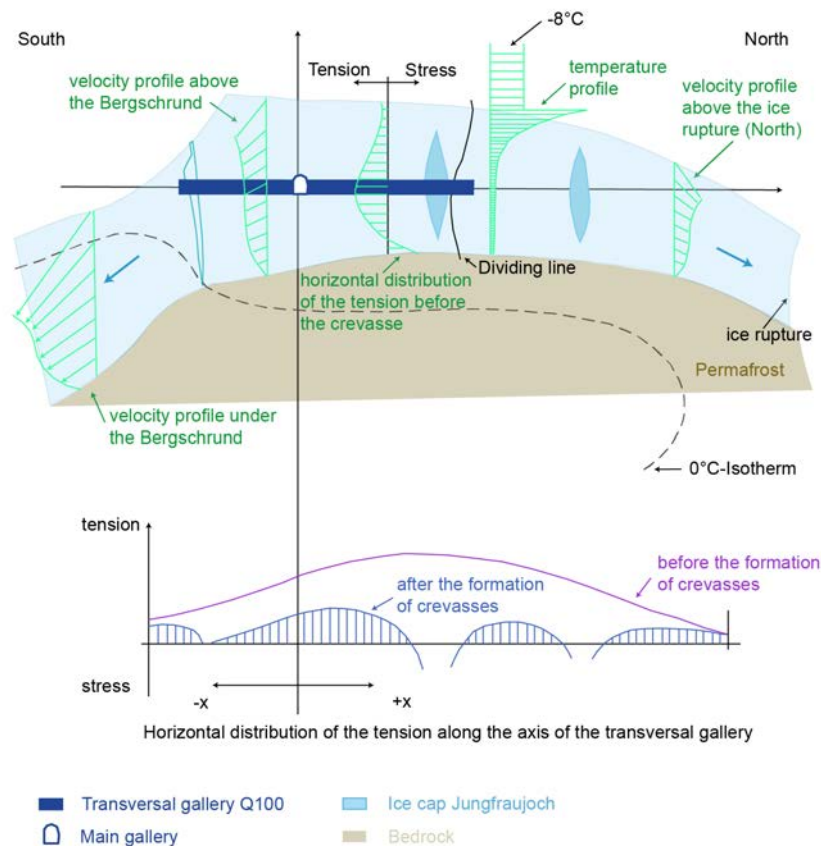


Figure 3.9 – Simplified schema of the transversal Q100 with the velocity profiles at different locations in the ice cap and the tension distribution in the ice cap (adapted from Haefeli & Brentani (1953, Appendix Figure 3c))

The access tunnel 2a (Fig. 3.4) lies at position 1.50. Its angle to the main ice tunnel is 53°C (Haefeli, 1953, p. 5).

A circular profile, named K_1 , was installed in the main ice tunnel to control the deformation of the ice tunnel (Fig. 3.4). The diameter of the circular profile is 2.90 m. This circular profile lies between the positions hm 1.24 and 1.30, and its length is 6m (Haefeli & Schnitter, 1954, page 8; Haefeli & Brentani, 1954a, page 400). The ice layer above the circular profile is 31m (Haefeli, 1956, page 9). These circular profiles enable the investigation of the plastic behavior of cold ice (Haefeli & Brentani, 1954b, page 29).

A circular profile, named K_2 , was installed in the transversal tunnel Q100 (Fig. 3.4) to investigate and to analyze the plastic deformation of cold ice (Haefeli & Schnitter, 1954, page 2). The circular profile lies between the positions 14.2m – 24.2m north of the main gallery, and its length is 10m. In the middle of this circular profile are installed eight measurement points, which means at position 19.2m. The ice layer above the circular profile is 25m (Haefeli, 1956, page 9).

For the drainage of the water-filled crevasses, a system of boreholes was installed every 10 meters in the ice walls and in the top of the tunnels. The boreholes have a length of 1 meter (Fig. B.7). These boreholes should be yearly controlled (Haefeli & Schnitter, 1954, page 5).

3.6 Choice of the Jungfraujoch

They systematically control the ice galleries and the ice cap for reasons of security, and they want to investigate the possibility of changing the position of the main ice gallery in a calmer region of the ice cap. The controls are also here to observe the evolution of the formation of water-filled crevasses in the ice cap (Haefeli, 1953, page 1; Haefeli & Brentani, 1954b, page 26). Moreover, there are cables in the main tunnel, and they need to understand better how ice behaves and creeps (Haefeli, 1956). After ten years of observations, they could have a better possibility to re-examine the flow law of ice (Haefeli, 1963, page 162).

Moreover, these measurements complete the measurements done in the temperate ice (such as in Zmutt or Mont Collon (Haefeli, 1963, page 163)) to investigate the plastic behavior of cold ice (Haefeli & Brentani, 1954b, page 29). They control if the measured deformations, the plastic behavior, and the states of stress coincide with the theory (Haefeli & Brentani, 1954a, page 394). With time, they want to know how the motion of the ice cap behaves inside and at the surface. They want to draw the real vector of speed (size and direction) and to determine the temporal variation of these vectors (Haefeli & Brentani, 1954a, page 400). In 1956/57, they built an experimental level for Greenland for an international glaciological expedition. It is useful to measure the snow height, firn growth of the ice cap, and to control the measurement of deformation in the long term (Haefeli, 1957, page 13).

The different measurements and observations done in the ice cap have a goal for scientific questions in glaciology and geophysics. It gives an opportune possibility to compare the data, and the results with the one gathered and observed in the ice cap of Greenland by the French expedition Victor (Haefeli, 1953, page 2; Haefeli & Brentani, 1954a, page 408, 1954b) and to investigate the tensions, the ice motion, and the ice temperature in a cold ice cap and the creep processes and the plasticity of cold ice (Haefeli & Brentani, 1954a, page 406, 1954b, page 1) from the Arctic and Antarctic (Haefeli & Brentani, 1954a, page 394). Moreover, they want to extrapolate the results of the Jungfraujoch to the ice cap of Groenland. Thanks to the results of the Jungfraujoch, they hypothesized that there is a core zone in the central Greenland where the ice does not slide on the rock, but it is freezing (Haefeli & Brentani, 1954a, page 408, 1954b, page 17; Robin, 1954). Then, the arisen shear stresses lie far under the breaking point. This implies that the core zone finds in the permafrost (Haefeli & Brentani, 1954b, page 17). The profile shape of Greenland's ice cap enables the re-examination of the validity of flow law in case of a small ice cap of a big ice cap (Haefeli, 1963, page 163).

Chapter 4

Methodology

4.1 Deformation measurements

The aims of deformation measurements in gallery cross-sections are to investigate the contraction of the circular profiles, to determine the deformations in the horizontal and vertical directions (Haefeli, 1953, page 8), and to identify the apparent viscosity of the ice cap (Haefeli & Schnitter, 1954, page 8). Moreover, these measurements give an insight into spatial movements inside the ice cap and enable to determine a temporal variation (Haefeli & Brentani, 1954b). The time interval between each measurement should capture the seasonal oscillations of the deformations (Haefeli, 1953, page 8). Three measurement campaigns were realized between 1950 and 2020 at different locations in the ice galleries. In total, four circular profiles were investigated, i.e., three in the principal gallery and one in the cross gallery Q_{100} .

4.1.1 Description of the four circular profiles

In order to systematically control the change of cross-section of the principal ice gallery, the principal gallery was excavated circularly between the locations hm 1.24 and hm 1.30 in 1951. The diameter of this circular profile is 2.9 m, and the length is 6.0 m (Haefeli & Schnitter, 1954, page 8). Between the locations hm 1.24 and hm 1.30, a circular profile K_1 was installed. The ice cover above the circular profile K_1 is approximately 30m (Haefeli & Brentani, 1954b, page 6). According to the georeferenced plan (Fig. 3.5), the ice cover has a thickness of 28m above the circular profile. Thanks to the information of the ice cover above the profile K_1 , the circular profile K_1 is assumed to be installed approximately at the location hm 1.25. The measurements were realized from 20.02.1951 to 08.01.1953, i.e., during 688 days. The deformation was in total measured seven times. The time interval between each measurement is not periodic.

Similarly to the profile K_1 , the northern part of the cross gallery Q_{100} was excavated circularly between the locations m 14.2 and m 24.2. The diameter of this circular profile is 2.6m, and the length is 10m. The circular profile K_2 was installed at the position m 19.2. The ice cover above the circular profile K_2 is 25m (Haefeli, 1956). The measurements were realized from 29.08.1954 to 15.04.1957, i.e., during 584 days. The deformation was in total measured 10 times for three couples of survey points and 4 times for a couple of survey points. The time interval between each measurement is not periodic.

On 04.12.2019, two profiles, K_3 and K_4 , were installed in the principal ice gallery. The deformation was measured on 06.07.2020, i.e., after 64 days. In comparison to the two above-mentioned profiles, these new profiles are not perfectly circular. The vertical length was respectively approximately 2.5m and 2.686m, for K_3 and K_4 . The horizontal length was respectively approximately 2.696m and 2.978m, for K_3 and K_4 . The profile K_3 is approximately at the position hm 0.938, and The profile K_4 is approximately at the position hm 1.384. Both profiles are separated at a distance of 44.6m. According to the georeferenced plan (Fig. 3.6), the ice cover above the profile K_3 has a thickness of 16m and above the profile K_4 20m.

4.1.2 Methodology

Profile K_1 and Profile K_2

No information has been found in the different available reports about the method of the measurements done between 1951 and 1953. However, it is assumed that the method used for the measurements done between 1951 and 1953 is the same as the one for the measurements done between 1954 and 1957. Eight screws were inserted in the ice wall by drawing an octagon. These eight screws correspond to the survey points. To not influence the measurements with the ice evaporation of the ice wall surface, 15 cm screws were chosen (Haefeli, 1956, page 9). The length change between two survey points was measured using a steel measuring tape (Haefeli, 1953, page 7). In the construction schedule of 1953 (Haefeli, 1953), it was mentioned that periodical monitoring and measurements of the ice galleries should be done at least 2 times per year. These monitoring and measurements were achieved by the engineer Brentani of the company Rothpletz, Lienhard and Cie. In the available data, the measurements were done many times between 1951 and 1953 and between 1954 and 1957, however not regularly.

Profile K_3 and Profile K_4

For the profiles K_3 and K_4 (Fig. 4.1 and 4.2), seven screws were inserted in the ice wall by drawing a heptagon. On 04.12.2019, the distance between many couples of survey points was measured in order to rebuild the figure graphically. Two different methods were tested. The first method used a tape measure. The second method used a laser. The profile K_3 was measured by means of a tape measure and a laser. It was noticed that the method with the tape measure was less precise than the method with the laser. All the measurements have been thus realized with the laser. For each couple of survey points, at least three measurements were taken to minimize the imprecision.



Figure 4.1 – Circular profile K_4 taken from the entrance of the gallery (photo taken on 06.02.2020 (S. Morard))

To realize the measurements with the laser, a little cork ball was put on a screw. The screw with the cork ball was designed as the target. The cork ball has a diameter of 30mm and adds a

distance of 14mm to the screw. The bottom of the laser was put down on the other screws and was directed towards the target. The distance between the screw and the target was measured. This operation was realized many times with different couples of survey points.



Figure 4.2 – Circular profile K_4 taken from the entrance of the gallery (photo taken on 06.02.2020 (S. Morard)). Zoom on the survey points 2, 3, 5 and 6.

To visualize the heptagon the mean of each measurement between two survey points is calculated. Then, these means (see Appendix C.1 and C.2) have been written in a text file. The text file is imported and read like a list in a python script. Then, the names of each column are determined. There are three variables: start survey point, end survey point, the distance between these two points. The second step is to distribute the different survey points on a circle. The survey points have been distributed as the shape of a heptagon. It means that the central angle is $\frac{360^\circ}{7} = 51.42^\circ$. The central angle has been shifted from an angle of 117° so that the survey points 1 and 7 are on the x-axis. The survey point 7 is defined with the following coordinates (0,0). The next step is to determine the potential coordinates of the survey points. The coordinate x is the sine of the angle, and the coordinate y is the cosine of the angle. The coordinates are multiplied by a factor of 1500. This factor 1500 corresponds to the radius of the gallery, i.e. 1500mm. Thanks to a loss function, the best position of the six other points is calculated. A loss function determines the error between the measured distance and the distance calculated by the python script. This python script has been written by Martin Lüthi. All these operations were repeated for the measurements of the 06.02.2020.

Postprocessing of data

The three data sets of these four circular profiles do not present the same variables. In order to compare the different values, the data of each measurement campaign is post-processed. For each data set, the measurement point i between two screws m and n , the date T , the time interval ΔT , the diameter D , the change in diameter ΔD_{mn} , the cumulative change in diameter $\Delta D_{mn_{cum}}$, the strain δD_{mn} and the strain rate $\delta \dot{D}_{mn}$ are calculated as following :

$$\text{Time interval [days]: } \Delta T_{i+1} = T_{i+1} - T_i \quad (4.1.1)$$

$$\text{Change in diameter [mm]: } \Delta D_{mn_{i+1}} = D_{mn_i} - D_{mn_{i+1}} \quad (4.1.2)$$

$$\text{Cum. change in diameter [mm]: } \Delta D_{mn_{cum,i+1}} = \sum_1^i \Delta D_{mn_{i+1}} \quad (4.1.3)$$

$$\text{Strain [\%]: } \delta D_{mn_{i+1}} = \frac{\Delta D_{mn_{i+1},cum}}{D_{mn_1}} \quad (4.1.4)$$

$$\text{Strain rate [\%/day]: } \delta \dot{D}_{mn_{i+1}} = \frac{\delta D_{mn_{i+1}}}{\Delta T_{i+1}} \cdot 100\% \quad (4.1.5)$$

In addition to the variables presented above, the coordinates X and Y, the horizontal and vertical changes (respectively dx and dy) from 04.12.2019 to 06.02.2020 are presented for the survey points of the profiles K_3 and K_4 .

$$\text{Horizontal change [mm]: } dx = X2_i - X1_i \quad (4.1.6)$$

$$\text{Vertical change [mm]: } dy = Y2_i - Y1_i \quad (4.1.7)$$

$$\text{Length change [mm]: } D = \sqrt{dx^2 + dy^2} \quad (4.1.8)$$

$$\text{Horizontal velocity [mm/day]: } v_x = dx/\Delta T \quad (4.1.9)$$

$$\text{Vertical velocity [mm/day]: } v_y = dy/\Delta T \quad (4.1.10)$$

$$\text{Velocity [mm/day]: } v = \sqrt{v_x^2 + v_y^2} \quad (4.1.11)$$

X2 and Y2 correspond to the coordinates of the profile measured on 06.02.2020, and X1 and Y1 correspond to the coordinates of the profile measured on 04.12.2019. The index i corresponds to the survey point.

The apparent viscosity μ was not available for each measurement. For some measurements, the apparent viscosity μ has been calculated with the following equations (eq. 4.1.12 to 4.1.14).

$$\text{Hydrostatic pressure } \left[\frac{kg}{m^2} \right]: \sigma_1 = \rho_i \cdot g \cdot h \quad (4.1.12)$$

The parameter h corresponds to the height above the ice gallery and ρ_i is the ice density. The ice density ρ_i is chosen as $850 \frac{kg}{m^3}$ for the circular profiles K_1 and K_2 and as $900 \frac{kg}{m^3}$ for the circular profiles K_3 and K_4 .

Then, the horizontal specific strain rate ϵ_y is determined as:

$$\text{Specific strain rate } \left[\frac{\%}{day} \right]: \epsilon_y = \frac{\delta D_{hor}}{\Delta T} \quad (4.1.13)$$

The parameter δD_{hor} corresponds to the final horizontal deformation, and ΔT corresponds to the entire period of the measurement campaigns. The equation (4.1.14) is given by Haefeli and Brentani (1954b).

$$\text{Apparent viscosity [Pa} \cdot \text{s]: } \mu = \frac{\sigma_1}{2 \cdot \epsilon_y} \quad (4.1.14)$$

4.2 Temperature

The measurements of temperature were assumed to be realized using thermistors or thermometers. For the air temperature at Sphinx, the air temperature is measured by MeteoSwiss, that possesses a weather station.

To measure the temperature in the ice and at the surface contact between the rock and the ice, they used different systems. Firstly, they drilled a borehole, where they install thermocouples (Schnitter & Kasser, 1958, page 11), thermistors or contact thermometers (Schnitter & Kasser, 1958, page 11; Vöggtli, 1959, page 2). The precision of the thermistor was 0.1°C (Schnitter & Kasser, 1958, page 11; Vöggtli, 1959, page 4). They probably used the NTC-thermistor (Negative Temperature Coefficient thermistor) (Vöggtli, 1959, page 3). To measure the temperature at the surface contact between the ice and the rock, they let the apparatus for 24 days. After 17 days, the temperature stabilized. They measured more or less at the same time (9 a.m. or 10 a.m.). On 09.11.1958, they measured during the afternoon (4 p.m.). To measure the ice temperature, they waited between 2 and 6 days for the temperature stabilization (Vöggtli, 1959, page 12). Ice temperature was measured at different locations along the main gallery. Ten boreholes were drilled with thermistors (Fig. 5.7). The thermistors measured the temperature at the ice surface. For the borehole 3, 4 thermistors measured the ice temperature. A thermistor measured the temperature at the contact surface between the rock and the ice, another 5m above the rock, the third one 10m above the rock and the last one 15m above the rock (Fig. 5.8). To measure the temperature along the gallery walls, they used a thermistor. It is like a tracer pin with a thermistor at the end of this tracer pin. The precision of this system is 0.8°C for a range of temperatures between -20°C and 60°C (Vöggtli, 1959, page 17). They measure the temperature at the ice surface of the wall gallery on 17.10.1958 and 10.12.1958. For more details about the calibration and the methodology of their temperature measurements, it is recommended to read the report of Vöggtli (1959). They describe and explain, what they did with more detail.

In 2020, the ice temperature was measured at 4 different locations. Three holes of a depth of approximately 11m were drilled in the bottom of the ice gallery and one in the ice wall. Then, a chain of thermistors, which has a thermistor every 0.5m, was installed on stakes of 12 meters (Fig. 4.3). The loggers have been let a certain time to stabilize the temperature.



Figure 4.3 – Ice temperature measurements in the wall and in the bottom of the main ice gallery (photo taken on 06.02.2020 (S. Morard)).

4.3 Ice density

No information is presented in the different reports to explain or to justify the choice of $850\text{kg}/\text{m}^3$ for the ice density. On 06.02.2020, a try to determine the ice density of the ice gallery has been conducted. Some ice is grabbed in the wall with an ice driller. This volume V of ice (eq. 4.3.1) is collected in a bag. The mass of the empty bag m_{eb} is 0.041kg. The hole in the ice wall has a depth h of 0.45m and a diameter d of 0.05m.

$$\text{Volume [m}^3\text{]: } V = \pi \cdot \left(\frac{d}{2}\right)^2 \cdot h \quad (4.3.1)$$

The mass of the bag filled m_b is 0.9101 kg. The mass of ice m_i can be determined with the following equation:

$$\text{Ice mass [kg]: } m_i = m_b - m_{eb} \quad (4.3.2)$$

Then, the ice density ρ_i is determined with the following equation:

$$\text{Ice density } \left[\frac{\text{kg}}{\text{m}^3}\right]: \rho = \frac{m_i}{V} \quad (4.3.3)$$

4.4 Modelling

4.4.1 Creation of the meshes for the circular profiles

For the modelling of the vertical and horizontal deformations of the ice galleries at the Jungfraujoch, the ice galleries are represented with a mesh (Fig. 4.4). For each gallery, different meshes were generated (Table 4.1). The meshes have different widths: 10m, 20m, 60m, 100m and 120m. It enables to test the influence of the boundary conditions on the deformations. The thickness of the meshes is 1m.

The mesh for the circular profile K_1 has a maximal height of 28m and a minimum height of -20m. The radius of the hole is 1.45m. The mesh for the circular profile K_2 has a maximal height of 25m and a minimum height of -20m. The radius of the hole is 1.3m. The mesh for the circular profile K_3 has a maximum height of 16m and a minimum height of -20m. The radius of the hole is 1.3m. The mesh for the circular profile K_4 has a maximum height of 20m and a minimum height of -6m. The radius of the hole is 1.4m. All these parameters have been derived from the georeferenced plan (Fig. 3.5 and 3.6). The coordinate (0,0,0)m locates in the center of the hole (Fig. 4.4).

Circular profile	K_1	K_2	K_3	K_4
Thickness (x-axis)	[0; 1] m	[0; 1] m	[0; 1] m	[0; 1] m
$Width_1$ (y-axis)	-	-	[-5; 5] m	[-5; 5] m
$Width_2$ (y-axis)	[-30; 30] m	[-30; 30] m	[-10; 10] m	[-10; 10] m
$Width_3$ (y-axis)	[-50; 50] m	[-50; 50] m	[-30; 30] m	[-30; 30] m
$Width_4$ (y-axis)	[-60; 60] m	[-60; 60] m	[-50; 50] m	[-50; 50] m
Height (z-axis)	[-20; 28] m	[-20; 25] m	[-19; 16] m	[-6; 20] m
Radius	1.45 m	1.30 m	1.30 m	1.40 m

Table 4.1 – Summary of the mesh size

The meshes have been generated in Gmesh (Fig. 4.4). Martin Lüthi provided the following script (Fig. C.1). Lines 3-5 define the size of the mesh (table 4.1). Line 8 defines the radius of the ice gallery (table 4.1). The parameters Lc1 and Lc2 are the distances between the nodes. Lines 13 and 14 define the bottom of the glacier. Lines 18 and 19 define the glacier surface. Lines 21-24 create a rectangle, i.e. the first face of the glacier section. Then, lines 27-31 define the points to create (lines 33-36) the ice gallery in the ice mass. For the rectangle frame, the nodes are spaced with a distance of 2m (Fig. 4.4). For the circle frame, the nodes are spaced with a distance of

0.2m. Lines 38-41 creates the second face of the mesh. Line 43 places the second face of the mesh 1m behind the first face. Then, we get a volume of the glacier section with the ice gallery. Lines 45-51 define each face of the mesh for MOOSE. The meshes are adapted for each circular profile according to the table 4.1.

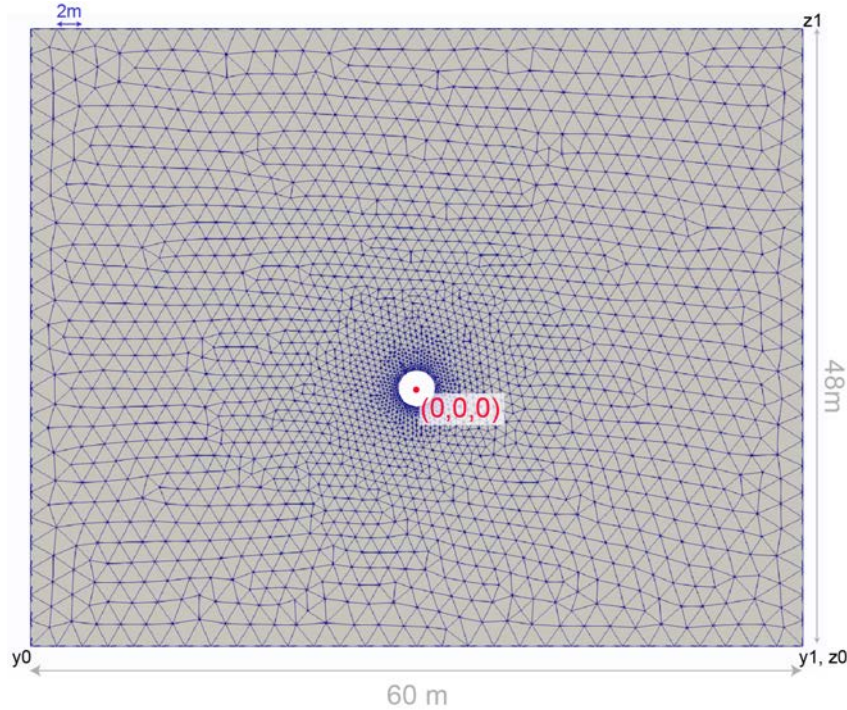


Figure 4.4 – Mesh for the circular profile K_1 with a width of 60m.

4.4.2 Import of the mesh in MOOSE

To visualize the deformations in the modelling, the nodes of the hole should be determined. The identity of the nodes can be read in ParaView. ParaView gives three names for the node: Id, GlobalNodeId, and PedigreeNodeId (Fig. 4.5). The Id is one unit smaller than GlobalNodeId and PedigreeNodeId. GlobalNodeId and PedigreeNodeId give the same name. To make sure that MOOSE begins to calculate from 1 and not from 0, a little test was realised. Instead of modelling with the ice gallery mesh, the model was run with a simple square mesh (Fig. 4.5). The node identities 0 and 2 for the displacements in y-direction were chosen in MOOSE and in ParaView. Then, it is possible to compare the results for the displacements. For the timestep $t=0.1$ year, the displacement y for the node identity 0 is $-4.74796 \cdot 10^{-6}$ m in MOOSE and in ParaView and for the node identity 2 the displacement y is $-3.45875 \cdot 10^{-6}$ m. This test was also realised with other timesteps. For every tested timestep, the *id* from Paraview corresponds to the *nodeid* from MOOSE.

To read the displacements from nodes in MOOSE, it is possible to use the function *NodalVariableValue*¹ in the postprocessor block. As cite in MOOSE Framework (2020), the *NodalVariableValue* postprocessor is used "in order to obtain the value of a nodal variable at a particular location (i.e., temperature and displacement)" and "to compare against experimental data". For this block, three parameters are required : *type*, *variable*, and *nodeid*. The *type* correspond to the output from this postprocessor. In this case, it is *NodalVariableValue*. Then, the *variable* is defined. Here, it is the displacement in some direction. For the vertical deformation, the *variable* is *disp_z*. For the horizontal deformation, the *variable* is *disp_y*. The last required parameter is *nodeid*. It is the name of the node (Id) in ParaView. For each mesh, the node identities of these points (0,0,r) and (0,0,-r) were read for the vertical deformations and the node identities of these points (0,r,0) and (0,-r,0) were read for the horizontal deformations (Fig. 4.6). The name of the node identities changes, when the mesh size changes.

1. Read for more details : <https://mooseframework.org/source/postprocessors/NodalVariableValue.html>

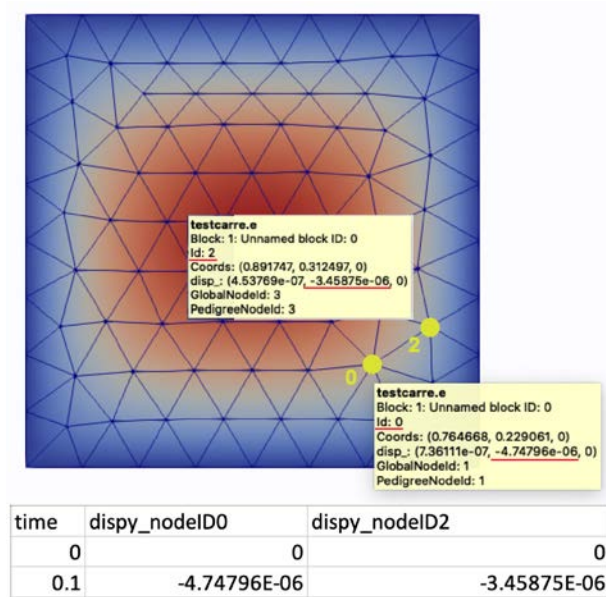
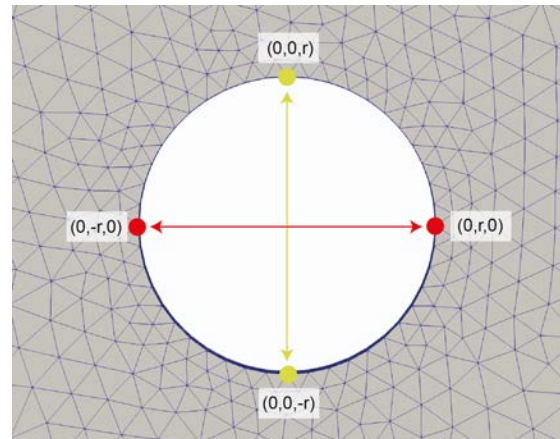
Figure 4.5 – Square mesh at the timestep $t=0.1$ year

Figure 4.6 – Hole of the ice gallery. The points represent the nodes. The red line and points represent the horizontal deformation. The yellow line and points represent the vertical deformation.

4.4.3 Modelling

In MOOSE, many models are already written. To answer the research questions, many models from the physic module *tensor mechanics* were tested. The first tested models were viscous models as Maxwell and Kelvin-Voigt models (see Appendix C). The second tested models were plane strain models. The third tested models were creep models. The creep model represents best the experimental data of the different circular profiles. In every model, the parameters were tuned to get a linear relation between the time and the strain. The final chosen model is a creep model. It is an adaptation of the model *combined_creep_plasticity.i* from MOOSE (see Appendix C).

4.4.4 Comparison with the experimental data

To make sure that the modelling results are correct, the results are compared with the data gathered in the 1950s and 2020 (see Chapter 5). The modelled and measured data are plotted on the same plot. However, the data from the 1950s are not given in centimeters but in %, because they gave the strain δ . Firstly, these data were adapted in length change H (eq. 4.4.1).

$$\text{Length change [m]: } H = \frac{\delta \cdot H_0}{100\%} \quad (4.4.1)$$

MOOSE does not give the deformation of the hole. It gives only the displacement of the nodes. Then, the displacement between the two nodes are subtracted. For the horizontal deformation, the nodes (0,r,0) and (0,-r,0) are subtracted. For the vertical deformation, the nodes (0,0,r) and (0,0,-r).

4.4.5 Sensitivity of the parameters

To test the influence of each parameter in the modelling and to find the best fit to represent the experimental data, many modellings have been run with changing only one parameter. The basis modelling has the following parameters :

- Ice density: $\rho = 850 \frac{kg}{m^3}$ for the 1950s and $\rho = 900 \frac{kg}{m^3}$ for 2020
- Young's modulus : $E = 8700$ MPa
- Poisson's ratio : $\nu = 0.31$
- A factor : $A = 65 \frac{a^{-1}}{MPa^{-3}}$
- n exponent : $n = 3$
- m exponent : $m = 0$

The first test was to change only the width of the mesh (10m, 20m, 60m, 100m, and 120m). The parameters above remain the same. The second test was to change the Young's modulus (8700 MPa, 870 MPa, 87 MPa, and 8.7 MPa). The third test was to change the n exponent (3 and 4). The fourth test was to change the m exponent (3, 2, 1, and 0). The last test was to change the A factor ($10 \frac{a^{-1}}{MPa^{-3}}$, $30 \frac{a^{-1}}{MPa^{-3}}$, $50 \frac{a^{-1}}{MPa^{-3}}$, and $65 \frac{a^{-1}}{MPa^{-3}}$). These different tests are done for every circular profile. Then, the boundary conditions were modified. Until now, the boundary conditions are 0 for the right, left, and bottom sides of the mesh for the $disp_y$. Then, the boundary conditions have velocities for the left and right sides of the mesh.

Chapter 5

Data

5.1 Profile K_1

The data for the profile K_1 (Fig. 5.1) come from the report written by Haefeli and Schnitter (1954, Appendix Figure 8). The given values by Haefeli and Schnitter (1954, Appendix Figure 8) describe only the measurements of the vertical deformation between the survey points 4 and 8 (Table 5.1) and the horizontal deformation between the survey points 2 and 6 (Table 5.2). To determine the coordinates (Table D.1) and the displacements (Table D.2-D.4) of each survey points for the three periods of measurements (see Chapter 4), the figure of the circular profile K_1 is digitized (Fig. 5.1). The vertical deformations between the survey points 3 and 1, 4 and 8, 5 and 7 (Table D.5), the horizontal deformations between the survey points 3 and 5, 2 and 6, 1 and 7 (Table D.6), the oblique deformations between the survey points 3 and 7, 5 and 1 (Table D.7) are also determined using the digitization.

The ice cover above the circular profile K_1 is 28m. The stress σ of the ice cover on the circular profile is $233'478kg/m^2$. The deformation of the circular profile was measured for 688 days. The horizontal specific strain rate ϵ_y is $0.003\%/day$. The viscosity μ is $3.47 \cdot 10^{14} Pa \cdot s$.

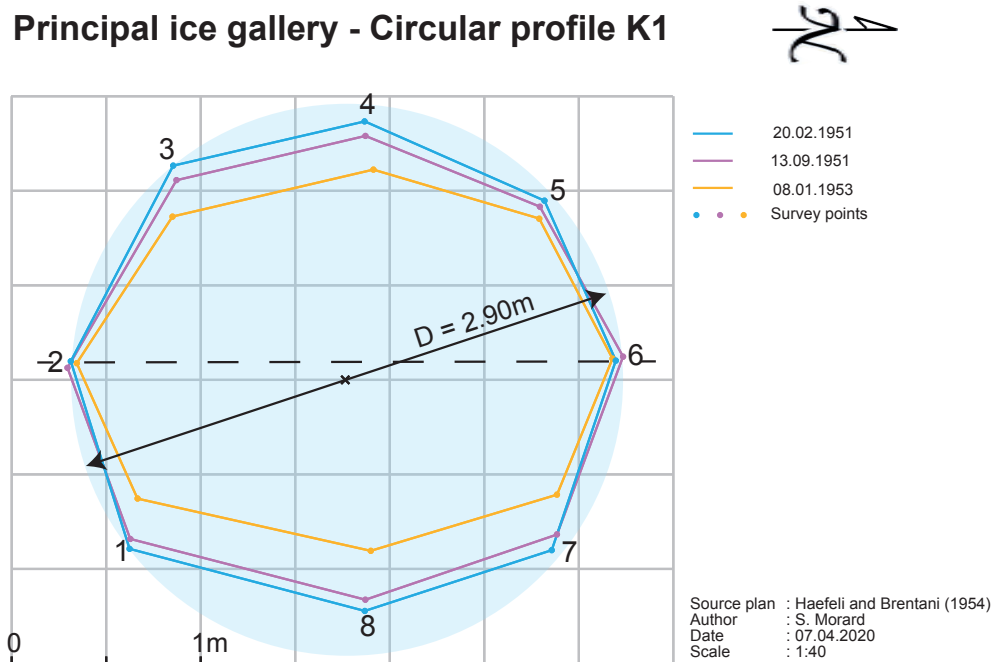


Figure 5.1 – Circular profile K_1 at three different time periods (20.02.1951, 13.09.1951, 08.01.1953)

5.1.1 Vertical deformation

The initial vertical distance between the survey points 4 and 8, measured by Haefeli and Schnitter (1954, Appendix Figure 8), is 2604 mm (Table 5.1). In 688 days, the diameter shortens of 534mm, 20.5% of its initial length. The mean strain rate is $-20.5\%/688 \text{ days} = -0.03\%/day = -10.9\%/year$. According to Table 5.1, the strain rate is constant and is equal to the mean strain rate except for the 5th measurement. From 16.08.1951 to 21.08.1951, the deformation accelerates.

i	T	ΔT	D_{48}	ΔD_{48}	$\Delta D_{48,cum}$	δD_{48}	$\delta \dot{D}_{48}$
[–]	[–]	[days]	[mm]	[mm]	[mm]	[%]	[%/day]
1	20.02.51	0	2604	0	0	0.0	0.00
2	15.03.51	23	2587	-17	-17	-0.7	-0.03
3	05.05.51	51	2545	-42	-59	-2.3	-0.03
4	16.08.51	103	2465	-80	-139	-5.3	-0.03
5	21.08.51	5	2441	-24	-163	-6.3	-0.18
6	13.09.51	23	2422	-19	-182	-7.0	-0.03
7	08.01.53	483	2070	-352	-534	-20.5	-0.03

Table 5.1 – Profile K_1 : Measured vertical deformation from 20.02.1951 to 08.01.1953 (data taken and adapted from Haefeli and Schnitter (1954, Appendix Figure 8))

5.1.2 Horizontal deformation

The initial horizontal distance between survey points 2 and 6, measured by Haefeli and Schnitter (1954, Appendix Figure 8), is 2931 mm (Table 5.2). In comparison to the vertical deformation (Table 5.1), the horizontal deformation is not constant in time. The horizontal deformation alternates between a process of contraction (negative distance) and a process of extension (positive distance). The diameter shortens of 580 mm, the 2% of its initial length. The mean strain rate is $-1.98\%/688 \text{ days} = -0.003\%/day = -1.05\%/year$.

i	T	ΔT	D_{26}	ΔD_{26}	$\Delta D_{26,cum}$	δD_{26}	$\delta \dot{D}_{26}$
[–]	[–]	[days]	[mm]	[mm]	[mm]	[%]	[%/day]
1	20.02.51	0	2931	0	0	0.00	0.00
2	15.03.51	23	2932	1	1	0.03	0.001
3	05.05.51	51	2927	-5	-4	-0.14	-0.003
4	16.08.51	103	2950	23	19	0.65	0.006
5	21.08.51	5	2921	-29	-10	-0.34	-0.068
6	13.09.51	23	2990	69	59	2.01	0.087
7	08.01.53	483	2873	-117	-58	-1.98	-0.004

Table 5.2 – Profile K_1 : Measured horizontal deformation from 20.02.1951 to 08.01.1953 (data taken from Haefeli and Schnitter (1954, Appendix Figure 8))

5.2 Profile K_2

The data for the profile K_2 (Fig. 5.2) come from the report written by Haefeli (1956, Appendix 3; 1957, page 8 and Appendix 3). The given values by Haefeli (1956, Appendix 3; 1957, page 8 and Appendix 3) describe only the measurements of the vertical deformation between the survey points 5 and 8 (Table 5.3), the horizontal deformation between the survey points 3 and 7 (Table 5.4), and the oblique deformations between the survey points 1 and 4 (Table 5.5) and the survey points 2 and 6 (Table 5.6). To determine the coordinates (Table D.8) and the displacements (Tables D.9-D.12) of each survey points at the four periods of measurements (see Chapter 4), the figure of the circular profile K_2 is digitized (Fig. 5.2). The vertical deformations between the survey points 3 and 1, 4 and 8, 5 and 7 (Table D.13), the horizontal deformations between the survey points 3 and 5, 2 and 6, 1 and 7 (Table D.14), the oblique deformations between the survey points 3 and

7, 5 and 1 (Tables D.15 and D.16) are also determined using the digitization.

The ice cover above the circular profile K_2 is 25m (Haefeli, 1956, page 9) and the stress σ of the ice cover on the circular profile is $208'462.5 \text{ kg/m}^2$. The deformation of the circular profile was measured for 960 days. The horizontal specific strain rate ϵ_y is $0.006\%/day$. The viscosity μ is $1.50 \cdot 10^{14} \text{ Pa} \cdot s$.

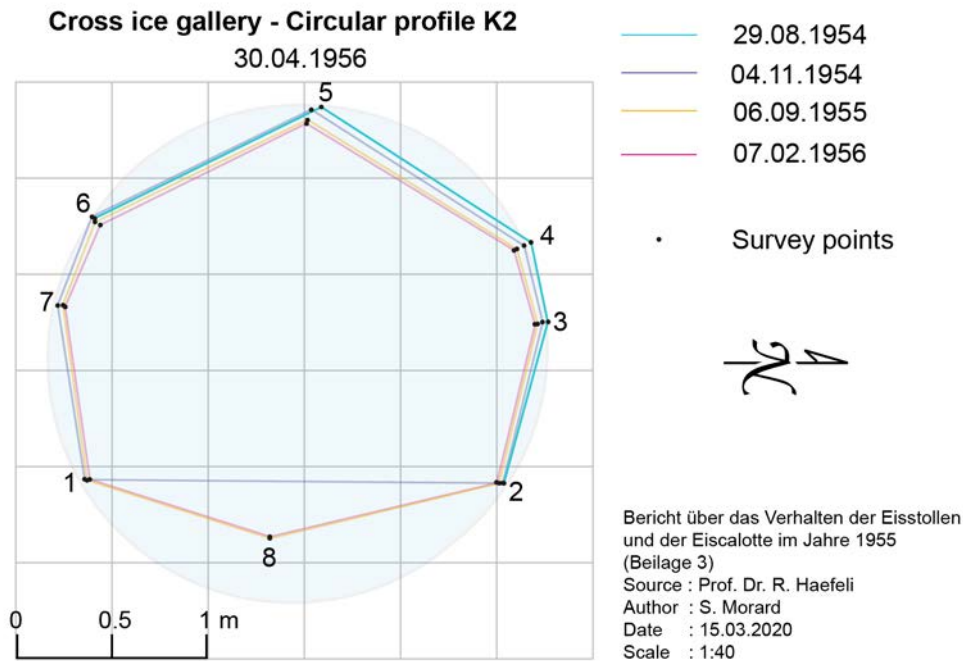


Figure 5.2 – Circular profile K_2 at four different time periods (29.08.1954, 04.11.1954, 06.09.1955, 07.02.1956)

5.2.1 Vertical deformation

The initial vertical distance between the survey points 5 and 8, measured by Haefeli (1956, Appendix 3; 1957, page 8 and Appendix 3), is 2215 mm (Table 5.3). In 584 days, the diameter shortens of 116 mm, 5.2% of its initial length. The mean strain rate is $-5.2\%/584 \text{ days} = -0.009\%/day = 3.2\%/year$. According to Table 5.3, the strain rate is rather constant and is equal to the mean strain rate.

5.2.2 Horizontal deformation

The initial horizontal distance between survey points 3 and 7, measured by Haefeli (1956, Appendix 3; 1957, page 8 and Appendix 3), is 2545 mm (Table 5.4). In 893 days, the diameter shortens of 142mm, 5.6% of its initial length. The mean strain rate is $-5.6\%/893 \text{ days} = -0.006\%/day = -2.3\%/year$. According to Table 5.4, the strain rate is more or less constant and is equal to the mean strain rate.

5.2.3 Oblique deformation

The initial oblique deformation between the survey points 1 and 4 is 2584 mm (Table 5.5). In 893 days, the length shortens of 167 mm, 6.5% of its initial length. The mean strain rate is $-6.5\%/893 \text{ days} = -0.007\%/day = -2.7\%/year$.

The initial oblique deformation between the survey points 2 and 6 is 2615 mm (Table 5.6). In 893 days, the length shortens of 146 mm, 5.6% of its initial length. The mean strain rate is $-5.6\%/893 \text{ days} = -0.006\%/day = -2.3\%/year$.

i	T	ΔT	D_{58}	ΔD_{58}	$\Delta D_{58,cum}$	δD_{58}	$\delta \dot{D}_{58}$
[–]	[–]	[days]	[mm]	[mm]	[mm]	[%]	[%/day]
1	29.08.54						
2	04.11.54						
3	21.02.55						
4	01.04.55						
5	22.07.55						
6	06.09.55						
7	09.09.55	0	2215	0	0	0	0
8	07.02.56	151	2182	-33	-33	-1.5	-0.009
9	18.10.56	254	2135	-47	-80	-3.6	-0.008
10	15.04.57	179	2099	-36	-116	-5.2	-0.009

Table 5.3 – Profile K_2 : Measured vertical deformation from 09.09.1955 to 15.04.1957 (data taken and adapted from Haefeli (1956, Appendix 3; 1957, page 8 and Appendix 3))

i	T	ΔT	D_{37}	ΔD_{37}	$\Delta D_{37,cum}$	δD_{37}	$\delta \dot{D}_{37}$
[–]	[–]	[days]	[mm]	[mm]	[mm]	[%]	[%/day]
1	29.08.54		2555				
2	04.11.54	0	2545	0	0	0	0
3	21.02.55	109	2528	-17	-17	-0.7	-0.006
4	01.04.55	39	2523	-5	-22	-0.9	-0.005
5	22.07.55	112	2506	-17	-39	-1.5	-0.006
6	06.09.55	46	2499	-7	-46	-1.8	-0.006
7	09.09.55						
8	07.02.56	154	2473	-26	-72	-2.8	-0.007
9	18.10.56	254	2432	-41	-113	-4.4	-0.006
10	15.04.57	179	2403	-29	-142	-5.6	-0.006

Table 5.4 – Profile K_2 : Measured horizontal deformation from 04.11.1954 to 15.04.1957 (data taken and adapted from Haefeli (1956, Appendix 3; 1957, page 8 and Appendix 3))

i	T	ΔT	D_{14}	ΔD_{14}	$\Delta D_{14,cum}$	δD_{14}	$\delta \dot{D}_{14}$
[–]	[–]	[days]	[mm]	[mm]	[mm]	[%]	[%/day]
1	29.08.54		2625				
2	04.11.54	0	2584	0	0	0	0
3	21.02.55	109	2564	-20	-20	-0.8	-0.007
4	01.04.55	39	2557	-7	-27	-1.0	-0.007
5	22.07.55	112	2537	-20	-47	-1.8	-0.007
6	06.09.55	46	2528	-9	-56	-2.2	-0.008
7	09.09.55						
8	07.02.56	154	2498	-30	-86	-3.3	-0.008
9	18.10.56	254	2453	-45	-131	-5.1	-0.007
10	15.04.57	179	2417	-36	-167	-6.5	-0.008

Table 5.5 – Profile K_2 : Measured oblique deformation between the survey points 1 and 4 from 04.11.1954 to 15.04.1957 (data taken and adapted from Haefeli (1956, Appendix 3; 1957, page 8 and Appendix 3))

i	T	ΔT	D_{26}	ΔD_{26}	$\Delta D_{26,cum}$	δD_{26}	$\delta \dot{D}_{26}$
[-]	[-]	[days]	[mm]	[mm]	[mm]	[%]	[%/day]
1	29.08.54		2595				
2	04.11.54	0	2615	0	0	0	0
3	21.02.55	109	2598	-17	-17	-0.7	-0.006
4	01.04.55	39	2592	-6	-23	-0.9	-0.006
5	22.07.55	112	2574	-18	-41	-1.6	-0.006
6	06.09.55	46	2568	-6	-47	-1.8	-0.005
7	09.09.55						
8	07.02.56	154	2522	-46	-93	-3.6	-0.011
9	18.10.56	254	2502	-20	-113	-4.3	-0.003
10	15.04.57	179	2469	-33	-146	-5.6	-0.007

Table 5.6 – Profile K_2 : Measured oblique deformation between the survey points 2 and 6 from 04.11.1954 to 15.04.1957 (data taken and adapted from Haefeli (1956, Appendix 3; 1957, page 8 and Appendix 3))

5.3 Profile K_3

The data for the profile K_3 (Fig. 5.3) come from the measurements done at the Jungfraujoeh on 04.12.2019 and 06/07.02.2020. The table 5.7 presents the coordinates of each survey point and the displacements of these coordinates. The coordinates were calculated using a script Python (see Chapter 4.1.2). The magnitude of the displacement in the x-direction is of few millimeters and in the y-direction is of few centimeters. The table 5.8 presents the vertical deformation between the survey point 4 and the bottom of the ice gallery, the table 5.9 the horizontal deformation between the survey points 2 and 6, the table 5.10 the oblique deformation between the survey points 1 and 5, the table 5.11 the oblique deformation between the survey points 3 and 6, and the table 5.12 the oblique deformation between the survey points 3 and 7.

The ice cover above the circular profile K_3 is 16 meters. The stress σ of the ice cover on the circular profile is $141'264 kg/m^2$. The deformation of the circular profile was measured for 64 days. The horizontal specific strain rate ϵ_y is $0.01\%/day$. The viscosity μ is $6.10 \cdot 10^{13} Pa \cdot s$.

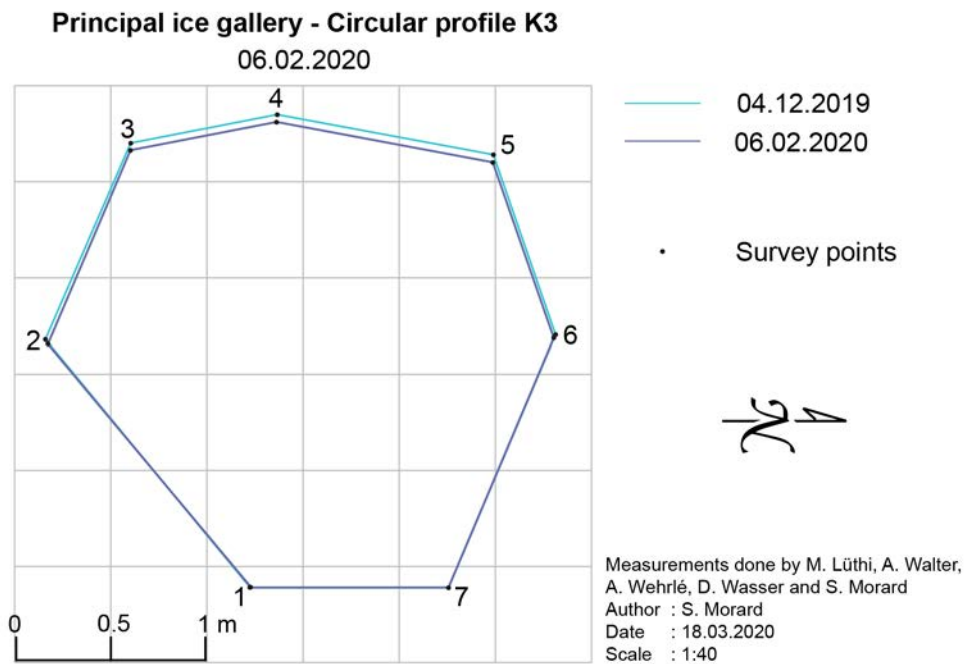


Figure 5.3 – Circular profile K_3 at two different time periods (04.12.2019 and 06.02.2020)

5.3.1 Positions and displacements of the survey points

i	X_1	Y_1	X_2	Y_2	dx	dy	D	v_x	v_y	v
[–]	[–]	[mm]	[mm]	[mm]	[mm]	[mm]	[mm]	[mm/day]	[mm/day]	[mm/day]
1	-1049	0	-1043	0	6	0	6	0.09	0	0.09
2	-2130	1312	-2117	1287	13	-25	28	-0.20	-0.39	0.44
3	-1680	2349	-1681	2312	-1	-37	37	-0.02	-0.58	0.58
4	-906	2500	-909	2461	-3	-39	39	-0.05	-0.61	0.61
5	237	2288	234	2248	-3	-40	40	-0.05	-0.62	0.62
6	566	1336	556	1319	-9	-17	19	-0.14	-0.27	0.30
7	0	0	0	0	0	0	0	0	0	0

Table 5.7 – Profile K_3 : Coordinates, displacements and velocity of displacements of the survey points of the circular profile K_3 at two different time periods (04.12.2019 and 06.02.2020)

5.3.2 Vertical deformation

The initial vertical distance between the survey point 4 and the bottom of the ice gallery is 2500mm (Table 5.8). In 64 days, the diameter shortens of 39mm, 1.6% of its initial length. The mean strain rate is $-1.6\%/64 \text{ days} = -0.02\%/day = -9.1\%/year$.

i	T	ΔT	D_4	ΔD_4	$\Delta D_{4,cum}$	δD_4	$\delta \dot{D}_4$
[–]	[–]	[days]	[mm]	[mm]	[mm]	[%]	[%/day]
1	04.12.19	0	2500	0	0	0	0
2	06.02.20	64	2461	-39	-39	-1.6	-0.02

Table 5.8 – Profile K_3 : Measured vertical deformation from 04.12.19 to 06.02.20

5.3.3 Horizontal deformation

The initial horizontal distance between the survey points 2 and 6 is 2694mm (Table 5.9). In 64 days, the diameter shortens of 22mm, 0.8% of its initial length. The mean strain rate is $-0.8\%/64\text{days} = -0.01\%/day = -4.6\%/year$.

i	T	ΔT	D_{26}	ΔD_{26}	$\Delta D_{26,cum}$	δD_{26}	$\delta \dot{D}_{26}$
[–]	[–]	[days]	[mm]	[mm]	[mm]	[%]	[%/day]
1	04.12.19	0	2696	0	0	0	0
2	06.02.20	64	2674	-22	-22	-0.8	-0.01

Table 5.9 – Profile K_3 : Measured horizontal deformation from 04.12.19 to 06.02.20

5.3.4 Oblique deformation

The initial horizontal distance between the survey points 1 and 5 is 2624 (Table 5.10). In 64 days, the diameter shortens of 39mm, 1.5% of its initial length. The mean strain rate is $-1.5\%/64\text{days} = -0.02\%/day = -8.6\%/year$.

The initial oblique distance between the survey points 3 and 6 is 2464mm (Table 5.11). In 64 days, the diameter shortens of 16mm, 0.6% of its initial length. The mean strain rate is $-0.6\%/days = -0.01\%/day = -3.7\%/year$.

The initial oblique distance between the survey points 3 and 7 is 2888mm (Table 5.12). In 64 days, the diameter shortens of 30mm, 1.0% of its initial length. The mean strain rate is $-1.0\%/days = -0.02\%/day = -5.9\%/year$.

i	T	ΔT	D_{15}	ΔD_{15}	$\Delta D_{15,cum}$	δD_{15}	$\delta \dot{D}_{15}$
[-]	[-]	[days]	[mm]	[mm]	[mm]	[%]	[%/day]
1	04.12.19	0	2624	0	0	0	0
2	06.02.20	64	2585	-39	-39	-1.5	-0.02

Table 5.10 – Profile K_3 : Measured oblique deformation from 04.12.19 to 06.02.20

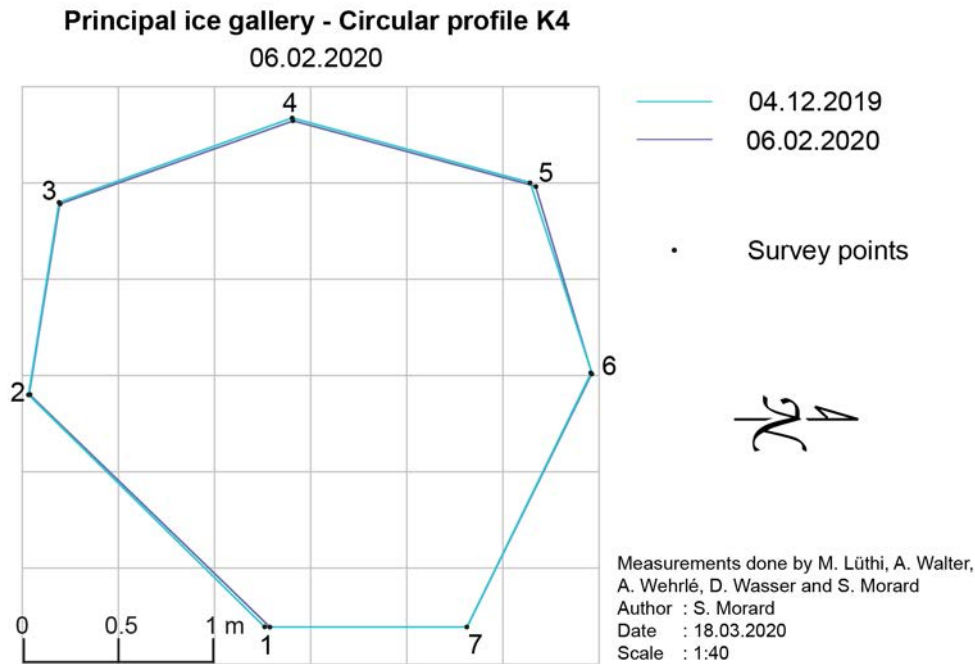
i	T	ΔT	D_{36}	ΔD_{36}	$\Delta D_{36,cum}$	δD_{36}	$\delta \dot{D}_{36}$
[-]	[-]	[days]	[mm]	[mm]	[mm]	[%]	[%/day]
1	04.12.19	0	2464	0	0	0	0
2	06.02.20	64	2448	-16	-16	-0.65	-0.01

Table 5.11 – Profile K_3 : Measured oblique deformation from 04.12.19 to 06.02.20

i	T	ΔT	D_{37}	ΔD_{37}	$\Delta D_{37,cum}$	δD_{37}	$\delta \dot{D}_{37}$
[-]	[-]	[days]	[mm]	[mm]	[mm]	[%]	[%/day]
1	04.12.19	0	2888	0	0	0	0
2	06.02.20	64	2858	-30	-30	-1.05	-0.02

Table 5.12 – Profile K_3 : Measured oblique deformation from 04.12.19 to 06.02.20

5.4 Profile K_4

Figure 5.4 – Circular profile K_4 at two different time periods (04.12.2019 and 06.02.2020)

The data for the profile K_4 (Fig. 5.4) comes from the measurements done at the Jungfrau-joch on 04.12.2019 and 06/07.02.2020. The table 5.13 presents the coordinates of each survey point and the displacements of these coordinates. The coordinates were calculated using a script Python (see Chapter 4.1.2). The magnitude of the displacement in the x-direction is of few millimeters and few centimeters for some points and in the y-direction it is similar. The table 5.14 presents the vertical deformation between the survey point 4 and the bottom of the ice gallery, the table 5.15 the horizontal deformation between the survey points 2 and 6, the table 5.16 the oblique de-

formation between the survey points 1 and 5, the table 5.17 the oblique deformation between the survey points 3 and 6, and the table 5.18 the oblique deformation between the survey points 3 and 7.

The ice cover above the circular profile K_4 is 20 meters. The stress σ of the ice cover on the circular profile is $176'580 \text{ kg/m}^2$. The deformation of the circular profile was measured for 64 days. The horizontal specific strain rate ϵ_y is $0.001\%/day$. The viscosity μ is $7.63 \cdot 10^{14} \text{ Pa} \cdot \text{s}$.

5.4.1 Positions and displacements of the survey points

i	X_1	Y_1	X_2	Y_2	dx	dy	D	v_x	v_y	v
[–]	[–]	[mm]	[mm]	[mm]	[mm]	[mm]	[mm]	[mm/day]	[mm/day]	[mm/day]
1	-1069	0	-1042	0	267	0	267	4.17	0	4.17
2	-2318	1225	-2314	1229	4	4	6	0.06	0.06	0.08
3	-2156	2241	-2153	2232	3	-9	9	0.05	-0.14	0.15
4	-924	2686	-919	2671	5	-15	16	0.08	-0.23	0.24
5	334	2345	362	2326	28	-19	34	-0.30	0.53	0.61
6	658	1345	660	1338	2	-7	7	-0.11	0.11	0.16
7	0	0	0	0	0	0	0	0	0	0

Table 5.13 – Profile K_4 : Coordinates, displacements and velocity of displacements of the survey points of the circular profile K_4 at two different time periods (04.12.2019 and 06.02.2020)

5.4.2 Vertical deformation

The initial vertical distance between the survey point 4 and the bottom of the ice gallery is 2686mm (Table 5.14). In 64 days, the diameter shortens of 15mm, 0.6% of its initial length. The mean strain rate is $-0.6\%/64 \text{ days} = -0.01\%/day = -3.4\%/year$.

i	T	ΔT	D_4	ΔD_4	$\Delta D_{4,cum}$	δD_4	$\delta \dot{D}_4$
[–]	[–]	[days]	[mm]	[mm]	[mm]	[%]	[%/day]
1	04.12.19	0	2686	0	0	0	0
2	06.02.20	64	2671	-15	-15	-0.6	-0.009

Table 5.14 – Profile K_4 : Measured vertical deformation from 04.12.19 to 06.02.20

5.4.3 Horizontal deformation

The initial horizontal distance between the survey point 2 and 6 is 2978mm (Table 5.15). In 64 days, the diameter shortens of 2mm, 0.07% of its initial length. The mean strain rate is $-0.07\%/64 \text{ days} = -0.001\%/day = -0.4\%/year$.

i	T	ΔT	D_{26}	ΔD_{26}	$\Delta D_{26,cum}$	δD_{26}	$\delta \dot{D}_{26}$
[–]	[–]	[days]	[mm]	[mm]	[mm]	[%]	[%/day]
1	04.12.19	0	2978	0	0	0	0
2	06.02.20	64	2976	-2	-2	-0.07	-0.001

Table 5.15 – Profile K_4 : Measured horizontal deformation from 04.12.19 to 06.02.20

5.4.4 Oblique deformation

The initial oblique distance between the survey point 1 and 5 is 2733mm (Table 5.16). In 64 days, the diameter shortens of 16mm, 0.6% of its initial length. The mean strain rate is $-0.6\%/64 \text{ days} = -0.009\%/day = -3.3\%/year$.

i	T	ΔT	D_{15}	ΔD_{15}	$\Delta D_{15,cum}$	δD_{15}	$\delta \dot{D}_{15}$
[-]	[-]	[days]	[mm]	[mm]	[mm]	[%]	[%/day]
1	04.12.19	0	2733	0	0	0	0
2	06.02.20	64	2717	-16	-16	-0.6	-0.009

Table 5.16 – Profile K_4 : Measured oblique deformation from 04.12.19 to 06.02.20

The initial oblique distance between the survey points 3 and 6 is 2953mm (Table 5.17). In 64 days, the diameter shortens of 2mm, 0.07% of its initial length. The mean strain rate is $-0.07\%/64 \text{ days} = -0.001\%/day = -0.4\%/year$.

i	T	ΔT	D_{36}	ΔD_{36}	$\Delta D_{36,cum}$	δD_{36}	$\delta \dot{D}_{36}$
[-]	[-]	[days]	[mm]	[mm]	[mm]	[%]	[%/day]
1	04.12.19	0	2953	0	0	0	0
2	06.02.20	64	2951	-2	-2	-0.06	-0.001

Table 5.17 – Profile K_4 : Measured oblique deformation from 04.12.19 to 06.02.20

The initial oblique distance between the survey points 3 and 7 is 3110mm (Table 5.18). In 64 days, the diameter shortens of 9mm, 0.3% of its initial length. The mean strain rate is $-0.3\%/days = -0.005\%/day = -1.7\%/year$.

i	T	ΔT	D_{37}	ΔD_{37}	$\Delta D_{37,cum}$	δD_{37}	$\delta \dot{D}_{37}$
[-]	[-]	[days]	[mm]	[mm]	[mm]	[%]	[%/day]
1	04.12.19	0	3110	0	0	0	0
2	06.02.20	64	3101	-9	-9	-0.3	-0.005

Table 5.18 – Profile K_4 : Measured oblique deformation from 04.12.19 to 06.02.20

5.5 Temperature

5.5.1 Air temperature

The mean annual air temperature was in 1954 approximately $-8^\circ C$ outside (Fig. 3.2). The air temperature in the ice gallery oscillated between $-3^\circ C$ and $-1^\circ C$ in the 1950s (Haefeli & Brentani, 1954a, page 10). The minimal air temperature, measured in the ice gallery during the period 26.10.1954-04.02.1956, is $-8^\circ C$, and the maximal air temperature is $-2^\circ C$ (Fig. 5.5). The mean temperature in the ice gallery is $-4.75^\circ C$. The air temperature in the principal ice gallery was measured two times at different locations. From 26.10.1954 to 04.02.1956, the air temperature was measured at the position hm 1.00. From 04.01.1956 to 02.01.1957, the air temperature was measured at the position hm 100.00. The temperature measurements from both time periods overlap (Fig. 5.5). The mean air temperature from 26.10.1954 to 02.01.1957 is $-4.75^\circ C$. The minimal air temperature is $-9^\circ C$ and the maximal air temperature is $-1^\circ C$ (Haefeli, 1957, page 19) (Fig. 5.5).

5.5.2 Rock-ice contact temperature

In 1958, Schnitter and Kasser (1958, page 13) measured the temperature at the contact surface between the ice and the rock (Fig. 5.6) at the position hm 0.40, where there was already a borehole. After 9 days, the temperature stabilizes at $-2.3^\circ C$ (Fig. 5.6). The ice cap lies on permafrost as Haefeli (1953, 1963), Haefeli and Schnitter (1954) and Haefeli and Brentani (1954a, 1954b, page 403) stated in their reports (see Chapter 3.4).

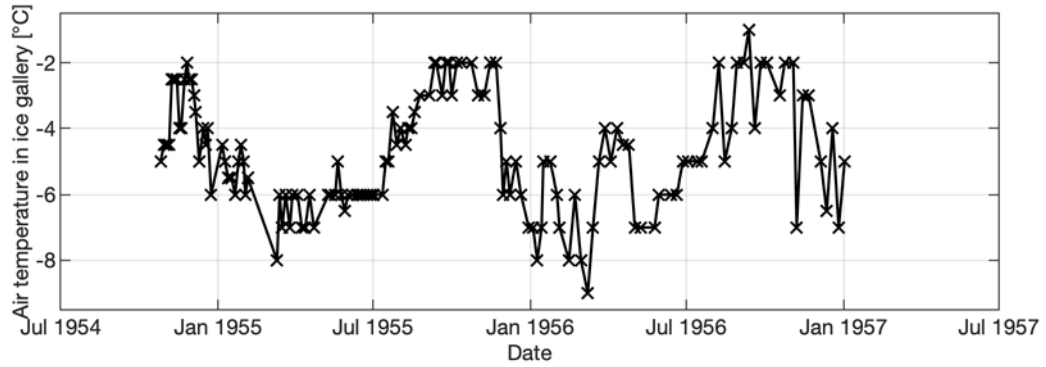


Figure 5.5 – Air temperature in the main ice gallery at the positions hm 1.00 (data taken from Haefeli (1956, page 25)) and hm 100.00 (data taken from Haefeli (1957, page 19))

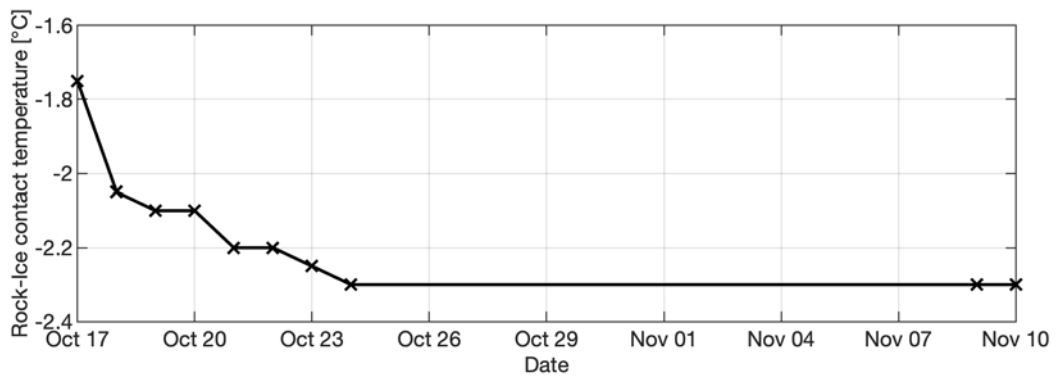


Figure 5.6 – Rock-ice contact temperature in the borehole at position hm 0.4 from 17.10.1958 to 10.11.1958 (data taken from Schnitter and Kasser (1958, page 13))

5.5.3 Ice temperature

The ice temperature of the ice cap was investigated at different locations and different periods (Fig. B.8). Vögtli (1959, page 14) measured the ice temperature in ten different boreholes (Fig. 5.7). The coldest temperatures are measured in the borehole B1 (Fig. 5.7). The borehole B1 situates at 50m east of the transversal ice gallery Q100 (Fig. B.8, B.7). The temperatures vary between -4°C and -3°C from November 1958 to mid-February 1959. The warmest temperatures are measured in the boreholes B9 and B10 (Fig. 5.7). The boreholes B9 and B10 locate in the transversal ice gallery Q100. The borehole B9 situates approximately 5m south from the main ice gallery, and the borehole B10 situates 25m north from the main ice gallery (Fig. B.8, B.7). The temperatures vary between -1.75°C and -1°C from November 1958 to mid-February 1959. The temperatures in the boreholes B2 to B8 behave similarly (Fig. 5.7). The temperatures vary between -3°C and -1.75°C from November 1958 to mid-February 1959. In the borehole B3, the temperature was measured at different depth (0m, 5m, 10m, and 15m) (Fig 5.8) between November 1958 and mid-February 1959. The temperature is warmer at the rock surface than at an ice thickness of 15m. Vögtli (1959, page 18) measured the temperature in the ice gallery walls between the entrance and the end of the ice gallery in 1958. The temperatures reach 0.5°C to -4.5°C (Fig. 5.9). In 2020, some temperature sensors were installed in the ice gallery in 10m of ice thickness. Three sensors measured the temperature in the bottom of the ice gallery and one in the ice wall (Fig. 5.10). The temperatures vary from 0°C to -1.6°C (Fig. 5.10).

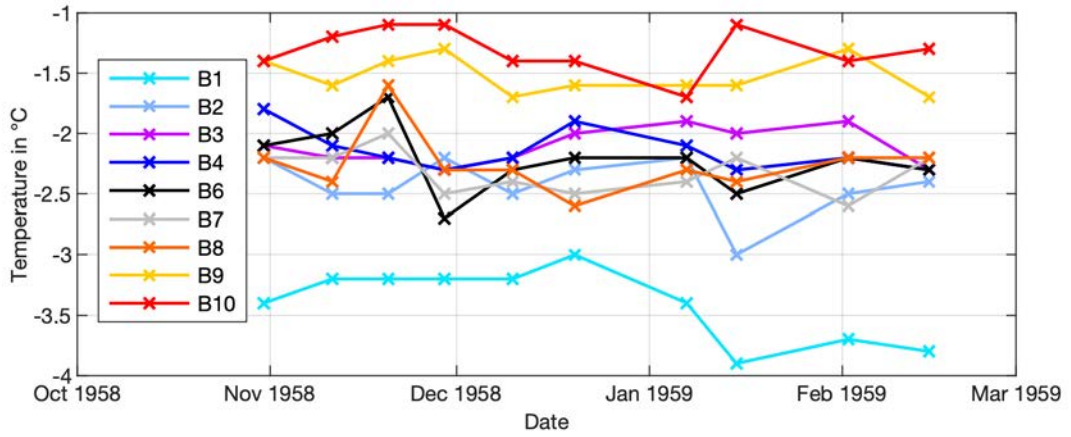


Figure 5.7 – Temperature in the boreholes B1 to B10 from 31.10.1958 to 15.02.1959 in the rock (data taken from Vöggtli (1959, page 14)). The values from borehole B9 are considered by Vöggtli (1959, page 14) as "uncertain".

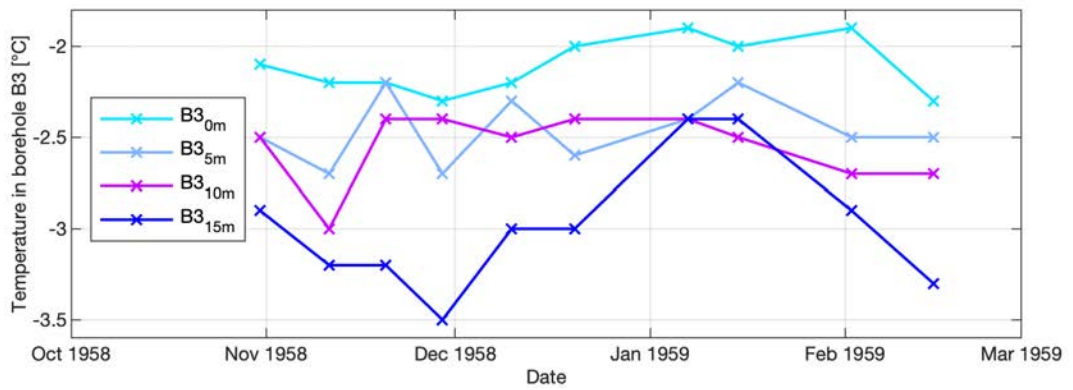


Figure 5.8 – Temperature in the borehole B3 at different depth (0m = rock surface, 5m, 10m, and 15m = ice thickness above the rock) (data taken from Vöggtli (1959, page 14))

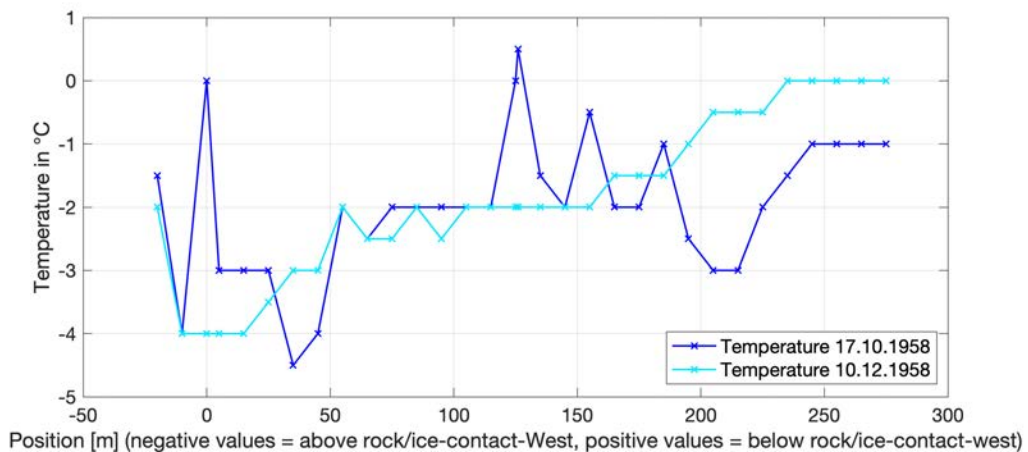


Figure 5.9 – Temperature in the ice walls on 17.10.1958 and 10.12.1958. Point 0m is the borehole B1. Negative values for x-axis are west of the ice gallery. Point -20m is the end of the ice gallery. Point 275m is the entrance of the ice gallery. (Values taken from Vöggtli (1959, page 18))

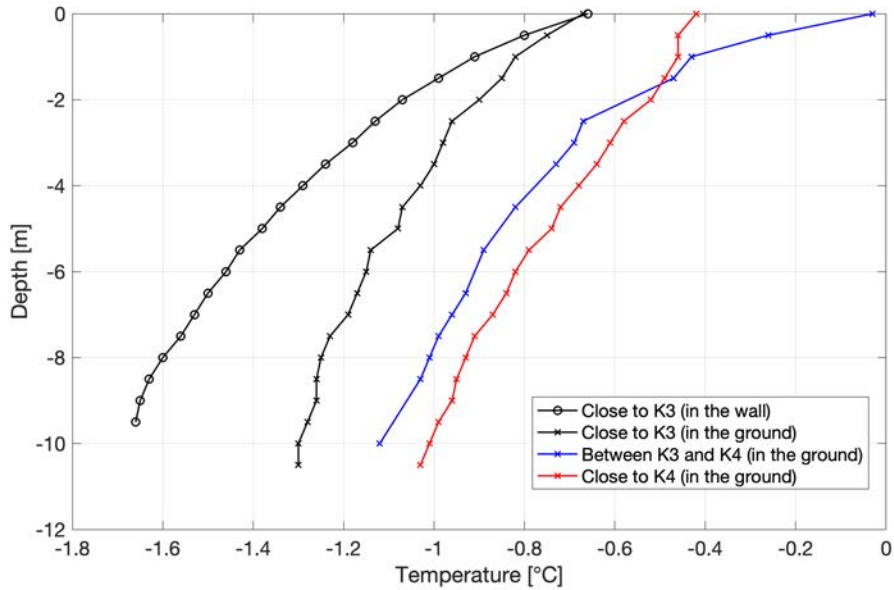


Figure 5.10 – Temperature in the ice walls and ice gallery bottom on 06.02.2020 at different positions

5.6 Ice density

The mean density for ice and firn, estimated by Haefeli and Brentani (1954a, page 404; 1954b, page 12; 1955, page 626), is $850\text{kg}/\text{m}^3$. On 06.02.2020, the density was measured, however the results are not convincing. The measured density for ice was $983.6\text{kg}/\text{m}^3$. For the measurements done in 2020, the ice density is assumed to be $900\text{kg}/\text{m}^3$.

5.7 Ice experiment

In 1956, Haefeli (1963, pages 171-173) did some experiments with some ice samples from the ice cap of the Jungfraujoeh. The ice was taken in the circular profile K_2 , which lied in the transversal gallery Q_{100} (Haefeli, 1963, page 178). He applied an axial stress of $1\text{kg}/\text{cm}^2$ (Fig. 5.11) for 100 days (Haefeli, 1963, page 172). The specific strain rate ϵ_y is $0.0174 \cdot 10^{-8}\text{s}^{-1}$. The specific velocity gradient k_1 is $0.21 \cdot 10^{-8}\text{s}^{-1}$ (Haefeli, 1963, page 178). On Figure 5.12, a relation between the pressure and the specific strain rate is visible.

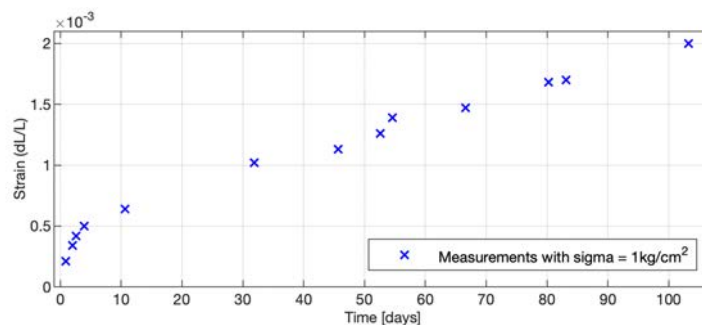


Figure 5.11 – Ice sample with a load of $\sigma = 1\text{kg}/\text{cm}^2$ (data taken and adapted from Haefeli (1963, page 172))

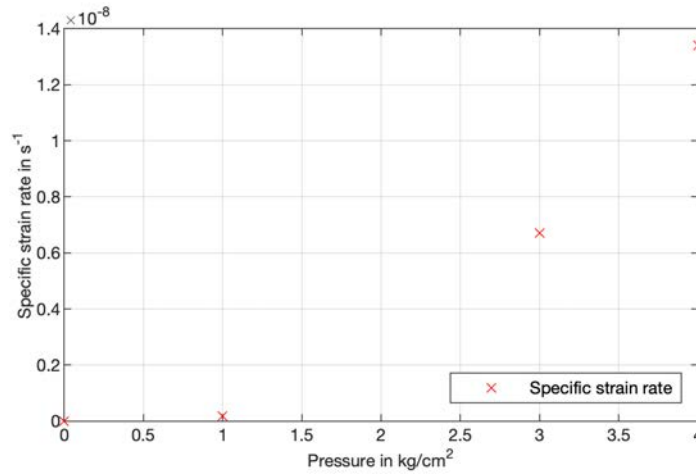


Figure 5.12 – Relation between the pressure and the specific strain rate for different load (1 kg/cm^2 , 3 kg/cm^2 , and 4 kg/cm^2)

5.8 General data on the length of the galleries

This chapter presents some general data and characteristics on the ice galleries at the Jungfrau-joch ice cap. As shown in Fig. 3.7 the axis of the main gallery moves in the northern and southern directions. Moreover, the bottom of the gallery is lowering of maximum 10cm/year. They expect a lowering of 1m in 1960 (Haefeli & Schnitter, 1954, page 6)). Both phenomena imply an elongation of the tunnel. However, this elongation is small. They give the following example. If a part of the main ice gallery, which has a length of 80m, is moving with a lateral buckling of 5m. The elongation of this part of the main ice gallery is 83cm (Haefeli & Schnitter, 1954, page 5; Haefeli, 1956, page 5). A part of the main ice gallery is shortening with a rate of approximately 12cm/year between hm 0.8 and hm 1.2 (Haefeli, 1956, page 5)). They also observe in the transversal ice gallery Q100 an elongation (Haefeli, 1956, page 7). They observe in the main gallery a shortening of the gallery height of 12cm/year. The gallery height passes from 2.50m to 2.15 in 3 years between hm 1.2 and hm 1.4 (Haefeli & Schnitter, 1954, p.age 8; Haefeli & Brentani, 1954a, page 400; Haefeli & Brentani, 1954b, page 6).

5.9 Apparent viscosity

The specific strain rate is determined for the transversal ice gallery Q_{120} (Haefeli & Brentani, 1954a, page 401; 1954b, page 7), for the ice surface (Haefeli & Brentani, 1954a, page 401). For the transversal ice gallery Q_{100} (Haefeli, 1956, page 8), and for the Greenland (Haefeli & Brentani, 1954a, page 405; 1954b, page 15).

The specific strain rate of the transversal ice gallery Q_{120} was determined for the period 19.01.1954-13.05.1954. The gallery has a length of 42.25m and deforms with a rate of 3.7mm/day. The specific strain rate is $\epsilon_y = 0.0087\%/day$ (Haefeli & Brentani, 1954a, page 401; 1954b, page 7). The apparent viscosity μ is $1.16 \cdot 10^{14} Pa \cdot s$. The specific strain rate of the ice surface was determined for the period 26.06.1954-06.09.1954. The specific strain rate is $\epsilon_y = 0.0178\%/day$ (Haefeli & Brentani, 1954a, page 401). The apparent viscosity μ of the transversal ice gallery Q_{100} is $1.5 \cdot 10^{14} Pa \cdot s$ (Haefeli, 1956, page 8). From 13.11.1953 to 22.01.1954, Haefeli (1956, page 4) measured the width in the main ice gallery at 4 different locations (hm 0.6, hm 0.8, hm 1.2, and hm 1.4). From 22.01.1954 to 22.07.1955, he measured the width in the main ice gallery at 2 different locations (hm 0.6 and hm 0.8) (Haefeli, 1956, page 4). From 22.07.1955 to 17.10.1956, Haefeli (1957, page 3) measured the width in the main ice gallery at 5 different locations (hm 0.6, hm 0.8, hm 1.1, hm 1.2, and hm 1.4). He gives the specific strain rate ϵ_y . It is possible to derive the apparent viscosity μ at these different locations (table 5.19). The ice thickness above the gallery at these positions is determined by means of the georeferenced plan (Fig. 3.5). In comparison, the measured apparent viscosity in the Z'mutt ice gallery, which is grabbed in tempered ice, is $2.5 \cdot 10^{13} Pa \cdot s$ for $\sigma_1 = 390'000 kg/m^2$ and $7.2 \cdot 10^{13} Pa \cdot s$ for $\sigma_1 = 220'000 kg/m^2$ (Haefeli & Brentani, 1954b, page 12).

For the Greenland, they determined the apparent viscosity μ for different ice depth. Under an ice thickness of 2'000m, the apparent viscosity μ is $3.5 \cdot 10^{13} Pa \cdot s$. Under 2'500m of ice, the apparent viscosity μ is $6 \cdot 10^{13} Pa \cdot s$. Under 3'000m of ice, the apparent viscosity μ is $1.5 \cdot 10^{14} Pa \cdot s$ (Haefeli & Brentani, 1954a, page 408; 1954b, page 15; Bauer, 1952).

From 13.11.1953 to 22.01.1954 (70 days)				
Position	h	σ_1	ϵ_y	μ
[–]	[m]	$\frac{kg}{m^2}$	s^{-1}	$Pa \cdot s$
hm 0.6	25	208'462	$1.0291 \cdot 10^{-9}$	$1.01 \cdot 10^{14}$
hm 0.8.	25	208'462	$5.2172 \cdot 10^{-9}$	$0.20 \cdot 10^{14}$
hm 1.2	27.5	229'308	$1.3829 \cdot 10^{-9}$	$0.83 \cdot 10^{14}$
hm 1.4	30	250'155	$2.1546 \cdot 10^{-9}$	$0.58 \cdot 10^{14}$
From 22.01.1954 to 22.07.1955 (546 days)				
Position	h	σ_1	ϵ_y	μ
[–]	[m]	$\frac{kg}{m^2}$	s^{-1}	$Pa \cdot s$
hm 0.6	25	208'462	$1.4424 \cdot 10^{-9}$	$0.72 \cdot 10^{14}$
hm 0.8	25	208'462	$9.0722 \cdot 10^{-10}$	$1.15 \cdot 10^{14}$
From 22.07.1955 to 17.10.1956 (453 days)				
Position	h	σ_1	ϵ_y	μ
[–]	[m]	$\frac{kg}{m^2}$	s^{-1}	$Pa \cdot s$
hm 0.6	25	208'462	$1.1098 \cdot 10^{-9}$	$0.94 \cdot 10^{14}$
hm 0.8	25	208'462	$2.5368 \cdot 10^{-10}$	$4.11 \cdot 10^{14}$
hm 1.1	26	216'801	$6.3420 \cdot 10^{-9}$	$0.17 \cdot 10^{14}$
hm 1.2	27.5	229'308	$6.3420 \cdot 10^{-10}$	$1.81 \cdot 10^{14}$
hm 1.4	30	250'155	$4.7565 \cdot 10^{-10}$	$2.63 \cdot 10^{14}$

Table 5.19 – Apparent viscosity in the main gallery determined from the change in the width of the gallery from 13.11.1953 to 22.01.1954, from 22.01.1954 to 22.07.1955, and from 22.07.1955 to 17.10.1956

Chapter 6

Results

6.1 Measurements

Figure 6.1 represents the different measurements realised during 1950-2020. The circular profile K_1 deforms vertically the most rapidly and the circular profile K_4 the slowest. However, the circular profile K_3 deforms horizontally the most rapidly and the circular profile K_4 the slowest. According to Table 6.1, the circular profiles K_1 and K_4 deform almost with the same ratio horizontal/vertical. However, the circular profile K_1 deforms approximately three time faster than the circular profile K_4 . According to Table 6.1, the circular profiles K_2 and K_3 deform almost with the same ratio horizontal/vertical. However, the circular profile K_3 deforms approximately 1.4 times faster than the circular profile K_2 .

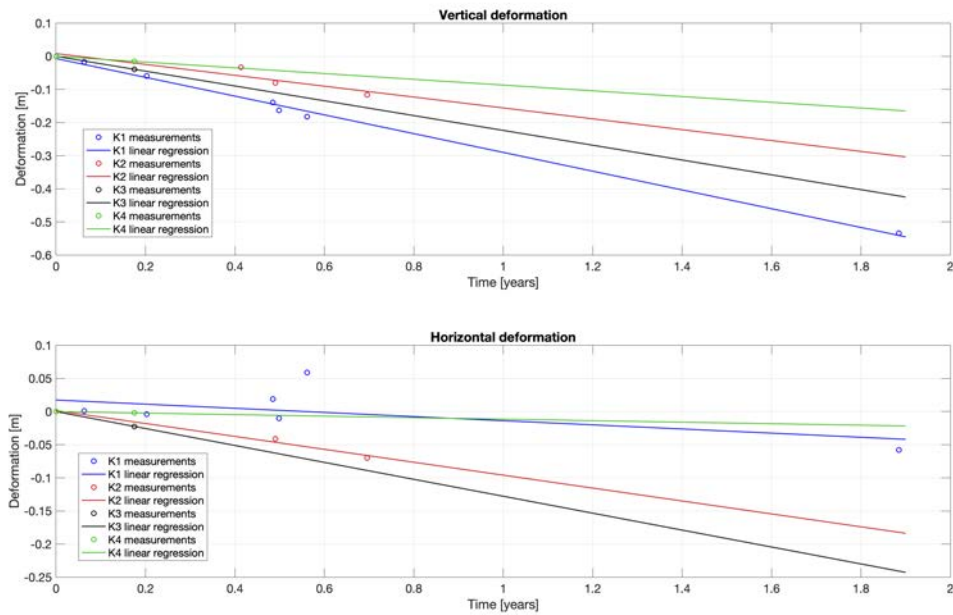


Figure 6.1 – Measurements for the four circular profiles (K_1 , K_2 , K_3 , and K_4)

	Profile K_1	Profile K_2	Profile K_3	Profile K_4
Vertical deformation	-28.3 cm/year	-16.4 cm/year	-22.4 cm/year	-8.7 cm/year
Horizontal deformation	-3.1 cm/year	-9.7 cm/year	-12.8 cm/year	-1.1 cm/year
Ratio hor/vert	0.11	0.59	0.57	0.12

Table 6.1 – Comparison between the different measurements of each circular profile (K_1 , K_2 , K_3 , and K_4)

The analytical solutions for B and A factors (see chapters 2.3 and 2.5) were determined with the

equations (2.5.3) and (2.3.10). The B and A factors were calculated for the horizontal deformations (table 6.2). To have an idea of the values for the B and A factors, Hooke (2005, page 323) finds a B factor of $0.18a^{1/3.11}MPa$ for temperate ice. It gives a A factor of $207a^{-1}MPa^{-3.11}$, i.e. according to Paterson (1999) an ice temperature of approximately $0^\circ C$.

	Unit	Profile K_1	Profile K_2	Profile K_3	Profile K_4
B_{hor}	$[a^{1/3}MPa]$	0.36	0.24	0.16	0.30
A_{hor}	$[a^{-1}MPa^{-3}]$	22.3	68.6	225.6	38.3
T_P	$^\circ C$	$[-10; -5]$	$[-5; 0]$	> 0	$[-10; -5]$
T_{CP}	$^\circ C$	$[-10; -5]$	$[-2; -5]$	> 0	$[-5; -2]$

Table 6.2 – B and A factors for the different circular profiles. T_p are temperature values taken from Paterson (1999) and T_{CP} are temperature values taken from Cuffey and Paterson (2010).

The four profiles get different values for B and A factors. The circular profile K_3 obtains a value close to the value obtained by Hooke (2005). The other profiles obtain values smaller than Hooke (2005). According to Paterson (1999), the profile K_2 may have a temperature contained between $-5^\circ C$ and $0^\circ C$. The profile K_3 is warmer than $0^\circ C$. The profiles K_1 and K_4 may have a temperature between $-10^\circ C$ and $-5^\circ C$. According to Cuffey and Paterson (2010), the profile K_1 may have a temperature contained between $-10^\circ C$ and $-5^\circ C$. The profile K_2 may have a temperature contained between $-2^\circ C$ and $0^\circ C$. The profile K_3 may have a temperature warmer than $0^\circ C$ and the profile K_4 may have a temperature contained between $-5^\circ C$ and $-2^\circ C$.

6.2 Influence of the parameters

6.2.1 Changing the width of the mesh

In this section, the results of the modellings according to different mesh widths for the four circular profiles are presented. The aim is to observe the influence of the mesh in the modelling.

Circular profile K_1

For the circular profile K_1 , meshes with a width of 60m, 100m, and 120m were applied to the modellings (Fig. 6.2). The three modellings follow almost a linear behavior. The modelling with a mesh of 30m gives different results with comparison to meshes 100m or 120m. The modellings with a mesh of 100m or 120m have similar results. At the timestep $t=0.9285$ years, the difference between the modelling with a mesh of 100m and 120m is approximately 0.2mm for the vertical deformation and 0.6mm for the horizontal deformation. At the timestep $t=0.2$ years, the difference between the modellings 60m and 100m is 5.1mm for the vertical deformation and 4.2mm for the horizontal deformation. For the next modellings, the mesh with a width of 100m will be used.

Circular profile K_2

For the circular profile K_2 , meshes with a width of 60m, 100m, and 120m were applied to the modellings (Fig. 6.3). The three modellings follow almost a linear behavior. The modelling with a mesh of 30m gives different results in comparison with a mesh of 100m or 120m. The modellings with a mesh of 100m and 120m give similar results. At the timestep $t=1.117$ years, the difference between the modellings 100m and 120m is approximately 2mm for the vertical deformation and 3mm for the horizontal deformation. At the timestep $t=0.1$ years, the difference between the modellings is 1mm for the vertical deformation and 0.6mm for the horizontal deformation. For the next modellings, the mesh with a width of 100m will be used.

Circular profile K_3

For the circular profile K_3 , meshes with a width of 10m, 20m, 60m, and 100m were applied to the modellings (Fig. 6.4). The four modellings follow almost a linear behavior. The modelling with a mesh of 10m and 20m give different results in comparison with a mesh of 60m or 100m. After 0.2 years, the difference between the modellings 60m and 100m is 0.05mm for the vertical deformation, and 0.5mm for the horizontal deformation. The differences for the vertical and horizontal deformation between the mesh of 10m and 100m are large. The difference is 2.5 cm for

the vertical deformation and 3.3 cm for the horizontal deformation. For the next modellings, the mesh with a width of 60m will be used.

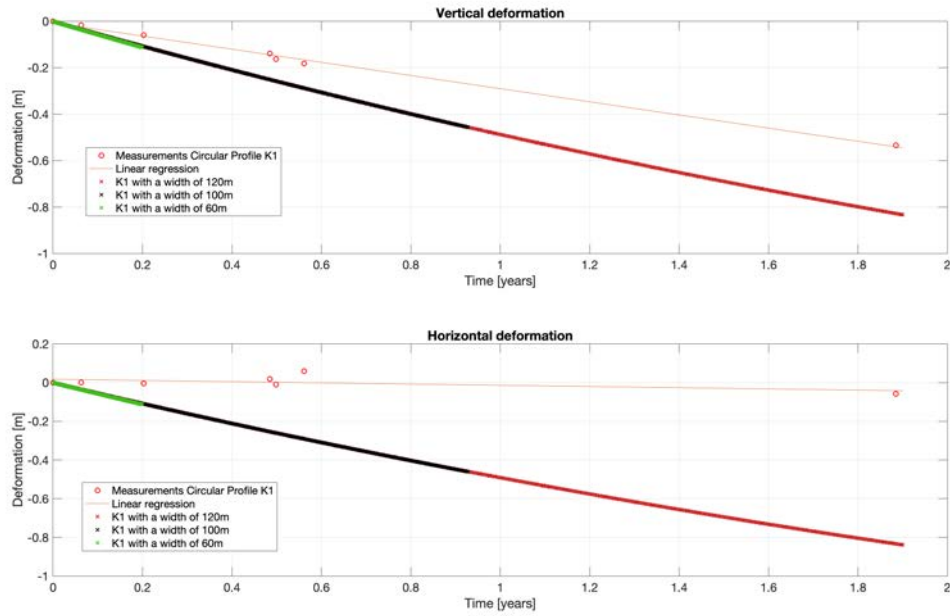


Figure 6.2 – Different modellings for the circular profile K_1 with different mesh widths (60m, 100m, and 120m)

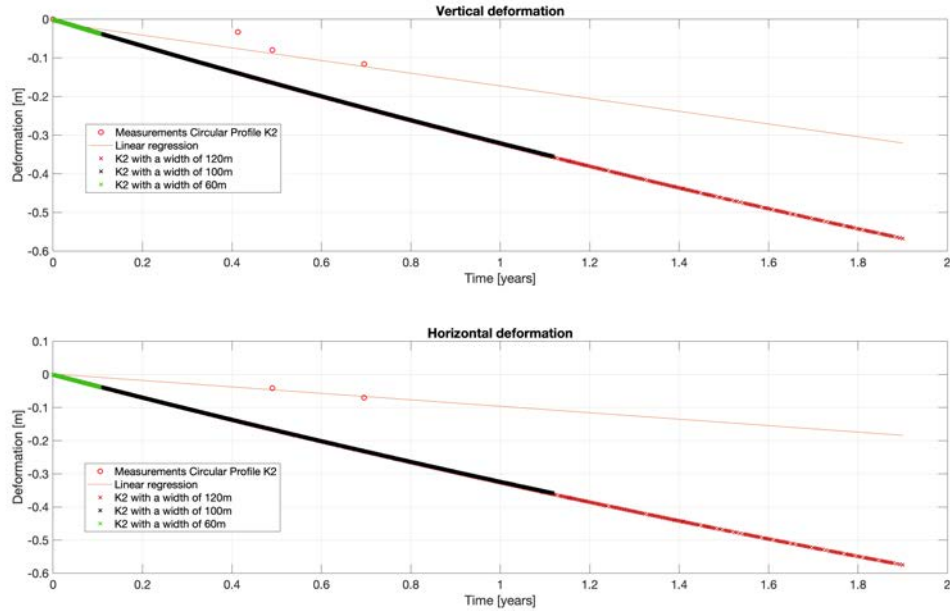


Figure 6.3 – Different modellings for the circular profile K_2 with different mesh widths (60m, 100m, and 120m)

Circular profile K_4

For the circular profile K_4 , meshes with a width of 10m, 20m, 60m, and 100m were applied to the modellings (Fig. 6.5). The four modellings follow almost a linear behavior. The modelling with a mesh of 10m and 20m give different results in comparison with a mesh of 60m or 100m.

After 0.2 years, the difference between the modellings 60m and 100m is 0mm. The differences for the vertical deformation and horizontal deformation between the mesh of 10m and 100m are large. The difference is 6.6 cm for the vertical deformation and 8.5 cm for the horizontal deformation after 0.2 years . For the next modellings, the mesh with a width of 60m will be used.

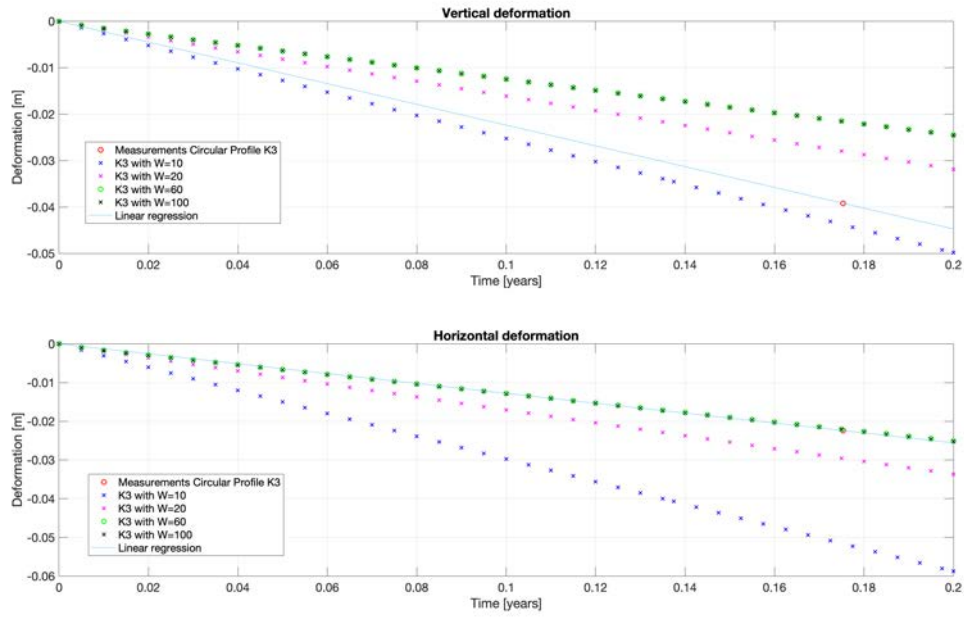


Figure 6.4 – Different modellings for the circular profile K_3 with different mesh widths (10m, 20m, 60m, and 100m)

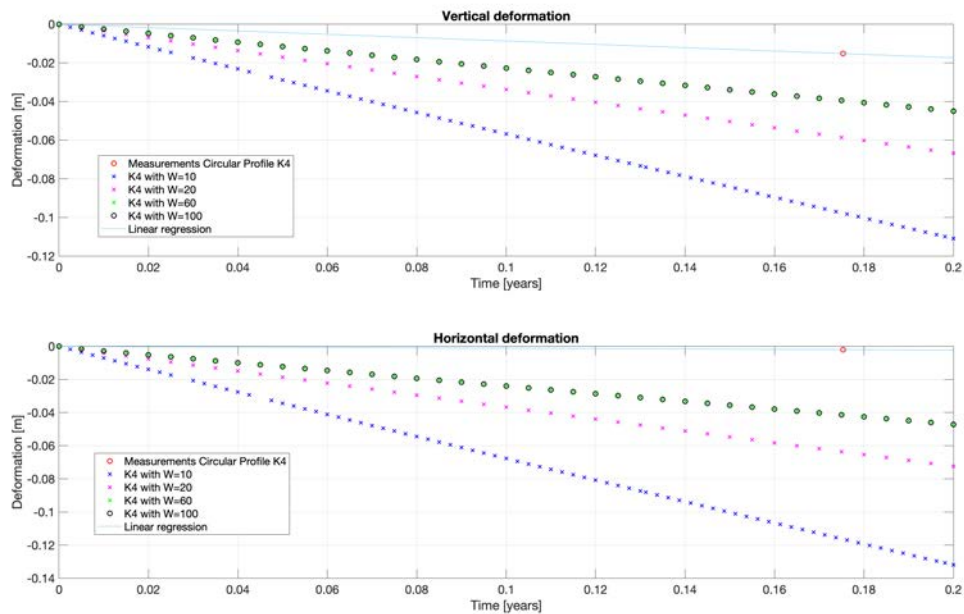


Figure 6.5 – Different modellings for the circular profile K_4 with different mesh widths (10m, 20m, 60m, and 100m)

6.2.2 Changing Young's modulus

In this section, the results of the modelling according to different Young's modulus for the four circular profiles are presented. The aim is to determine the unit of Young's modulus in MOOSE and to observe the influence of Young's modulus in the modelling.

Circular profile K_1

For the circular profile K_1 , the modelling behaves almost similar for an Young's modulus of 8700 or 870 (Fig. 6.6). However, a difference is graphically visible. After 0.9237 years, the difference is 5.5mm for the vertical deformation and 6.9mm for the horizontal deformation. For an Young's modulus of 8.7, the modelling has not a linear behavior. At the timestep $t=0.555$ years, the difference between the modelling of 8700 and 8.7 is approximately 41cm for the vertical deformation and 24.5cm for the horizontal deformation.

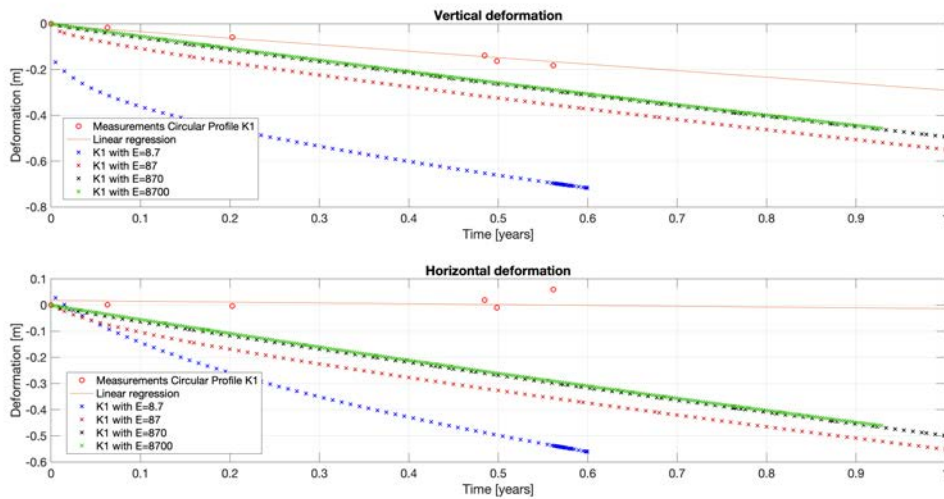


Figure 6.6 – Different modellings for the circular profile K_1 with different Young's modulus (8.7, 87, 870, and 8700)

Circular profile K_2

For the circular profile K_2 , the modelling behaves almost similar for an Young's modulus of 8700 or 870 (Fig. 6.7). However, a difference is graphically visible. After 0.28 years, the difference is 4.65mm for the vertical deformation and 5.56mm for the horizontal deformation. For an Young's modulus of 8.7, the modelling has not a linear behavior. At the timestep $t=0.16$ years, the difference between the modelling 8700 and 8.7 is approximately 22cm for the vertical deformation and 11cm for the horizontal deformation.

Circular profile K_3

For the circular profile K_3 , there is a difference between the Young's modulus of 8700 and 870 (Fig. 6.8). After 0.2 years, the difference is 0.3mm for the vertical and horizontal deformation. For an Young's modulus of 8.7, the modelling has not a linear behavior. After 0.2 years, the difference between the modelling 8700 and 8.7 is 16cm for the vertical deformation and 4cm for the horizontal deformation.

Circular profile K_4

For the circular profile K_4 , the modelling behaves similar for an Young's modulus of 8700 or 870 (Fig. 6.9). After 0.2 years, the difference between the modelling of 8700 and 870 is 0mm. For an Young's modulus of 8.7, the modelling has not a linear behavior. The modelling points follow a curved pattern. The difference between the modellings of 8700 and 8.7 is 20.26cm for the vertical deformation and 8cm for the horizontal deformation after 0.2 years.

According the four circular profiles (Fig. 6.6 - 6.9), the chosen Young's modulus will be 8700 for the next modellings, i.e. 8700 MPa, because the Young's modulus of ice is 8.7 GPa.

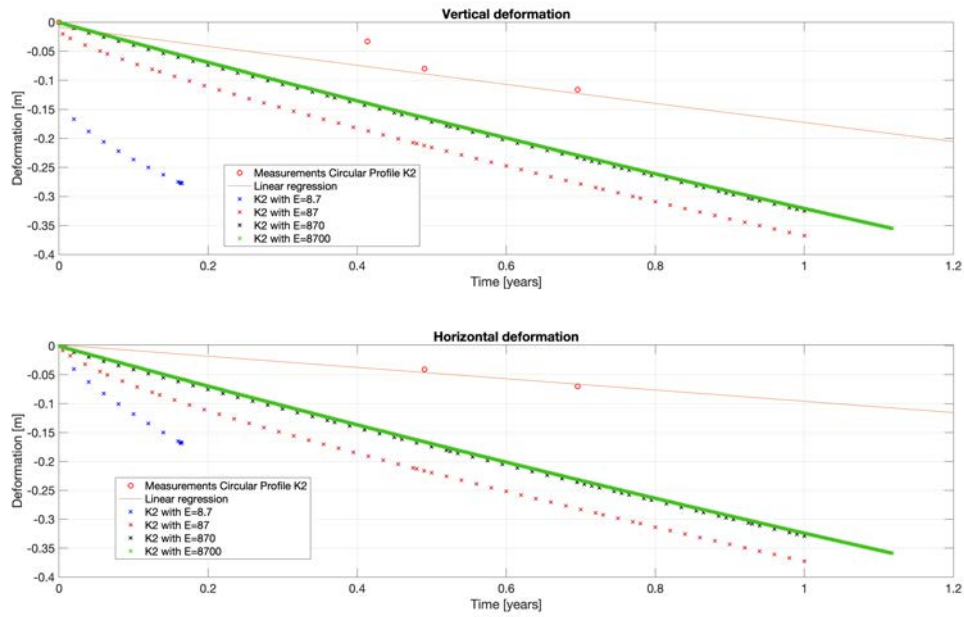


Figure 6.7 – Different modellings for the circular profile K_2 with different Young's modulus (8.7, 87, 870, and 8700)

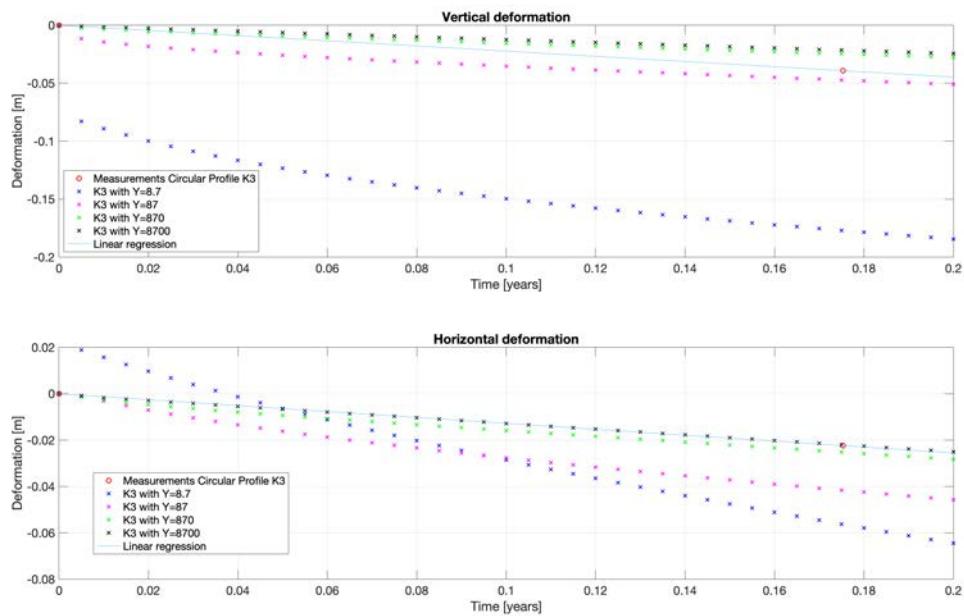


Figure 6.8 – Different modellings for the circular profile K_3 with different Young's modulus (8.7, 87, 870, and 8700)

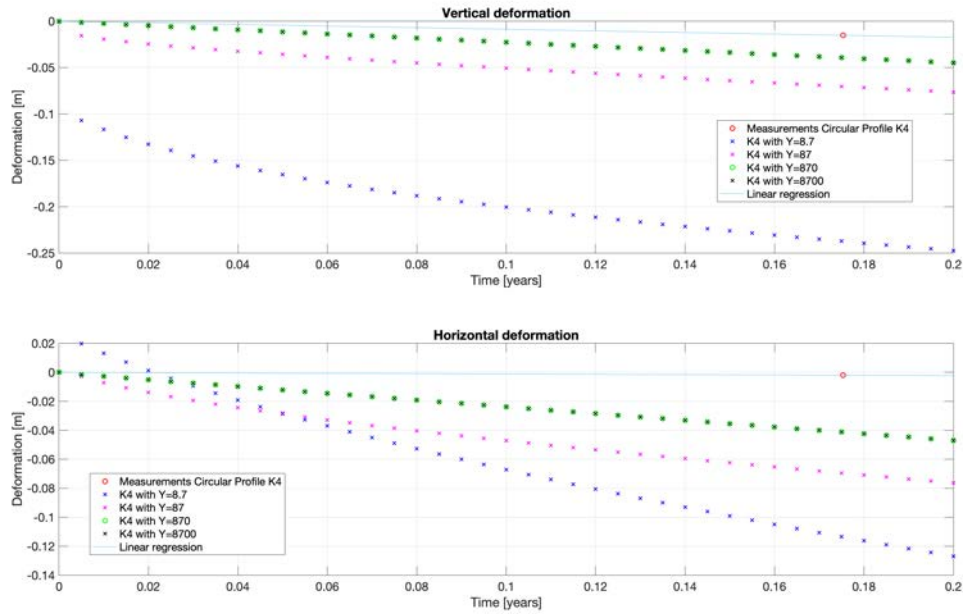


Figure 6.9 – Different modellings for the circular profile K_4 with different Young's modulus (8.7, 87, 870, and 8700)

6.2.3 Changing n coefficient

In this section, the results of the modelling according to different n coefficients for the four circular profiles are presented. The aim is to observe the influence of the n coefficient in the modelling. For the circular profiles K_1 (Fig. 6.10), K_2 (Fig. 6.11), K_3 (Fig. 6.12), and K_4 (Fig. 6.13), the n coefficient influences a lot the slope of the results. The results with $n=4$ give a slope approaching 0. The results with $n=3$ represent at best the measurements. However, the horizontal deformation of K_4 are better described with $n=4$.

6.2.4 Changing m coefficient

In this section, the results of the modelling according to different m coefficients for the four circular profiles are presented. The aim is to observe the influence of the m coefficient in the modelling. For the circular profiles K_1 (Fig. 6.14), K_2 (Fig. 6.15), K_3 (Fig. 6.16), and K_4 (Fig. 6.17), the m coefficient influences a lot the results. For a m coefficient of 1,2, or 3, the modelling points will follow a curved pattern. For $m = 0$, the modelling points follow a linear behavior.

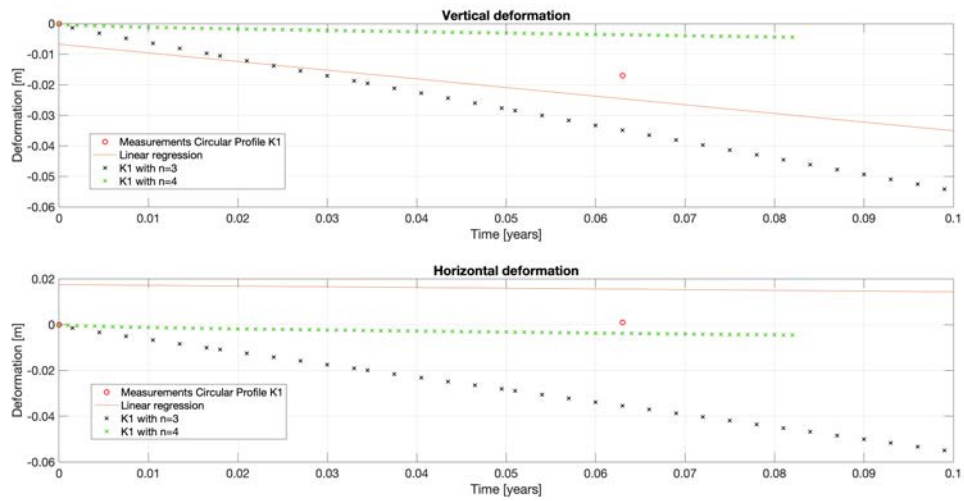


Figure 6.10 – Different modellings for the circular profile K_1 with different n coefficients (3 and 4)

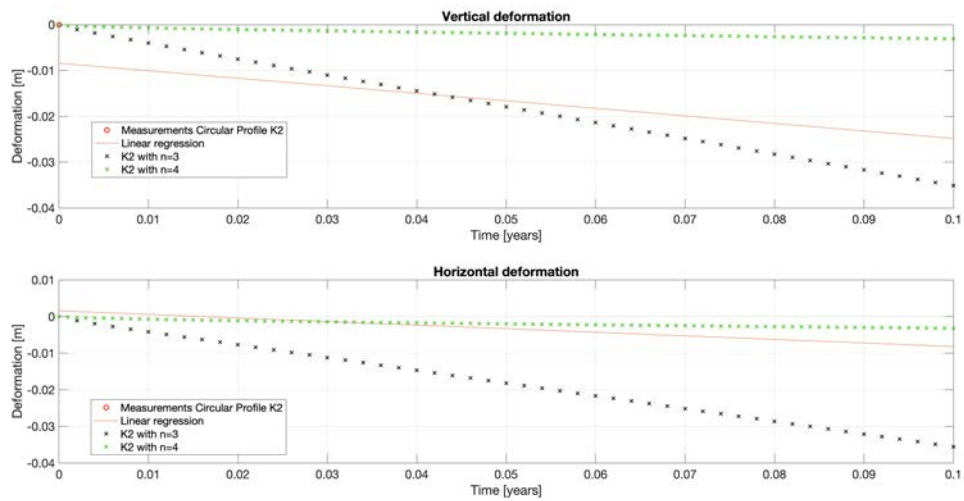


Figure 6.11 – Different modellings for the circular profile K_2 with different n coefficients (3 and 4)

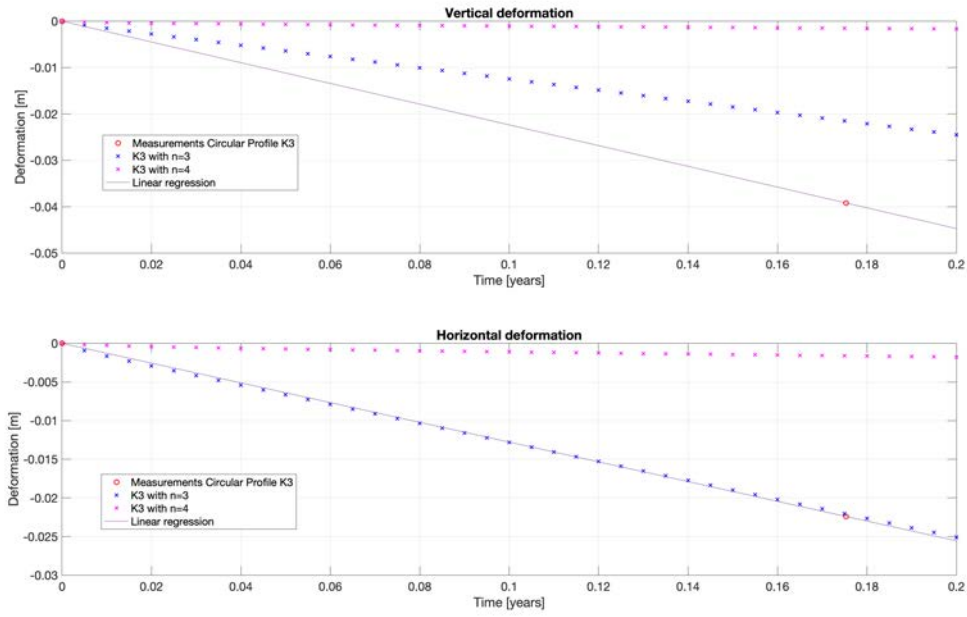


Figure 6.12 – Different modellings for the circular profile K_3 with different n coefficients (3 and 4)

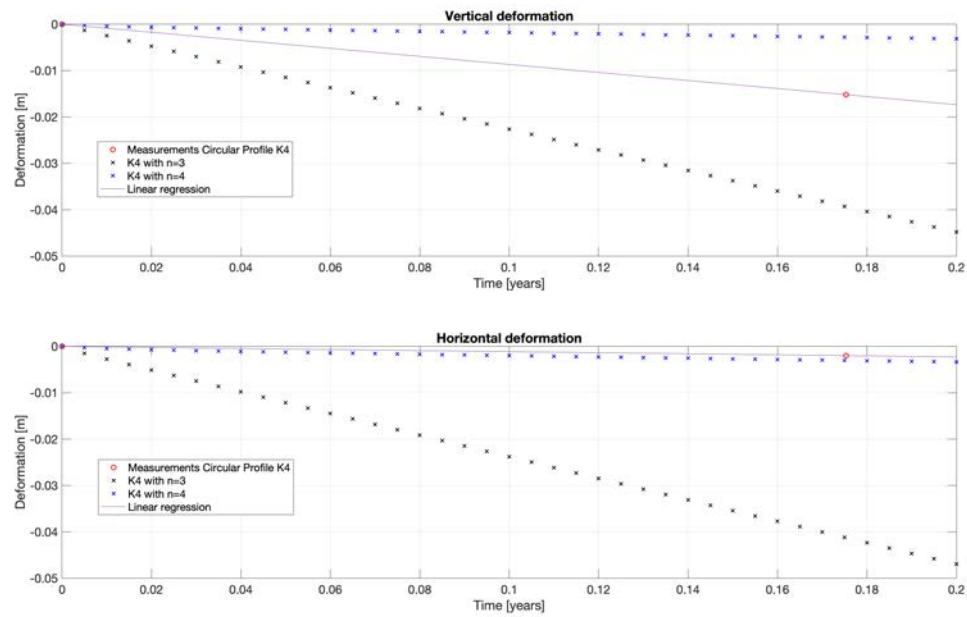


Figure 6.13 – Different modellings for the circular profile K_4 with different n coefficients (3 and 4)

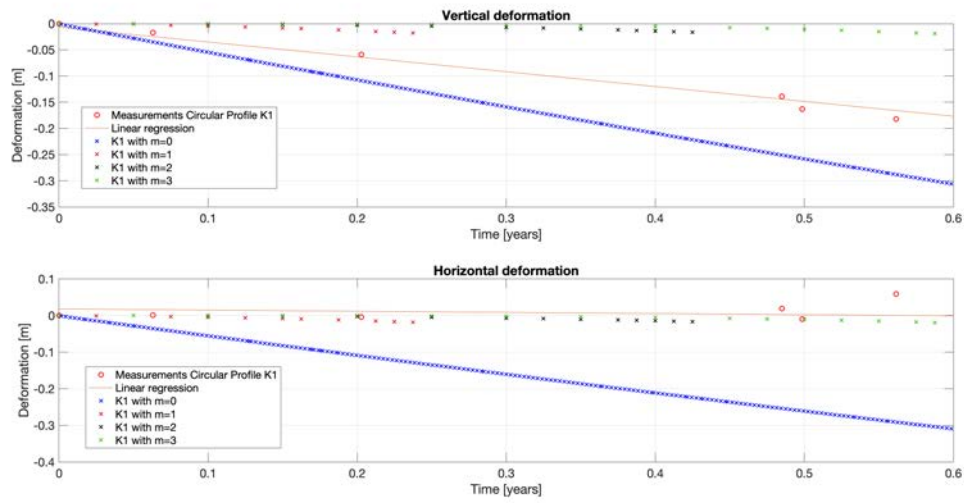


Figure 6.14 – Different modellings for the circular profile K_1 with different m coefficients (0, 1, 2, and 3)

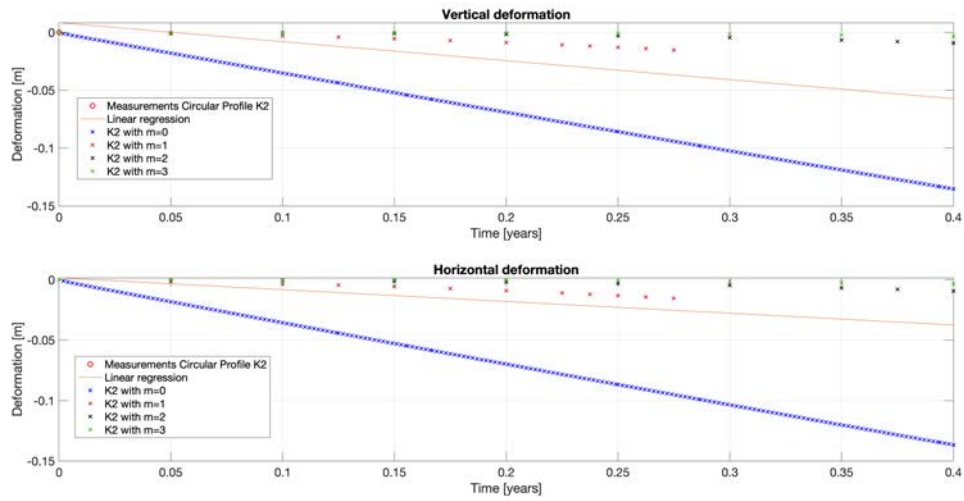


Figure 6.15 – Different modellings for the circular profile K_2 with different m coefficients (0, 1, 2, and 3)

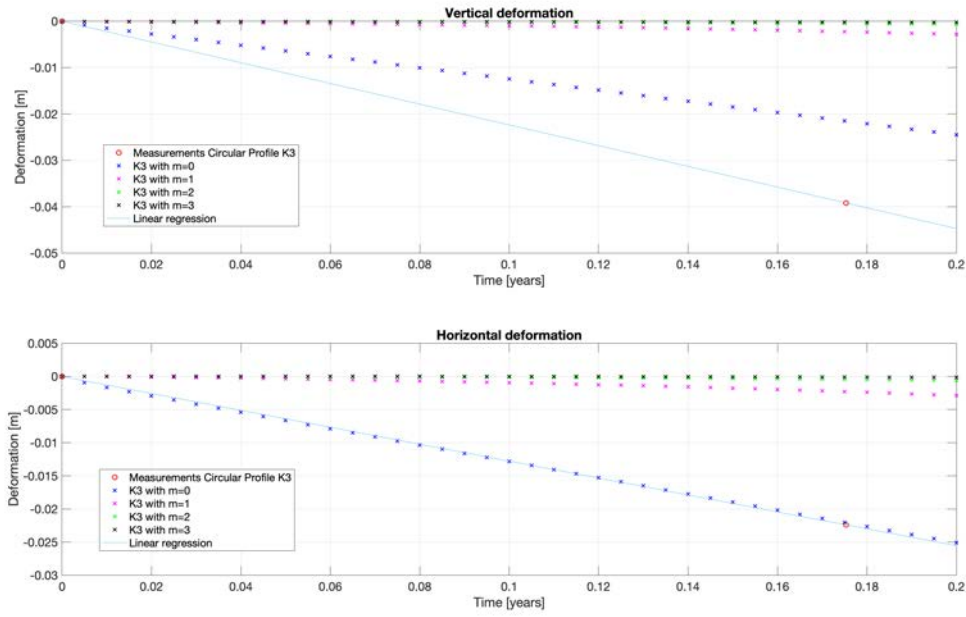


Figure 6.16 – Different modellings for the circular profile K_3 with different m coefficients (0, 1, 2, and 3)

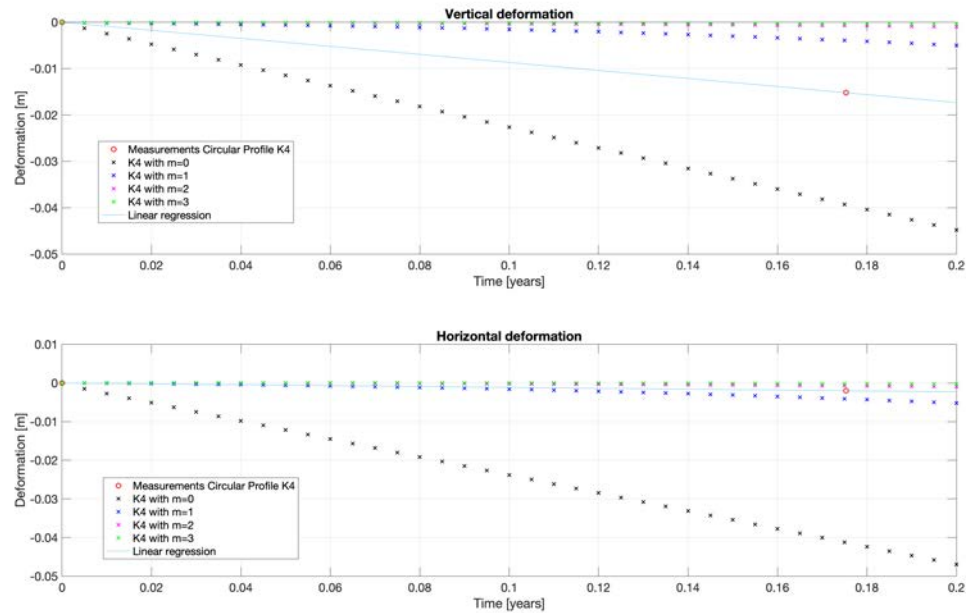


Figure 6.17 – Different modellings for the circular profile K_4 with different m coefficients (0, 1, 2, and 3)

6.2.5 Changing A factor

In this section, the results of the modelling according to different A factors for the four circular profiles are presented. The aim is to observe the influence of the A factor in the modelling. An A factor of $75.7a^{-1}MPa^{-3}$ corresponds to a temperature T of $0^{\circ}C$. An A factor of $53.6a^{-1}MPa^{-3}$ corresponds to a temperature T of $-2^{\circ}C$. An A factor of $30a^{-1}MPa^{-3}$ corresponds approximately to a temperature T of $-5^{\circ}C$. An A factor of $10a^{-1}MPa^{-3}$ corresponds approximately to a temperature T of $-10^{\circ}C$ (Cuffey & Paterson, 2010). The A factor modifies the slope of the results. If the A factor is big, the deformation becomes also large. If the A factor is small, the

deformation is small. A small A factor means a cold temperature.

Circular profile K_1

The vertical deformation is better described with A a little bit bigger than 30 and the horizontal deformation with A smaller than 10 (Fig. 6.18).

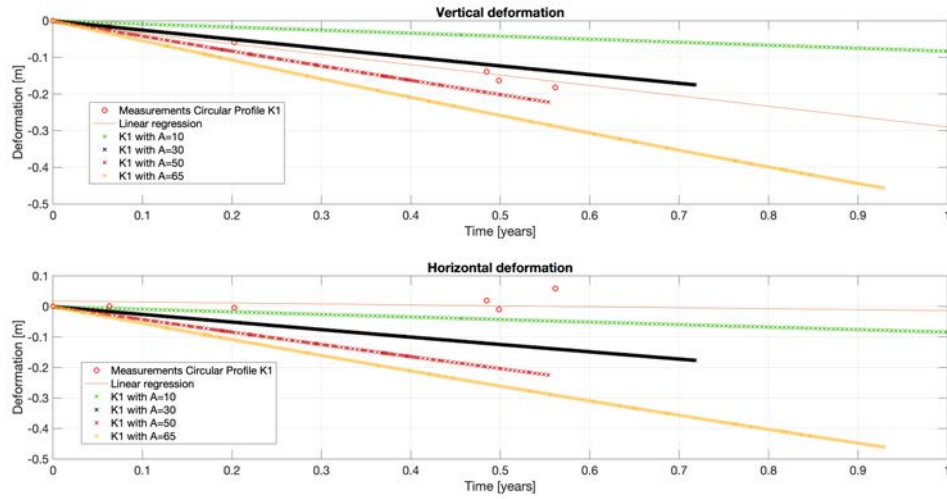


Figure 6.18 – Different modellings for the circular profile K_1 with different A factors (10, 30, 50, and 65)

Circular profile K_2

The vertical deformation is better described with $A = 10$ and the horizontal deformation with $A = 30$ (Fig. 6.19). The slope of the results $A=30$ approximates the slope of the linear regression.

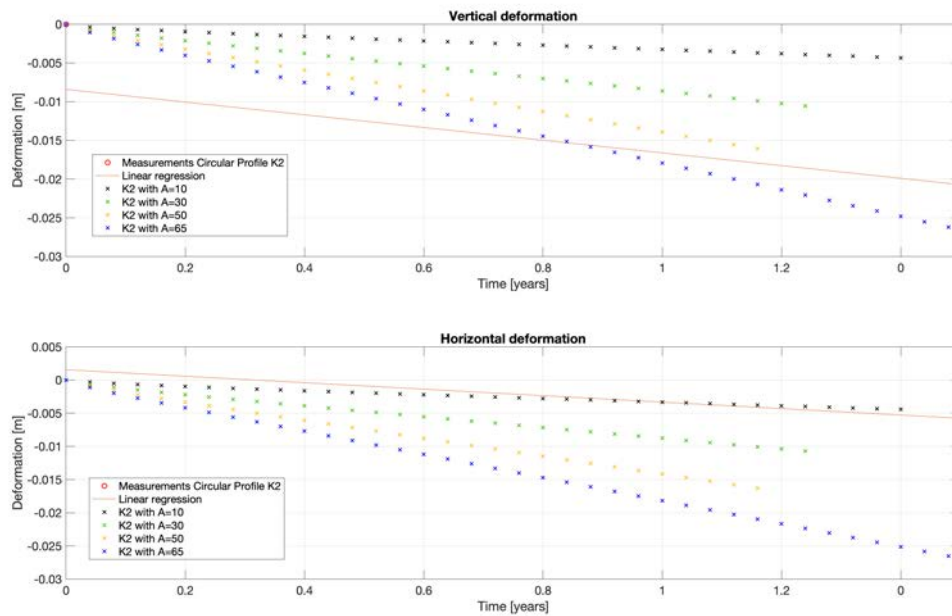


Figure 6.19 – Different modellings for the circular profile K_2 with different A factors (10, 30, 50, and 65)

Circular profile K_3

The vertical deformation is better described with $A > 70$ and the horizontal deformation with $A = 65$ (Fig. 6.20).

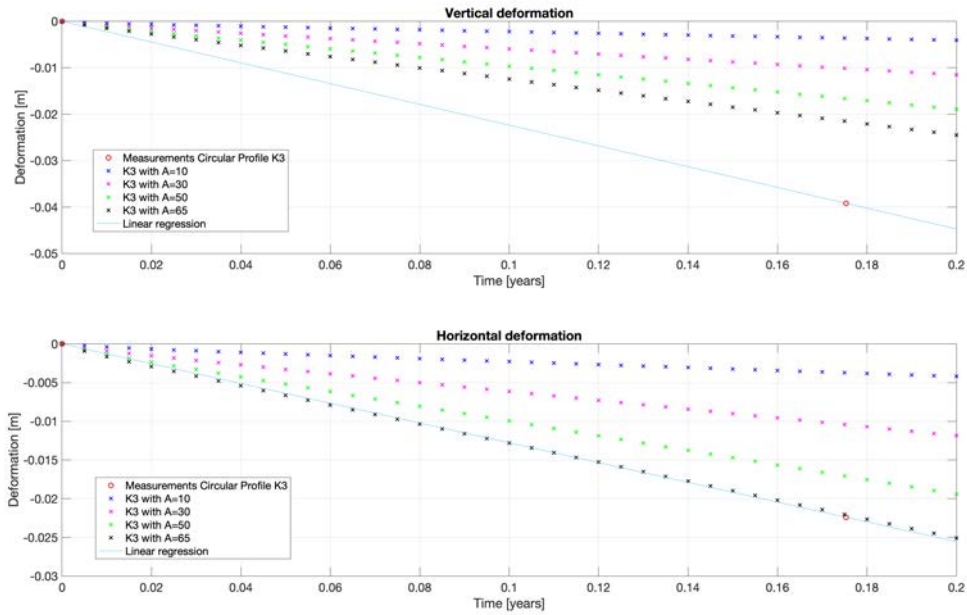


Figure 6.20 – Different modellings for the circular profile K_3 with different A factors (10, 30, 50, and 65)

Circular profile K_4

The vertical deformation is better described with $A = 30$ and the horizontal deformation with $A < 10$ (Fig. 6.21).

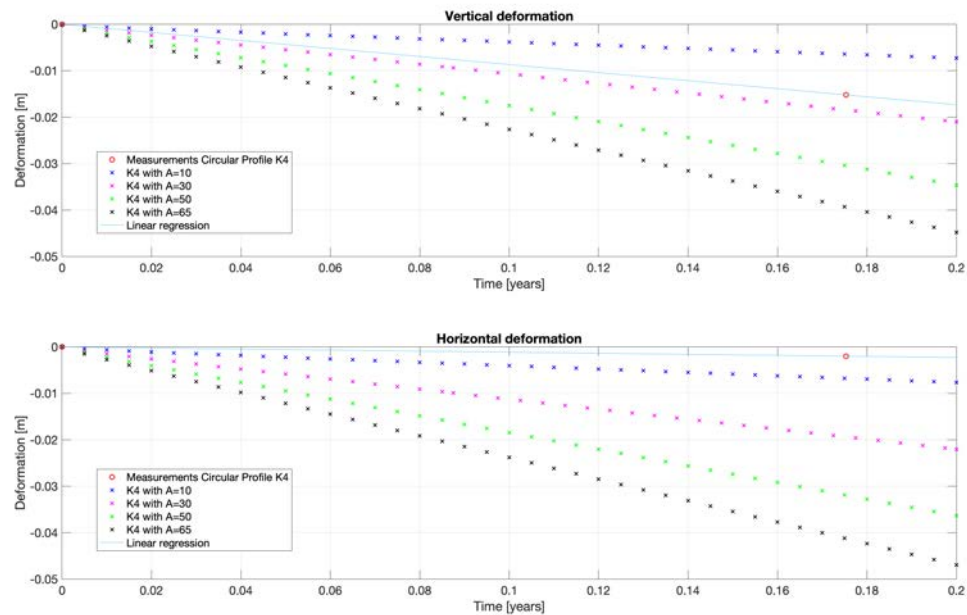


Figure 6.21 – Different modellings for the circular profile K_4 with different A factors (10, 30, 50, and 65)

6.3 Velocity in boundary conditions

Circular profile K_1

The blue dots represents the modellings, where a velocity of 0.1m/year have been applied to the boundary conditions. The A factor is $2a^{-1}MPa^{-3}$. On Figure 6.22 is good represented by the modelling. Without velocity, the measurements are horizontally good represented with a A factor smaller than 10.

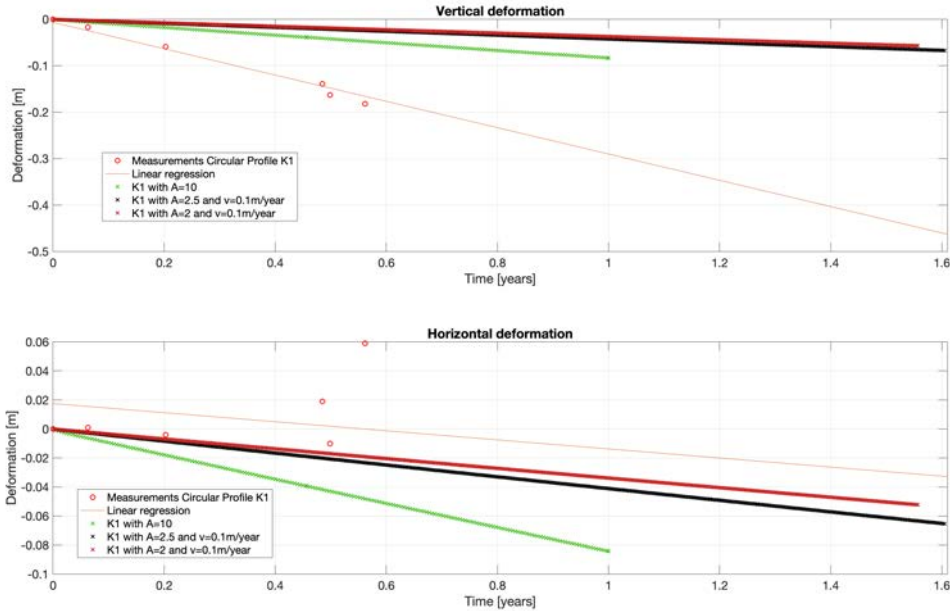


Figure 6.22 – Modellings of the circular profile without and with velocity applied to boundary conditions (Profile K_1).

Circular profile K_2

The blue dots represents the modellings, where a velocity of 0.1m/year have been applied to the boundary conditions. The A factor is $11a^{-1}MPa^{-3}$. On Figure 6.23 is good represented by the modelling. The measurements seems to be good represented without velocity by $A=30$ for the vertical and horizontal deformation. However, the vertical deformation deforms slowly. After 1.44 years, the difference between the modelling (green) and the linear regression for the horizontal deformation is 9.7mm.

Circular profile K_3

The blue dots represents the modellings, where a velocity of 0.1m/year have been applied to the boundary conditions. The A factor is $32a^{-1}MPa^{-3}$. On Figure 6.24 the horizontal deformation is almost perfectly represented with the modelling. However, the ice gallery vertically deforms slower than the measurements. If the modelling without velocity was run with $A=32$, the vertical would be slower (Fig. 6.20) than the one modelled with velocity. The horizontal deformation will also deform slower. However, the modelling without velocity applied on the boundary conditions and $A = 65$ gives similar result as a velocity of 0.1m/year and $A = 32$.

Circular profile K_4

The blue dots represents the modelling, where a velocity of 0.1m/year have been applied to the boundary conditions. The A factor is $1.75a^{-1}MPa^{-3}$. On Figure 6.25, the horizontal deformation is almost perfectly represented with the modelling. However, the ice gallery vertically deforms slower than the measurements. If the modelling without velocity was run with $A=1.75$, the vertical deformation would be slower (Fig. 6.21) than the one modelled with velocity (Fig. 6.25) Maybe,

the horizontal deformation will be good represented with $A=5$ (Fig. 6.21). The difference between the modelling and the linear regression after 1.518 years is 0.66mm.

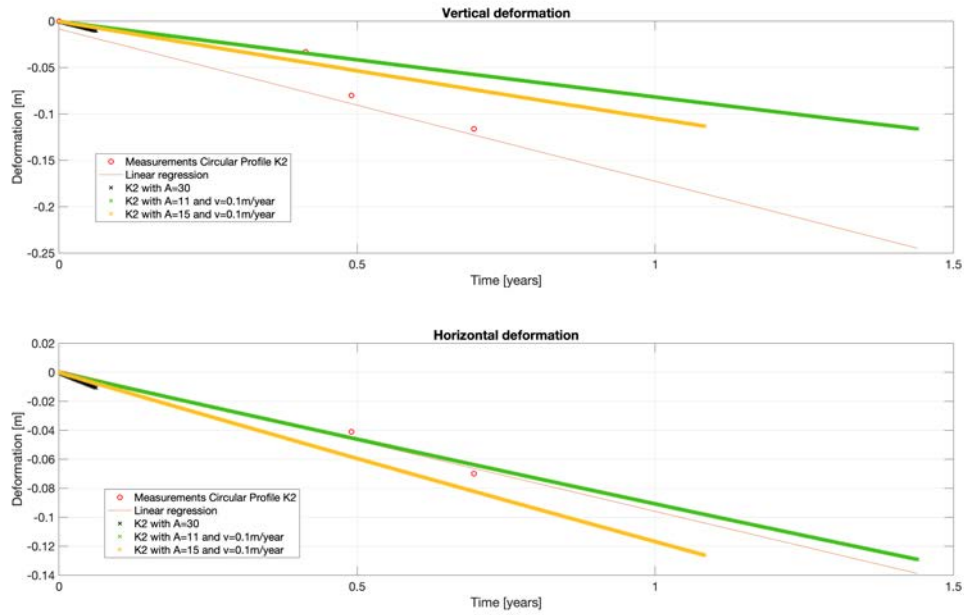


Figure 6.23 – Modellings of the circular profile without and with velocity applied to boundary conditions (Profile K_2 .)

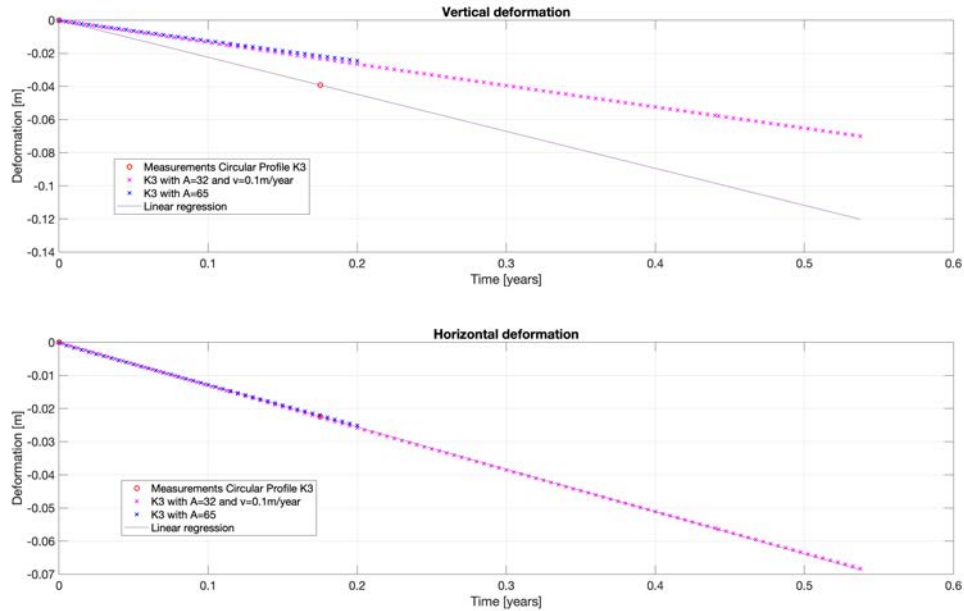


Figure 6.24 – Modellings of the circular profile without and with velocity applied to boundary conditions (Profile K_3 .)

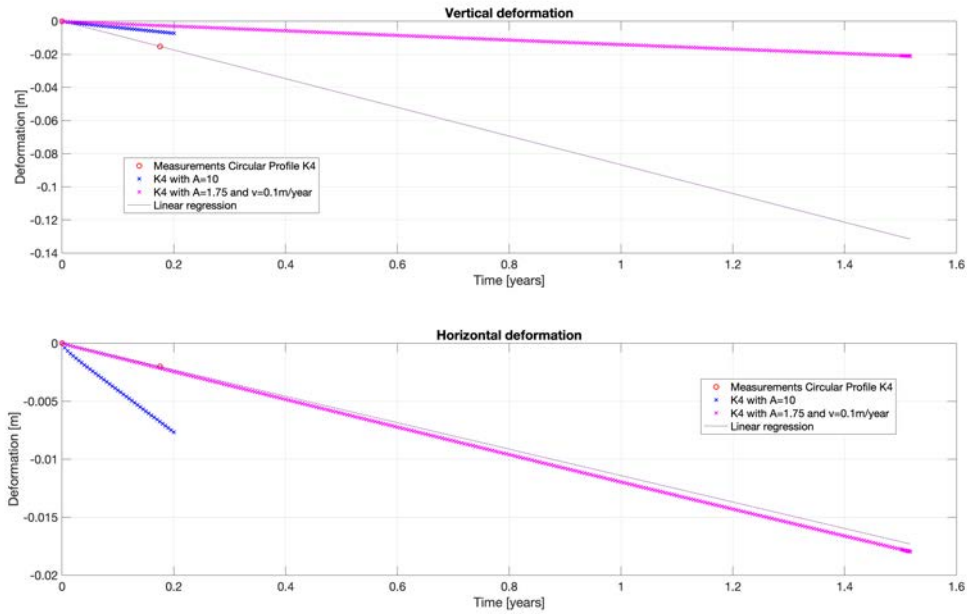


Figure 6.25 – Modellings of the circular profile without and with velocity applied to boundary conditions (Profile K_4).

6.4 Ice experiment

On Figure 6.26, the modelling represents more or less the measurements. The transient (between timesteps $t=0$ day and $t=10$ days) is little bigger for the modelling than for the measurements. In the modelling, the ice sample is faster compressed. The Burger model is used.

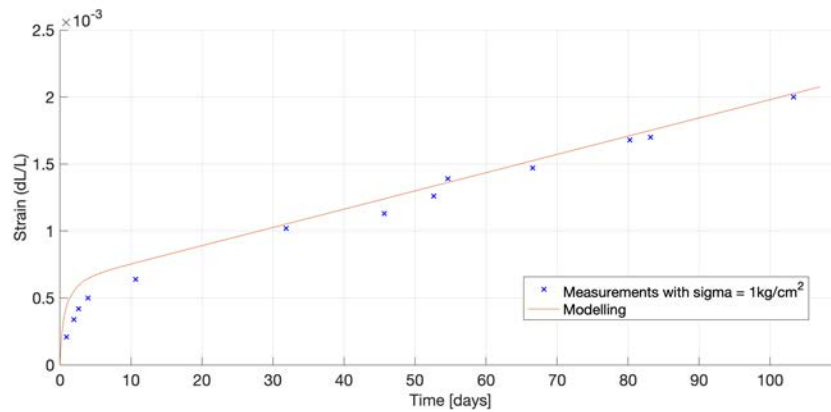


Figure 6.26 – Results from the modelling for an ice sample with a load of $\sigma = 1\text{kg}/\text{cm}^2$.

In the model, the input values are the following:

- Young's modulus = $8.9 \cdot 10^9$ Pa
- Poisson's ratio = 0.31
- Axial load = $-9.81 \cdot 10^4$ Pa
- Ice density = $850 \text{ kg}/\text{m}^3$

The system was built with four dampers and three springs. The dampers have the following values : 1s, 3s, 12s and 2.2s. The springs have the following values: $9.08 \cdot 10^{11}$ Pa, $0.81 \cdot 10^8$ Pa and $1.02 \cdot 10^8$ Pa.

Chapter 7

Analysis and discussion

7.1 Measurements

The profile K_1 has a different pattern for the horizontal deformation. The general trend gives a process of contraction (Fig. 6.1, K_1 linear regression). However, the measurements alternate between contraction and elongation of the horizontal diameter. The first explanation may result from imprecise measurements because it concerns only two measurement points for almost two years. The second explanation can be a modification of the local glacier dynamics for a short period due to the construction of the installations in the ice gallery. This phenomenon of elongation is not noted in the circular profile K_2 .

The difference of behavior between the circular profiles K_1 and K_2 are explained by their respective location. The circular profile K_1 lies in the main gallery. It is perpendicular to the glacier flow. The horizontal deformation should be bigger than the one for K_2 . However, K_1 (hm 1.25) lies at the frontier of the dividing line (hm 1.30). The flow is less strong than at the position hm 1.00. In both cases, the flow goes in the southern direction. The circular profile K_2 lies in the transversal gallery Q_{100} . The ice gallery is in the glacier flow. As seen in Table 6.1, K_2 horizontally deforms three times faster than K_1 . Concerning the vertical deformation, K_1 deforms more than K_2 . The height of the overlying ice cover can be an explanation. The overlying ice cover above K_1 is 28m and above K_2 25m.

Both circular profiles, K_3 and K_4 , are measured in the main gallery. The difference in behavior between K_3 and K_4 is noted. The circular profile K_3 finds at the position hm 0.938 and K_4 at the position hm 1.384. K_4 lies in the area of the dividing line determined by the different studies of Haefeli in the 1950s. The glacier flow is stronger at the location hm 1.00 than hm 1.30. As seen in Table 6.1, K_3 vertically deforms three times faster than K_4 . The overlying ice cover above K_3 is 16m and above K_4 20m. In this case, the height of the overlying ice cover cannot explain why there is this difference in vertical deformation between these both profiles.

In Table 6.1, K_2 and K_3 obtain a similar ratio between the horizontal and vertical deformation. K_1 and K_4 also obtain a similar ratio. The profile K_3 shows the largest deformation and K_4 the smallest one. The large deformations of K_3 could be explained by the augmentation of ice temperature in 70 years. The small deformations of K_4 could result in the location of the circular profile in the ice cap. K_4 should lie in this 0-stress area defined by Haefeli (see Chapter 3.4). The temperatures, measured in 2020, do not exceed $-2^\circ C$. The temperature is contained between $[-1.4; -1]^\circ C$ (Fig. 5.10). In the 1950s, the measured temperatures were contained between $[-2.5; -1.5]^\circ C$ (Fig. 5.7). There is an increase of $1^\circ C - 1.5^\circ C$ in 70 years. The ice thickness has decreased 10m (Fig. 3.4, 3.5, and 3.6). It means the hydrostatic pressure has also decreased. According to the four circular profiles, a lot of processes influence the deformation such as the direction of the circular profile according to the glacier flow, the distribution of the stresses in the ice cap, the ice temperature.

If the deformations follow in the long term a linear behavior. We expect for K_1 a collapse after 9.2 years, for K_2 after 13.5 years, for K_3 after 11 years, and for K_4 after 31 years. The ice gallery will not collapse everywhere at the same time. To link with the theory, we see that the measurements show this linear and continuous deformation implied by the creep (Cuffey & Paterson, 2010).

7.2 Influence of the parameters

To determine and to understand the units of the different parameters, it was necessary to model the deformations by changing only a parameter. It is easier to observe differences between the modellings and to find the most representative values to model the measurements. MOOSE has not defined units for each variable. The user should decide what are units for time, A factor, Young's modulus. The chosen units should be, then, consistent and make sense. It means, if the timesteps are considered to be year, then the temporal part of the velocity will be also in year and not in second. The results of Chapter 6.2 have been modelled with simple boundaries conditions. The displacements $disp_x$, $disp_y$, and $disp_z$ have a value of 0 at the bottom of the mesh. The displacement $disp_x$ has a value of 0 at the front and the back of the mesh. The displacement $disp_y$ has a value of 0 on the right and left faces of the mesh.

7.2.1 Changing the width of the mesh

By testing different widths for the mesh, it has been noted that the width should be at least three times larger than the height above the gallery. For the circular profiles K_1 and K_2 , the chosen width is 100m and for K_3 and K_4 60m. From these chosen widths, the differences between the modelled results are small. For K_1 and K_2 , a mesh with a width of 120m could be chosen. It will take more time to compute since there are many more nodes. The difference between a mesh of 100m and 120m is maybe 2-4mm after two years. It is low.

7.2.2 Changing Young's modulus

As mentioned in Chapter 7.2, MOOSE does not define in advance the unit. It was necessary to find if Young's modulus is in GPa or MPa. Young's modulus describes the rigidity of the material. According to the measurements and the theory, we expect to get a linear relation between time and deformation. Young's modulus of ice is defined as 8.7 GPa. However, on the four figures (Fig. 6.6-6.9), the blue dots follow a curved pattern. It means, Young's modulus is not in GPa. The second possibility is 8'700 MPa. The four figures (Fig. 6.6-6.9) show a linear pattern. However, it is noted that $Y=870$ and $Y=8'700$ give similar results. Differences between $Y=870$ and $Y=8700$ have been noted in Fig. 6.8.

7.2.3 Changing n and m coefficient

The coefficients n and m have been defined as 3 and 0 for creep models applied for glaciers. However, it is interesting to explore the influence of these both parameters, since they are empirically defined.

If the n coefficient is large, the deformation will be small. The coefficient n is applied in the equation (2.6.4). The n exponent multiplies a difference. If the difference $(\sigma - 3G\Delta p)$ is very small and n large, the strain will be small. The results given by MOOSE, make sense for $n=4$. Hooke(2005) represented the relation between the pressure and the rate of contraction with $n=3.11$, which he empirically defined. According to the flow laws (eq. 2.3.8 and 2.3.9), if the ratio $\frac{\sigma}{B} < 1$, bigger is the n coefficient, smaller is the strain rate. The coefficient m shows a curved pattern for $m > 0$. As for the case of Young's modulus, we expect a linear relation between the deformation and the time. The coefficient $m = 0$ is the most appropriate solution.

7.2.4 Changing A factor

By changing the A factor, we see different reactions according to the circular profiles. As seen in Chapter 7.1, the circular profiles K_2 and K_3 have the highest horizontal deformations, and the circular profiles, K_1 and K_4 , the smallest one. Higher is the A coefficient, the warmer is the ice. It means, the ice has less resistance to flow. The results give $A=65$ for K_3 , $A=30$ for K_2 , $A=10$ for K_1 and K_4 . According to the theory and the observations, the magnitude of the A values represents the measurements. According to Figure 2.8, $A = 30a^{-1}MPa^{-3}$ (K_2) represents ice at temperature approximately of $-5^\circ C$. $A = 65a^{-1}MPa^{-3}$ (K_3) represents a temperature of approximately $-1^\circ C$. $A = 10a^{-1}MPa^{-3}$ (K_1 and K_4) represents a temperature of $-10^\circ C$. As seen in Fig. 5.7, 5.8, 5.9, and 5.10, the temperature does not reach $-10^\circ C$ and not $-5^\circ C$. The temperatures are contained between $[-4; -1]^\circ C$. It is noted that the most appropriate A factors to model the vertical deformations are bigger than the one to model the horizontal deformations. K_3 gets the most appropriate A factor.

7.3 Velocity in BCs

For the modelling with a velocity, the boundaries conditions applied to $disp_y$ have been modified. For the bottom face, $disp_y$ takes the value of 0. On the right face, the function $0.1 \cdot t$ is applied to $disp_y$. On the left face, the function $-0.1 \cdot t$ is applied to $disp_y$. We assume that the velocity has the unit m/year. According to Fig. 3.7, the maximal velocity was 33cm/year. In Chapter 3.5, it is stressed that the ground sinks with a velocity of 10cm/year. It can justify our choice of 0.1m/year for the boundary conditions. When the velocity is applied, the A factor decreases. However, a similar results can be found without velocity. Moreover, K_1 and K_4 get small values for A (2.5 and 1.75). K_2 and K_3 get bigger values for A (11 and 32), but smaller than the values got in Chapter 7.2.4. With the results of K_3 , we noted that the A factor makes more sense without velocity in boundary conditions because $A = 65$ corresponds to a temperature of $-1^\circ C$, what was measured in 2020 (Fig. 5.10). For the four circular profiles, something should still be added to the model to model the vertical deformation correctly. We tried to add different axial load in the boundary conditions. However, the modelling crashed, because the time step was always too large.

7.4 Ice experiment

The number of springs and dampers gives the shape of the transient. The last damper determines the slope of the linear pattern (after 10 days). We suppose that the creep viscosity is given in seconds because the creep modulus is in Pa, and the viscosity was in $Pa \cdot s$. The ideal will be to create a model with only a spring and a damper to have a simple model. The problem with this model was the choice of the creep modulus and creep viscosity. In the beginning, many springs and dampers have been put together with the same value. Since many dampers-springs systems have the same value, we can simplify the system. We calculate the equivalent creep modulus (as done for the equivalent resistance in electricity for a system installed in parallel). Then, the creep modulus and the creep viscosity were tuned until to find an appropriate solution. It is not a good way to find the solution and to explain the physical processes through the model. According to Figure 5.12, when the pressure is increased, the specific strain rate does not follow a linear behavior, but an exponential one. The transient corresponds to the elastic deformation. Then, it is the viscous deformation.

7.5 Modelling

7.5.1 Choice of the model

Many modellings were tested before this model was presented. The first model applied was a Kelvin-Voigt model. Elasticity is described by the spring with Young's modulus. Viscosity is described by the damper with the viscosity. The problem of this model is the choice of Young's modulus and the viscosity. Moreover, the number of dampers and springs was complicated to define. The second test was to apply the Burger model. It consists of n springs and n+1 dampers. The third tested model was the Maxwell model. From these three models, the best one was the Burger model. However, it was complicated to define an appropriate system. The viscosity in MOOSE was described by the *creep_viscosity*. However, this *creep_viscosity* is not the viscosity but the characteristics times of the damper. The fourth try was to implement a plane-strain model. It should be easier and faster because we are working only in 2D and not in 3D. There are less nodes. The mesh was realized with GMSH. It defines differently the nodes, the planes, the lines of the mesh as in MOOSE. Then, it was difficult to implement the GMSH-mesh in MOOSE due to the name of the faces. It creates some troubles in the definition of the boundary conditions. The model crashed. The last model was a creep model. We get better results with this model. It was also easier to choose the values and to find what were the units of the different parameters. The difference between the Kelvin-Voigt model and the creep model is the presence of transient. In the creep model, the relation between time and deformation is linear. In the Kelvin-Voigt model, the modelling begins with a transient, and then it shows a linear pattern. This transient-linear pattern works in case of uniaxial compression because we apply a weight on the material, and it reacts fast. Then, it stabilizes. In the case of glacier motion, it does not work so. This quick elastic compression had already occurred a long time ago.

7.5.2 Choice of the units

For each model mentioned in the Chapter 7.4.1, an issue was to enter the good value for each variable. Without knowing the unit, it can be complicated. Many tests were realized already to know if the time step is second, day or year. At the end, we worked with time step in year. For the models Kelvin-Voigt, Maxwell and Burger, a big difficulty was to find out the unit of the time characteristics (*creep_viscosity*) and also the unit of the time step. In the creep model, the units have been defined has MPa for the Young's modulus and $a^{-1}MPa^{-3}$ for the A factor.

7.5.3 Time steps

The choice of the time step is important to gain time in the modelling. A time stepper with a constant time change has been chosen. It was also possible to choose a time stepper with a logarithmic change. It was noted that it was for this modelling faster with a constant time change. It is better to choose small time change and not to have a big amplitude between the minimal time change and the time change because it will be taken lots of time to find the solution for the next time step if the difference is too large. MOOSE begins to compute with the time change. If it finds no solution, it changes the time step. It does that until it finds a solution. This computation is stopped when it reaches the minimal time step. The second reason to choose a small time step is when we are modelling, we gain time. It was noted that if the first time step is big and there is a solution for this big time step, it would take more time to get a solution. Before to have good modellings, the modelling is tuned. When we are in the tuning part, we do not need to have lots of solutions. If the solution does not correspond to our expectations, we kill the modelling and we change the values. With small time steps, we can observe faster what the modelling is doing. Generally, the time step was chosen as 0.01 in the best cases or 0.005 or 0.001. The disadvantage with small time steps is the size of the outputs. The smaller is the time step, the bigger is the number of time steps.

7.6 Density

The measurements of the ice density in 2020 show some errors. It can be explained by the methodology. The ice was grabbed in the wall. By turning the ice driller, ice is warmed. The ice structure has been modified. It can explain the high value obtained for ice density. Ice was like some snow (see Fig. 4.3) after drilling. In this configuration, ice has time to transform by the changing in temperature between the ice and the air. In the reports of Greenland, they cut ice cube in the glacier to measure the density. The method used in Greenland requires more material to cut perfectly the ice cube. In the 1950s, they chose an ice density of $850kg/m^3$. According to Cuffey and Paterson (2010, page 12), glacier ice is contained between $830kg/m^3$ and $923kg/m^3$. Firn is contained between $700kg/m^3$ and $800kg/m^3$. In their reports, they do not explain if they measured it or if they assumed this value. In accordance with Cuffey and Paterson (2010, page 12 and 13), a lot of factors play a role in ice density. Usually, pure ice at $0^\circ C$ should have a value of $917kg/m^3$. In this case, the pressure applied to ice is low. If the pressure increases, the density also increases and could reach $921kg/m^3$. So, choosing ice density of $900kg/m^3$ is contained between $850kg/m^3$ and $917kg/m^3$.

7.7 Georeferencing

It is possible that the georeferencing of the different maps are not perfectly precise. The difference can be of some millimeters. It is explained by the position of the georeferencing points. It is complicated to reach precisely the points to georeference due to the pixelation of the image. It can be problematic when we should measure, for example, deformation where the magnitude corresponds to some centimeters or millimeters. This can be noted in Appendix D.

7.8 Discussion

As seen, something is missing to model the vertical deformation correctly. Then, we note two main differences between the measured and modelled profiles. We can group together the profiles K_1 and K_4 , and K_2 and K_3 . It let suppose the importance of the stress in the ice cap, since K_1 and K_4 find in a calm location, where the ice motion is low. K_2 and K_3 find in a region with higher stresses. K_2 and K_3 are almost in the middle of the area, where the glacier flows into the

southern direction. The vertical deformation cannot be explained only by the hydrostatic pressure since the profile K_3 deforms more strongly than the profile K_2 . The overlying ice above K_2 is 9m higher than the one above K_3 . Temperature also plays a role in the deformations. We expect fewer deformations if the glacier has a smaller volume because there is less stress applied to the glacier. However, higher deformation can be expected if the temperature increases. The profile K_1 has been done after the construction of the ice galleries. The high vertical deformation, with comparison to the profile K_4 , can be explained by an adaptation of the glacier to this gallery. We think that this double ice motion in the ice cap plays an important role in the deformations. The temperature also increases the viscosity of the ice and then the ice motion. We see with the profile K_3 an appropriate result for the parameter A. The three other profiles get too small A factors. As written in Chapter 2.4.2, viscosity depends on many factors like the pressure, the temperature, and the applied stress. Most of the studies investigate the behavior of ice in the laboratory and on small samples. The advantage of laboratory experiments is the possibility to control the parameters. In the glacier, we cannot control the temperature, the pressure, and the applied stress.

In the 1950s, they did some links with the ice cap in Greenland. The ice gallery in Greenland has other characteristics. The ice gallery has an ice overlying of 30m (see Appendix B). The ice density is smaller because it is firm and snow, not glacier ice. The values are contained between $600kg/m^3$ and $700kg/m^3$. The ice temperature is much colder ($-27^\circ C$). We expect fewer deformations in this situation due to the low density and cold temperature.

Cuffey and Paterson (2010) stress the influence of temperature, hydrostatic pressure, water content, density, grain sizes, impurities, preferred-orientation fabric. Hooke (2005) also stresses the influence of the preferred-orientation fabric in the viscosity. According to Cuffey and Paterson (2010, page 66), under $830kg/m^3$, we should expect an increase of the strain rate. The density at the Jungfraujoch does not play a major role since ice densities are $850kg/m^3$ and $900kg/m^3$. It can play a role in Greenland, where the first 30 meters have a smaller density. The ice grain sizes also are more important for the Jungfraujoch than for Greenland. Under $-10^\circ C$, the viscosity depends partly on the ice grain sizes (Cuffey & Paterson, 2010, page 66). Cuffey and Paterson (2010, page 73) present a table with different value for the A factor at temperatures $0^\circ C$, $-2^\circ C$ and $-10^\circ C$. For $0^\circ C$, the recommended value is $75.7a^{-3}MPa^{-3}$. However, A factor can be contained between $75.7a^{-3}MPa^{-3}$ and $293.3a^{-3}MPa^{-3}$. We see here also the influence of many parameters.

More studies on the topics are needed to have a better understanding of the processes. Moreover, it can be interesting to compare the ice deformations in temperate ice galleries to observe the influence of water on the viscosity. Maybe the stress conditions in the temperate ice gallery are a little less complicated as at the Jungfraujoch, where many processes play a role in the deformations. Finally, the model should also be improved to represent the vertical deformation better.

Chapter 8

Conclusion

The motion of the Jungfrauoch ice cap is controlled by lots of factors. A particularity in the motion is this dividing line, where a part of the glacier goes in the southern direction, and the other part flow in the northern direction. There is thus a part in the glacier where the flow is 0. This dividing area has been observed in the investigation of the deformation in the main ice gallery. Moreover, the flow is not everywhere the same as observed with K_1 - K_4 and K_2 - K_4 . In some parts, the glacier flows more strongly than in other parts. The model needs to be improved to model perfectly the measurements. The values for the A factors are very low for the circular profile K_1 and K_4 , and bigger for the circular profiles K_2 and K_3 . For high deformations, the A factor is large. For small deformations, the A factor is small. The magnitude for A factor corresponds to the theory. The values for A factor do not correspond to the theory (except for K_3). It was noted that in 70 years, the circular profiles show a similar pattern and behavior at similar locations. With the profile K_3 , we observe the influence of the temperature on the glacier flow. An increase in the temperature increases the deformations.

The different trials for the models show us the complexity to find an appropriate model to represent at best measurements since five different models have been used. The sensitivity of parameters highlights the importance of inserting the right units and understanding the units of the model. The negative points in the modelling, highlighted by the strain plane model, is the ability to import a mesh from GMSH in MOOSE. Even if MOOSE gives the possibility to create a mesh inside the script, it remains complicated in MOOSE to create a complex mesh as used for the ice galleries. It is the reason why GMSH is used. It is important to choose the mesh as small as possible to gain time in the modelling.

To have a better understanding of the deformation in the Jungfrauoch ice cap is necessary to develop the project of the Jungfrau Railway at the relay station. A better understanding of viscosity is important for other cases as the hanging glaciers or for the other glaciers. The thermal regime of hanging glaciers is cold. With the increase in air temperature, their thermal regime will be temperate. The consequence will be the increase in the instability of hanging glaciers. It is, in this case, important to understand how the viscosity evolves and how the glacier will flow. For the other glaciers, the viscosity could accelerate or modify the glacier flow and then causes natural hazards.

To conclude, the model should be improved to get more appropriate results. However, it was already possible to describe some processes with the modellings. It could be interesting to compare results with ice galleries in temperate ice, where we expect a higher viscosity. With ice density and temperature measured in Greenland, we expect different values for the viscosity and a different behaviors of deformation.

References

- Adams, E. E., & Sato, A. (1993). Model for effective thermal conductivity of a dry snow cover composed of uniform ice spheres. *Annals of Glaciology*, (18), 300-304. doi: 10.3189/S026030550001168X
- Amiroudine, S., & Battaglia, J.-L. (2014). *Mécanique des fluides : Cours et exercices corrigés* (2nd ed.). Dunod.
- Barnes, H. A., Hutton, J. F., & Walters, K. (1989). *An introduction to rheology*. Amsterdam, Elsevier Science.
- Bauer, A. (1952). Wissenschaftliche Ergebnisse der französischen Polarexpeditionen. *Wissensch. Rundschau, H. 1*.
- Blatter, H., & Hutter, K. (1991). Polythermal conditions in arctic glaciers. *Journal of Glaciology*, 37(126), 261-269. doi: 10.1017/S0022143000007279
- Boon, S., & Sharp, M. (2003). The role of hydrologically-driven ice fracture in drainage system evolution on an arctic glacier. *Geophysical research letters*, 30(18), 1-4. doi: 10.1029/2003GL018034
- Copland, L., Sharp, M. J., & Nienow, P. W. (2003). Links between short-term velocity variations and the subglacial hydrology of a predominantly cold polythermal glacier. *Journal of Glaciology*, 49(166), 337-348. doi: 10.3189/172756503781830656
- CRM. (2012). *Formulaires et tables. Mathématiques, Physiques, Chimie*. Editions du Tricorne.
- Cuffey, K. M., & Paterson, W. S. B. (2010). *The physics of glaciers* (4th ed.). Oxford, Butterworth-Heinemann.
- Deeley, R. M. (1908). The viscosity of ice. *Proc. R. Soc. London, Ser. A*, 81(547), 250-259. doi: 10.1098/rspa.1908.0077
- Deeley, R. M., & Parr, P. H. (1913). The viscosity of glacier ice. *The London, Edinburgh, and Dublin Philosophical Magazine and Journal of Science*, 26(151), 85-111. doi: 10.1080/14786441308634957
- Duval, P., Ashby, M. F., & Anderman, I. (1983). Rate-controlling processes in the creep of polycrystalline ice. *Journal of Physical Chemistry*, 87(21), 4066-4074.
- ETHZ. (1964). Picture of the ice cap of the Jungfrauoch taken on 1964.
- ETHZ. (2019). Plan of the ice gallery in 2019 at the Jungfrauoch.
- Expéditions Polaires Françaises. (1950). Campagne au Groenland. *Série scientifique*, 15.
- Fountain, A. G., & Walder, J. S. (1998). Water flow through temperate glaciers. *Reviews of Geophysics*, 36(3), 299-328. doi: 10.1029/97RG03579
- Fowler, A. C. (1997). *The mathematics of models for climatology and environment* (Glaciers and ice sheets. In: Díaz J.I. ed., Vol. 48). NATO ASI Series (Series I: Global Environmental Change), Berlin, Heidelberg, Springer.
- Fowler, A. C., & Larson, D. A. (1978). On the flow of polythermal glaciers: I. model and preliminary analysis. *Proceedings of the Royal Society*, 363(1713), 217-242. doi: 10.1098/rspa.1978.0165
- Gilbert, A. (2013). *Modélisation du régime thermique des glaciers: applications à l'étude du risque glaciaire et à la quantification des changements climatiques à haute altitude*. Thèse de doctorat, Grenoble, Sciences de la Terre, Université de Grenoble.
- Giorla, A. (2017). Implementation of Concrete Creep Model in Grizzly. United States: N. p. doi: 10.2172/1460224
- Glen, J. W. (1955). The creep of polycrystalline ice. *The Royal Society*, 228, 519-538. doi: 10.1098/rspa.1955.0066
- Glen, J. W. (1958). The flow law of ice. a discussion of the assumptions made in glacier theory, their experimental foundations and consequences. *International Association of Scientific Hydrology Publication 47 (Symposium at Chamonix 1958 — Physics of the Movement of the Ice)*, 171-183.
- Greve, R., & Blatter, H. (2009). *Dynamics of ice sheets and glaciers*. Berlin, Springer.

- Haefeli, R. (1953). *Höhenstation PTT Jungfrauoch. Eisstollen. Generelles Arbeitsprogramm (22.10.1953)* (No. 624). Zürich, VAW ETHZ.
- Haefeli, R. (1956). *Eisstollen. Jungfrauoch, Höhenstation PTT. Bericht über das Verhalten der Eisstollen und der Eiscalotte im Jahre 1955 (30.04.1956)*. Zürich, VAW ETHZ.
- Haefeli, R. (1957). *Eisstollen Jungfrauoch. Höhenstation PTT. Bericht über das Verhalten der Eisstollen und der Eiscalotte im Jahre 1956/57 (30.09.1957)*. Zürich, VAW ETHZ.
- Haefeli, R. (1963). Observations in ice tunnels and the flow law of ice. *Ice and Snow: Properties, Processes and Applications*(39), 162-186.
- Haefeli, R., & Brentani, F. (1954a). Beobachtungen in einer kalten Eiscalotte. *Association Internationale d'Hydrologie*(39), 394-409.
- Haefeli, R., & Brentani, F. (1954b). *Eisstollen. Jungfrauoch Höhenstation PTT. Bericht über das Verhalten des Zugangsstollens u. der Beobachtungstollen in der Eiscalotte (25.11.1954) - Wissenschaftlicher Bericht* (No. 624a). Zürich, VAW ETHZ.
- Haefeli, R., & Brentani, F. (1955). Observation in a cold ice cap. *Journal of Glaciology*(18), 623-630.
- Haefeli, R., & Kasser, P. (1948). *Beobachtungen im Firn- und im Ablationsgebiet des Grossen Aletschgletschers*. in : Mitteilungen der Versuchsanstalt für Wasserbau, Hydrologie und Glaziologie (VAW) an der Eidg. Technischen Hochschulen (ETH) Zürich, Nr. 15, 3-12.
- Haefeli, R., & Schnitter, G. (1954). *Eisstollen. Jungfrauoch Höhenstation PTT. Bericht über das Verhalten des Zugangsstollens u. der Beobachtungstollen in der Eiscalotte (25.11.1954) - Technischer Bericht* (No. 624a). Zürich, VAW ETHZ.
- HFSJG. (2019). *History of the High Altitude Research Station Jungfrauoch*. Retrieved 18.09.2019, from <https://www.hfsjg.ch/en/jungfrauoch/history/>
- Hooke, R. L. (1981). Flow law for polycrystalline ice in glaciers: comparison of theoretical predictions, laboratory data, and field measurements. *Rev. Geophys. Space Phys.*, 19, 664-672. doi: 10.1029/RG019i004p00664
- Hooke, R. L. (2005). *Principles of glacier mechanics* (2th ed.). Cambridge, University Press.
- Hutter, K. (1983). *Theoretical glaciology*. Springer.
- Hutter, K., Blatter, H., & Funk, M. (1988). A model computation of moisture content in polythermal glaciers. *Journal of Geophysical Research*, 93(B10), 205-212. doi: 10.1029/JB093iB10p12205
- Höppler, F. (1941). Die plastizität des eises. *Kolloid-Zeitschrift*(97), 154-160. doi: 10.1007/BF01502642
- Irvine-Fynn, T. D., Hodson, A. J., Moorman, B. J., Vatne, G., & Hubbard, A. L. (2011). Polythermal glacier hydrology: a review. *Reviews of Geophysics*, 49(4). doi: 10.1029/2010RG000350
- Jungfrau. (2019). *Jungfrau Railway: Rocky road to the project of the century*. Retrieved 18.09.2019, from <https://www.jungfrau.ch/en-gb/jungfrauoch-top-of-europe/construction-of-the-jungfrau-railway/>
- Jungfrau Holding AG. (2018). *Generalversammlung JBH vom 14. Mai 2018*. Retrieved 22.09.2019, from <https://www.jungfrau.ch/fileadmin/unternehmen/generalversammlungen/Ausfuehrungen-CEO-GV-JBH-2018.pdf?v=1526558250>
- Lüthi, M. P., & Funk, M. (2001). Modelling heat flow in a cold, high-altitude glacier: interpretation of measurements from colle gnifetti, swiss alps. *Journal of Glaciology*, 47(157), 314-324. doi: 10.3189/172756501781832223
- Malvern, L. E. (1969). *Introduction to the mechanics of a continuous medium*. Prentice-Hall.
- McConnel, J. C. (1891). I. on the plasticity of an ice crystal. *Proceedings of the Royal Society*, 49(296-301), 323-343. doi: 10.1098/rspl.1890.0099
- MeteoSwiss. (2020). Lufttemperatur 2m über Boden - Monatsmittel (01.01.1950-01.12.1959/01.01.2010-01.12.2019). *MeteoSwiss, CLIMAP-net*.
- MOOSE Framework. (2020). *Advanced capability, delivered simply*. Retrieved 09.01.2020, from <https://mooseframework.inl.gov/old/>
- Morard, S. (2020). Picture of the ice cap of the Jungfrauoch taken on 06.02.2020.
- Moyer, A. E. (1977). Robert hooke's ambiguous presentation of "hooke's law". *Isis*, 68(2), 266-275.
- Nye, J. F. (1953). The flow law of ice from measurements in glacier tunnels, laboratory experiments and the jungfrauoch borehole experiment. *Proceedings of the Royal Society, A219*(1139), 477-489. doi: 10.1098/rspa.1953.0161
- Paterson, W. S. B. (1994). *The physics of glaciers* (3th ed.). Oxford, Pergamon.
- Paterson, W. S. B. (1999). *The physics of glaciers* (3th ed.). Oxford, Butterworth-Heinemann.
- Perutz, M. F. (1947). Report on problems relating to the flow of glaciers. *Journal of Glaciology*, 1(2), 47-51. doi: 10.3189/S0022143000007541

- Pettersson, R., Jansson, P., & Blatter, H. (2004). Spatial variability in water content at the cold-temperate transition surface of the polythermal storglaciären, sweden. *Journal of Geophysical Research - Earth Surface*, 109(F02009), 1-12. doi: 10.1029/2003JF000110
- Robin, G. d. Q. (1954). Some factors affecting the temperature distribution in large ice sheets. *Rapport UGGJ, de Rome*.
- Schnitter, G., & Kasser, P. (1958). *Sondierbohrungen und Temperaturmessungen im Oktober 1958 zur Ermittlung der Felsoberfläche und der Permafrostverhältnisse unter der Eiskalotte Jungfrauoch als Unterlagen zur Projektierung eines Felsstollens (25.11.1958)*. Zürich, VAW ETHZ.
- Slaughter, W. S. (2012). *The linearized theory of elasticity*. Springer Science Business Media.
- Strang, G., & Fix, G. J. (1973). *Finite-Element Method*. New York, Prentice Hall.
- Swisstopo. (2019). *SwissAlti3D of Switzerland from WMS*. Retrieved 22.09.2019, from <https://wms.swisstopo.admin.ch>
- Tanner, R. I. (2002). *Engineering rheology* (2nd ed.). Oxford University Press.
- Timoshenko, S. P., & Goodier, J. N. (1970). *Theory of elasticity*. McGraw-Hill Book Company.
- Van Vliet-Lanoë, B. (2005). *La planète des glaces : Histoire et environnements de notre ère glaciaire*. Vuibert.
- Volmar, F. A. (1962). Poisson d'avril en 1886 - Réalité gigantesque en 1912, Chemin de fer du Jungfrauoch. *Le Confédéré*, 102(81), 1-6.
- Vögtli, K. (1959). *Untersuchungen im Eistollen auf dem Jungfrauoch (21.04.1959)* (No. 14.137). Generaldirektion PTT, Forschungs- und Versuchsanstalt.
- Wegmann, M. R. (1998). *Frostdynamik in hochalpinen Felswänden am Beispiel der Region Jungfrauoch-Aletsch* Doktorarbeit, Zürich, Naturwissenschaft,ETH. doi: 10.3929/ethz-a-001956015
- Weinberg, B. (1907). Über den koeffizienten der inneren reibung des gletschereises und seine bedeutung für die theorien der gletscherbewegung. *Zeitschrift für Gletscherkunde*, Bd. 1(Ht. 5), 321-347.

Appendix A

Theory

A.1 Movement of glacier ice

The ice velocity in the three directions (x-, y-, and z-direction) can be described with an ice volume $V = dx \cdot dy \cdot dz$ (Fig. 2.2). Into the volume V, ice moves with a velocity of u, v, and w in the x-, y-, and z-direction respectively (Fig. 2.2). The vector velocity is defined as $\vec{U}_{in} = (u, v, w)$. Out the volume V, the velocity is defined by the vector \vec{U}_{out} (eq. A.1.1) (Hooke, 2005, page 9).

$$\text{Velocity out the volume : } \vec{U}_{out} = \begin{pmatrix} u + \frac{\partial u}{\partial x} dx \\ v + \frac{\partial v}{\partial y} dy \\ z + \frac{\partial w}{\partial z} dz \end{pmatrix} \quad (\text{A.1.1})$$

By means of the velocities U_{in} and U_{out} (Fig. 2.2), it is possible to determine the mass flux into the volume M_{in} (eq. A.1.2) and out the volume M_{out} (eq. A.1.3) (Hooke, 2005, page 9).

$$\text{Mass flux into the volume V : } \vec{M}_{in} = \rho \cdot \begin{pmatrix} u \cdot dy \cdot dz \\ v \cdot dx \cdot dz \\ w \cdot dx \cdot dy \end{pmatrix} \quad (\text{A.1.2})$$

$$\text{Mass flux out the volume V : } \vec{M}_{out} = \rho \cdot \begin{pmatrix} (u + \frac{\partial u}{\partial x} dx) \cdot dy \cdot dz \\ (v + \frac{\partial v}{\partial y} dy) \cdot dx \cdot dz \\ (w + \frac{\partial w}{\partial z} dz) \cdot dx \cdot dy \end{pmatrix} \quad (\text{A.1.3})$$

The sum of mass flux into the volume M_{in} and out the volume M_{out} gives the change in mass with time $\frac{\partial m}{\partial t}$ (eq. A.1.4) (Hooke, 2005, page 9). Mass flux into the volume M_{in} is positive, because it is a gain of mass and mass flux out the volume M_{out} is negative, because it corresponds to a mass loss.

$$\begin{aligned} \text{Change in mass with time : } \frac{\partial m}{\partial t} &= \rho \cdot u \cdot dy \cdot dz - \left(\rho u + \frac{\partial \rho u}{\partial x} dx \right) dy dz \\ &+ \rho \cdot v \cdot dx \cdot dz - \left(\rho v + \frac{\partial \rho v}{\partial y} dy \right) dx \cdot dz + \rho \cdot w \cdot dx \cdot dy - \left(\rho w + \frac{\partial \rho w}{\partial z} dz \right) dx \cdot dy \\ &= \rho \cdot u \cdot dy \cdot dz - \rho \cdot u \cdot dy \cdot z - \frac{\partial \rho u}{\partial x} \cdot dx \cdot dy \cdot dz \\ &+ \rho \cdot v \cdot dx \cdot dz - \rho \cdot v \cdot dx \cdot dz - \frac{\partial \rho v}{\partial y} \cdot dx \cdot dy \cdot dz + \rho \cdot w \cdot dx \cdot dy - \rho \cdot w \cdot dx \cdot dy - \frac{\partial \rho w}{\partial z} \cdot dx \cdot dy \cdot dz \end{aligned}$$

$$= - \left(\frac{\partial \rho u}{\partial x} + \frac{\partial \rho v}{\partial y} + \frac{\partial \rho w}{\partial z} \right) \cdot dx \cdot dy \cdot dz \quad (\text{A.1.4})$$

The equation (A.1.4) is divided by $-\rho \cdot dx \cdot dy \cdot dz$:

$$-\frac{1}{\rho \cdot dx \cdot dy \cdot dz} \frac{\partial m}{\partial t} = \frac{\partial u}{\partial x} + \frac{\partial v}{\partial y} + \frac{\partial w}{\partial z} = \vec{\nabla} \cdot \vec{U}_{in} \quad (\text{A.1.5})$$

A.2 Strain

$$\text{Strain for } \epsilon_{xx} : \epsilon_{xx} = \frac{\partial \vec{x}}{\partial x}$$

$$\text{Strain for } \epsilon_{yy} : \epsilon_{yy} = \frac{\partial \vec{y}}{\partial y} \quad (\text{A.2.1})$$

$$\text{Strain for } \epsilon_{zz} : \epsilon_{zz} = \frac{\partial \vec{z}}{\partial z}$$

$$\text{Strain for } \epsilon_{xy} : \epsilon_{xy} = \frac{1}{2} \left(\frac{\partial \vec{x}}{\partial y} + \frac{\partial \vec{y}}{\partial x} \right)$$

$$\text{Strain for } \epsilon_{yz} : \epsilon_{yz} = \frac{1}{2} \left(\frac{\partial \vec{y}}{\partial z} + \frac{\partial \vec{z}}{\partial y} \right) \quad (\text{A.2.2})$$

$$\text{Strain for } \epsilon_{xz} : \epsilon_{xz} = \frac{1}{2} \left(\frac{\partial \vec{x}}{\partial z} + \frac{\partial \vec{z}}{\partial x} \right)$$

A.3 Collapse of a cylindrical hole

There is no deformation in x-direction. It means, $\dot{\epsilon}_{xx} = \lambda \cdot \sigma'_{xx} = 0$. By adding all the stresses of Fig. 2.10 (right) (eq. A.3.1), which are in equilibrium, playing on a part of the wall of a cylindrical hole, it is possible to put in relation σ_{rr} and σ (see Chapter 12 of Hooke (2005) for more details).

$$\sigma_{rr} \cdot (r \cdot d\theta) - \left(\sigma_{rr} + \frac{d\sigma_{rr}}{dr} dr \right) \cdot (r + dr)d\theta + 2 \cdot \sigma_{\theta\theta} \cdot dr \cdot \frac{d\theta}{2} = 0 \quad (\text{A.3.1})$$

$$\Leftrightarrow \sigma_{rr} \cdot r \cdot d\theta - \sigma_{rr} \cdot (r + dr) \cdot d\theta - \frac{d\sigma_{rr}}{dr} dr \cdot (r + dr) \cdot d\theta + 2 \cdot \sigma_{\theta\theta} \cdot dr \cdot \frac{d\theta}{2} = 0$$

$$\Leftrightarrow -\sigma_{rr} - \frac{d\sigma_{rr}}{dr} \cdot r - d\sigma_{rr} + \sigma_{\theta\theta} = 0$$

The term $d\sigma_{rr}$ could be negligible and the equation (A.3.1) can be written as :

$$\frac{d\sigma_{rr}}{dr} \cdot r + \sigma_{rr} - \sigma_{\theta\theta} = 0 \quad (\text{A.3.2})$$

The effective stress σ is defined by the following equation (Hooke, 2005, page 317):

$$\text{Effective stress : } \sigma = \frac{1}{2} |\sigma_{rr} - \sigma_{\theta\theta}| \quad (\text{A.3.3})$$

The equation (A.3.3) could be inserted in the equation (A.3.2).

$$\frac{d\sigma_{rr}}{dr} + 2 \cdot \frac{\sigma}{r} = 0$$

$$\iff d\sigma_{rr} = -2 \cdot \frac{\sigma}{r} dr \quad (\text{A.3.4})$$

For a radius $r \geq a$, the stress is σ_{rr} .

$$\int_0^{\sigma_{rr}} d\sigma_{rr} = \sigma_{rr} = \int_r^\infty \frac{2\sigma}{r} dr \quad (\text{A.3.5})$$

Since r and σ are related, it is necessary to express r in terms of σ . It will be done with the help of the velocity field. Due to the condition of the incompressibility of ice, the mass flux through a cylinder of radius r with a velocity u should be the same as a cylinder of radius $r+dr$ with a velocity $u + \frac{\partial u}{\partial r} dr$ (eq. A.3.6) (Fig. A.1). The velocity is directed to the center of the hole (eq. A.3.7) (Hooke, 2005).

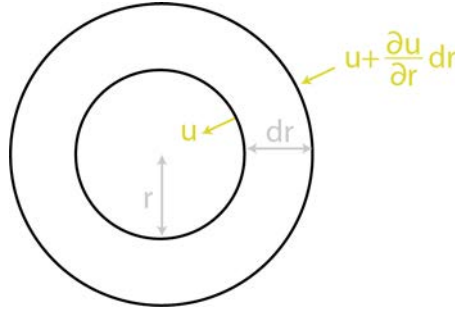


Figure A.1 – Representation of the velocity u in a cylindrical hole (adapted from Hooke (2005, Fig. 12.3, page 318))

$$2 \cdot \pi \cdot r \cdot u = 2 \cdot \pi \cdot (r + dr) \left(u + \frac{du}{dr} \cdot dr \right) \quad (\text{A.3.6})$$

$$0 = r \cdot \frac{du}{dr} + u + \frac{du}{dr} \cdot dr \iff -\frac{u}{r} = \frac{du}{dr} \iff \frac{du}{u} = \frac{dr}{r} \iff \ln(u) = -\ln(r) + \ln(c)$$

$$u = -\frac{c}{r} \quad (\text{A.3.7})$$

The strain rate is defined by the following relation (Hooke, 2005):

$$\dot{\epsilon}_{\theta\theta} = \dot{\epsilon}_{rr} = \frac{u}{r} \quad (\text{A.3.8})$$

The equation (A.3.7) is inserted in the equation (A.3.8). This relation gives the effective strain rate $\dot{\epsilon}$ (eq. A.3.9) (Hooke, 2005).

$$\dot{\epsilon} = \frac{c}{r^2} = f(\sigma) \quad (\text{A.3.9})$$

By deriving $f(\sigma)$, the following relation is obtained (Hooke, 2005):

$$\frac{df(\sigma)}{d\sigma} = \frac{d\left(\frac{c}{r^2}\right)}{dr} \frac{dr}{d\sigma} = -\frac{2c}{r^3} \frac{dr}{d\sigma} = -\frac{2}{r} \frac{c}{r^2} \frac{dr}{d\sigma} = -\frac{2}{r} \cdot f(\sigma) \frac{dr}{d\sigma} \quad (\text{A.3.10})$$

$$-\frac{df(\sigma)}{f(\sigma)} \frac{r}{2} = dr \quad (\text{A.3.11})$$

The equation (A.3.11) is inserted in equation (A.3.5) (Hooke, 2005).

$$\sigma_{rr} = - \int \frac{2 \cdot \sigma}{r} \frac{r}{2} \frac{df(\sigma)}{f(\sigma)} = - \int \frac{\sigma}{f(\sigma)} \cdot df(\sigma) = - \int \frac{\sigma}{\left(\frac{\sigma}{B}\right)^n} \frac{n \cdot \sigma^{n-1}}{B^n} \cdot d\sigma = \int n \cdot d\sigma \quad (\text{A.3.12})$$

$$\sigma_{rr} = \int_0^\sigma n \cdot d\sigma = n \cdot \sigma \quad (\text{A.3.13})$$

For the closure of the gallery hole, the deviatoric stress $\sigma'_{rr(r=a)}$ is necessary (Hooke, 2005).

$$\dot{\epsilon}_{rr(r=a)} = \frac{\sigma^{n-1}}{B^n} \cdot \sigma'_{rr(r=a)} = \frac{\left(\frac{P_n}{n}\right)^{n-1}}{B^n} \cdot \frac{P_n}{n} \quad (\text{A.3.14})$$

The strain rate $\dot{\epsilon}_{rr(r=a)}$ is defined as (Hooke, 2005):

$$\dot{\epsilon}_{rr(r=a)} = -\frac{u_a}{a} \quad (\text{A.3.15})$$

Appendix B

Study site

B.1 Particularity of the Jungfraujoch

The crevasses formation (Haefeli, 1953, page 2; Haefeli & Brentani, 1954a, page 395; Haefeli & Brentani, 1954b, page 3) and the observed deformation in the ice tunnels can be explained with the distribution of the different stresses existing in the ice cap. A compressive stress σ_z is acting in the vertical direction. A compressive stress σ_y is acting in the horizontal direction, which means along the main tunnel. A tensile stress σ_x is acting in the horizontal direction, which means perpendicular to the main gallery (Haefeli, 1953, page 2) (Fig. B.1). The formation of crevasses, direction east-west, due to stress conditions, can reach a depth from 25m to 33m in the central part of the ice cap. The hydrostatic pressure applied on the walls of the crevasses due to meltwater slowly enlarges the crevasses (Haefeli & Schnitter, 1954, page 4). On 08.02.1953 at 3 a.m., a water-filled crevasse frees water at $0^\circ C$ in the transversal tunnel Q120 at a distance of 13.4m of the main gallery. The flow is 5-6l/minute. At 3h15 p.m., the water flux increases. The hole has a diameter of 10cm. The air temperature in the ice tunnel is $-3^\circ C$. The outside air temperature is $-31^\circ C$ and the ice temperature varies between $-3^\circ C$ and $-2^\circ C$ (Haefeli & Brentani, 1954a, page 395, (1954b, page 3)).

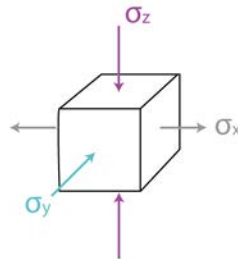


Figure B.1 – Applied stresses (σ_x , σ_y and σ_z) in the three directions (resp. x-, y- and z-direction) in the ice cap of the Jungfraujoch (adapted from Haefeli (1953: Appendix Figure 3b))

The crevasse S2 lies far from 40m of the main tunnel to its north and is water-filled (Fig. 3.4, B.3, B.4, B.5). The volume of water corresponds to 8'000 or 10'000 m^3 . The crevasse S2 communicates with the crevasse S3. The crevasse S3 lies far from 80m of the main tunnel to its north (Fig. 3.4, B.4, B.5). Between the crevasses S2 and S3, two smaller crevasses were observed (Haefeli & Brentani, 1954a, page 395, 1954b, page 3) (Fig. B.4, B.5). The southern wall of the crevasse S3 (position hm 0.72) deforms a lot in 1955 (Haefeli, 1956, page 37). The crevasses are not visible since the surface and do not reach the bedrock. The crevasse S1 lies 1.5m above the top of the tunnel and is water-filled (Fig. 3.4, 3.5, B.3, B.6). It is a dangerous crevasse for the infrastructure due to water invasion. This crevasse is 50m long and has a maximal depth of 10m. The deeper height was 33m under the firn surface. All the crevasses cited above were water-filled and have been drained (Haefeli & Brentani, 1954a, page 395).

The observed blue bands are the freezing of the meltwater filling the crevasses (Fig. B.3, B.5). These blue bands have an obtuse or perpendicular angle to the ice structure (Fig. 3.5, B.3, B.5), which is the primary layer (Haefeli & Brentani, 1954a, page 395, 1954b, page 4). The ice crystals in

the blue bands are coarsely crystalline and limpid. The ice crystals in the ice are finely crystalline and bubble-rich. The observed ice grain diameter of blue bands varies between 5 and 12cm due to the slow process of freezing (Haefeli & Brentani, 1954a, page 400, 1954b, page 4). The primary layer corresponds to the metamorphose of the firn layer. The primary layer follows the morphology of the bedrock. This morphology of the primary layer is more visible at the entrance of the main tunnel (position hm 0.30, which is in the compression zone) than the end of the tunnel (position hm 1.60, which is the tension zone where the contact between the ice and the bedrock is less good) (Haefeli & Brentani, 1954a, page 395).

On 06.02.2020, during the temperature measurement, a water-filled crevasse (north of the ice gallery) was emptying by the hole for the temperature sensors. The emptying happened for some hours. According to Martin Lüthi, the discharge may be of approximately 6.5 L/s.



Figure B.2 – Emptying of a water-filled crevasse on 06.02.2020 (photo taken by S. Morard)

B.2 Description of the infrastructure

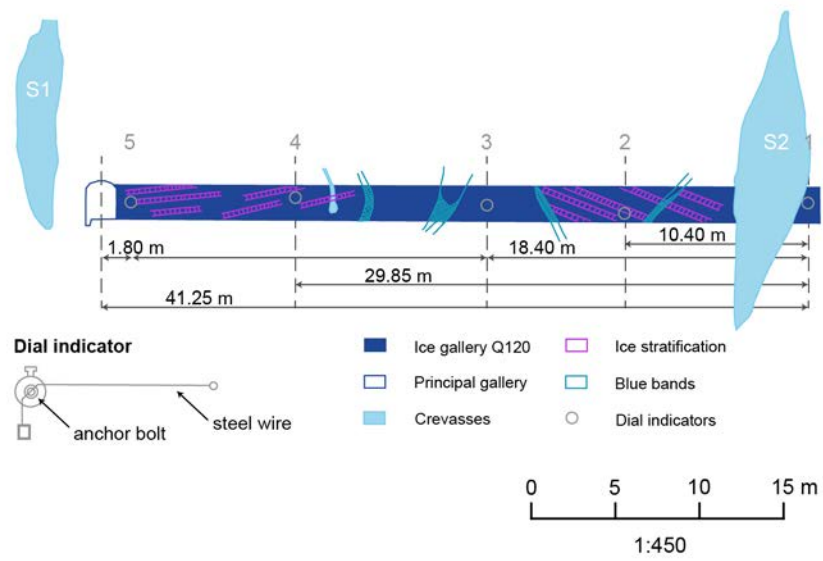


Figure B.3 – Schema of the transversal tunnel Q120 (adapted from Haefeli & Schnitter (1954, Appendix Figure 6))

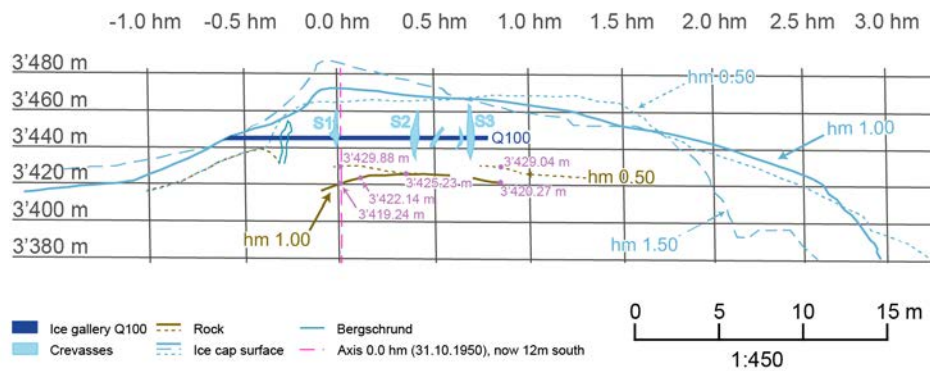


Figure B.4 – Schema of the transversal tunnel Q120 in the ice cap (adapted from Haefeli & Schnitter (1954, Appendix Figure 3))

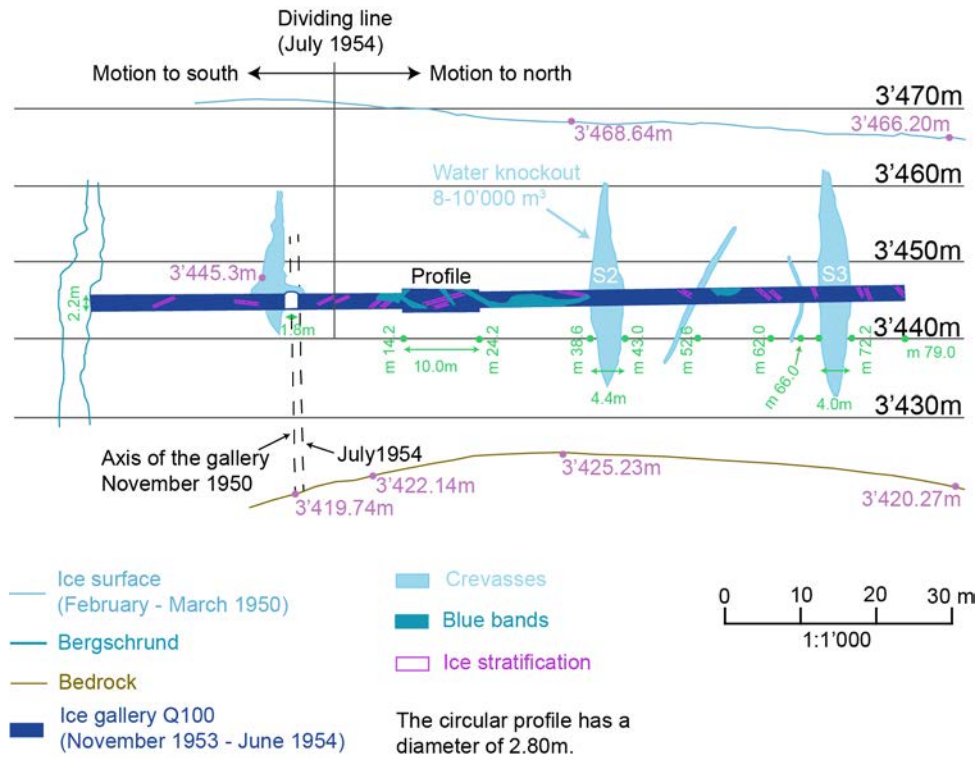


Figure B.5 – Schema of the transversal tunnel Q100 (adapted from Haefeli & Schnitter (1954, Appendix Figure 7))

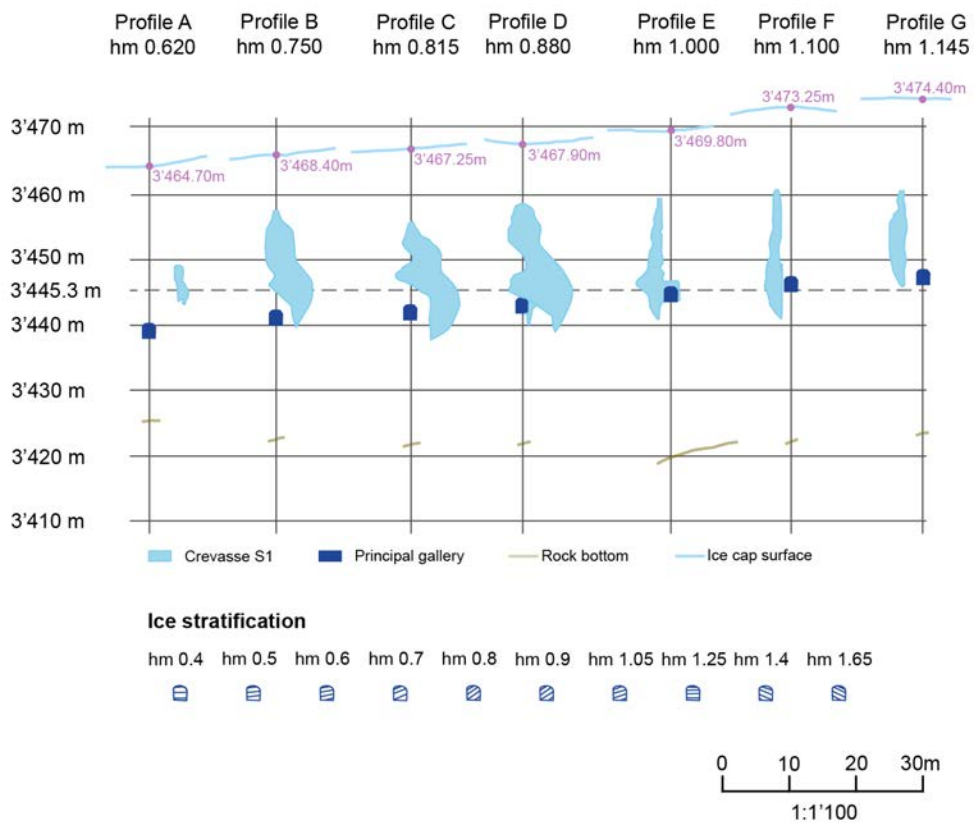


Figure B.6 – Crevasses (adapted from Haefeli & Schnitter (1954, Appendix figure 4))

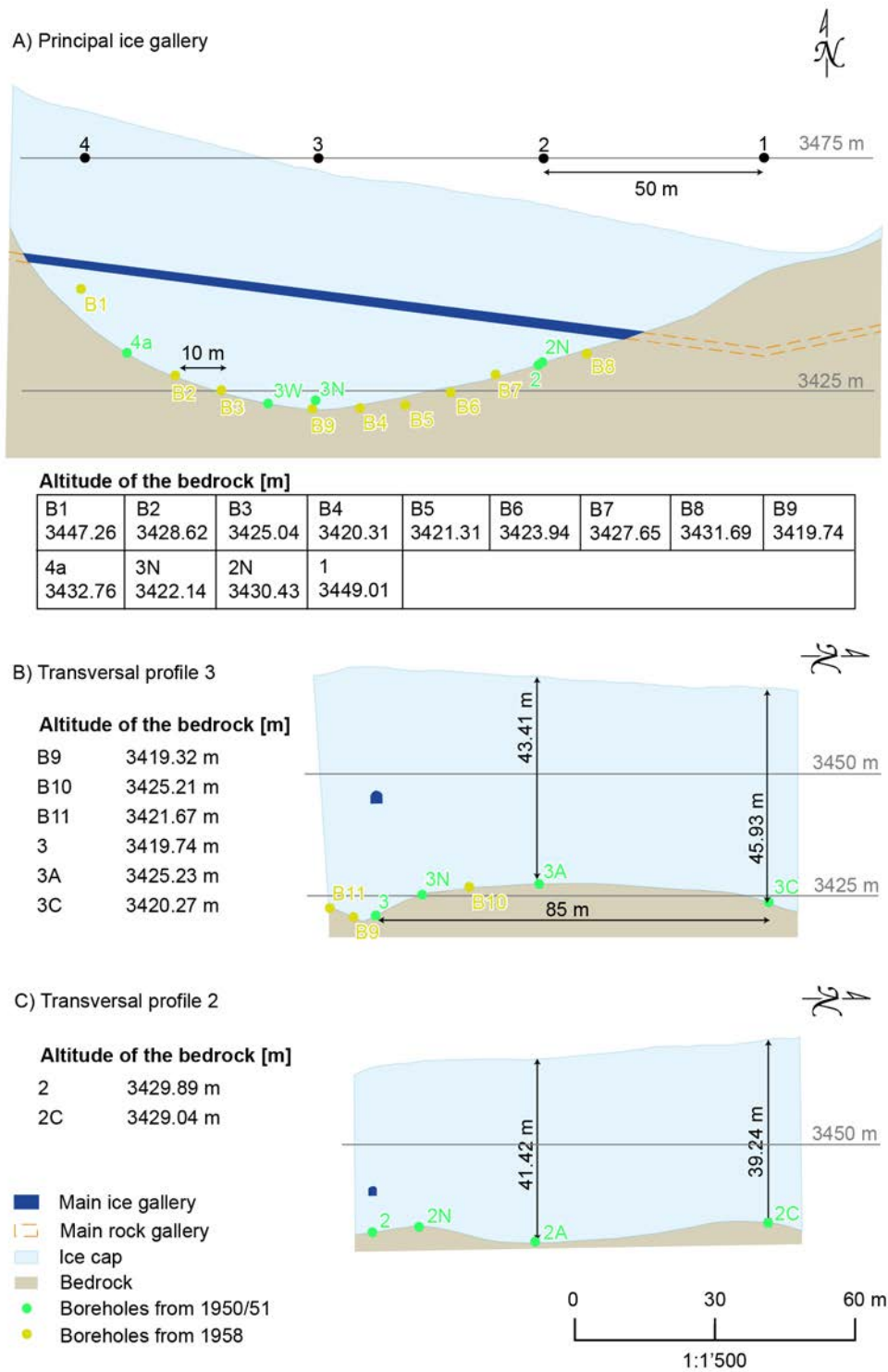


Figure B.7 – Position of the different boreholes. In the figure A), the borehole B9 situates 4.9m south of the borehole 3. The bedrock shape for the three figures dates from 1950/51. The boreholes B1 to B11 reach the bedrock. (adapted from Vöggtli (1959, Appendix Figure 2 and 3))

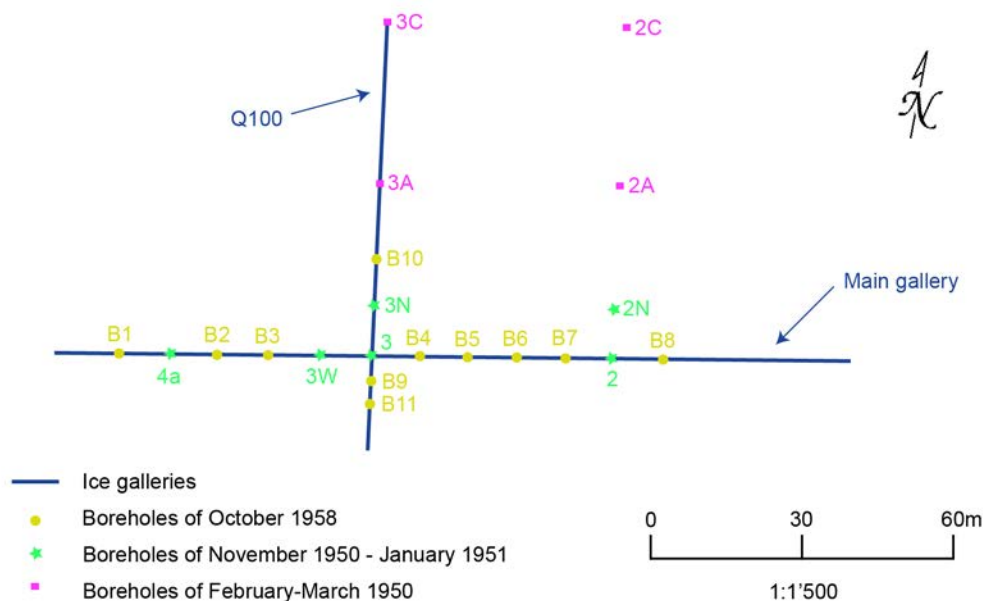


Figure B.8 – Location of the boreholes B1 to B10 (adapted from Vögtli(1959, Fig. 1))

B.3 Greenland

The ice cap of Greenland is 60-70 times thicker than the ice cap of the Jungfrauoch (Haefeli & Brentani, 1954a, page 408, 1954b, page 16). The width is 3000 times bigger (Haefeli & Brentani, 1954b, page 16). The temperature in central Greenland is colder (Haefeli & Brentani, 1954a, page 408, 1954b, page 16). It noted cold temperature but small shear stress. Due to the high seismic waves (approx. 3800 m/s) realized by the Expédition Polaires Françaises (Missions Paul-Emile Victor), J. Holtzecherer hypothesized that the central ice cap of Groenland should be cold until the rock bottom (Haefeli & Brentani, 1954b, page 16). G. Robin hypothesized the temperature at the rock bottom with the hypothesis that the annual accumulation is 34cm. So, the temperature at the rock bottom may be $-2^{\circ}C$ under 3'000m of ice cover (Haefeli & Brentani, 1954b, p. 17). During summer 1950, the third campaign (B.9) in Greenland was organised, where they measured the ice density and the temperature at different depths at the *Station Centrale (mile 200)*. The *Station Centrale* locates at the position $70^{\circ}55'03''N / -40^{\circ}38'22''E$. The well had a diameter of 80cm and reached a depth of 30m. The temperature had been measured for ten days. Temperatures vary between $-29^{\circ}C$ and $-16^{\circ}C$. The density varies between $0.51g/cm^3$ and $0.7g/cm^3$ (Expéditions Polaires Françaises, 1950). On Fig. B.9, it seems to have a gallery at depth 30m. However, the reports do not mention it.

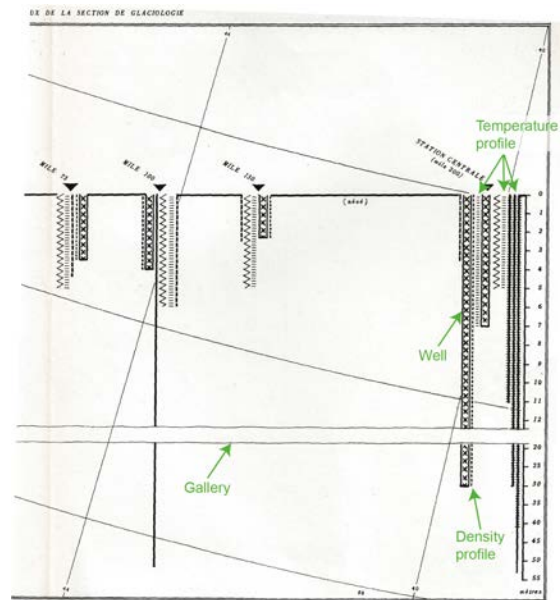


Figure B.9 – Measurements at the Station Centrale (Expéditions Polaires Françaises, 1950, page 84)

Appendix C

Methodology

```
1 // define a tunnel by hand,
2
3 x0 = 0; x1 = 1;
4 y0 = -30; y1 = 30;
5 z0 = -20; z1 = 28;
6
7 // radius of the hole
8 rhole = 1.45;
9
10 Lc1 = 2; // length scale
11 Lc2 = 0.2; // length scale
12
13 // bottom
14 Point(1) = {x0, y0, z0, Lc1};
15 Point(2) = {x0, y1, z0, Lc1};
16
17 // top
18 Point(3) = {x0, y0, z1, Lc1};
19 Point(4) = {x0, y1, z1, Lc1};
20
21 Line(1) = {1, 2};
22 Line(2) = {2, 4};
23 Line(3) = {4, 3};
24 Line(4) = {3, 1};
25
26 // circle in center (x0,0,0) of radius rhole
27 Point(5) = {x0, 0, 0, Lc2};
28 Point(6) = {x0, rhole, 0, Lc2}; // right
29 Point(7) = {x0, 0, rhole, Lc2}; // top
30 Point(8) = {x0, -rhole, 0, Lc2};
31 Point(9) = {x0, 0, -rhole, Lc2};
32
33 Circle(5) = {6, 5, 7};
34 Circle(6) = {7, 5, 8};
35 Circle(7) = {8, 5, 9};
36 Circle(8) = {9, 5, 6};
37
38 Curve Loop(9) = {1, 2, 3, 4}; // square
39 Curve Loop(10) = {5, 6, 7, 8}; // circle
40 Plane Surface(11) = {9, 10};
41 Surface Loop(12) = {11};
42
43 num[] = Extrude {x1, 0, 0} { Surface{11}; };
44
45 Physical Volume("glacierice") = {num[1]};
46 Physical Surface("front") = {num[0]};
47 Physical Surface("bottom") = {num[2]};
48 Physical Surface("right") = {num[3]};
49 Physical Surface("back") = {11};
50 Physical Surface("left") = {num[5]};
51 Physical Surface("top") = {num[4]};
```

Figure C.1 – Code of the mesh, written by Martin Lüthi, for the circular profile K_1 with a width of 60m.

```

1  [GlobalParams]
2  displacements = 'disp_x disp_y disp_z'
3  []
4
5  [Mesh]
6  displacements = 'disp_x disp_y disp_z'
7  type = FileMesh
8  file = K1_50m.msh
9  second_order = true
10 boundary_id = '2 3 4 5 6 7'
11 boundary_name = 'front bottom right back left top'
12 []
13
14 [Modules/TensorMechanics/Master]
15 [./all]
16 strain = FINITE
17 incremental = true
18 add_variables = true
19 generate_output = 'stress_yy strain_yy stress_zz strain_zz'
20 eigenstrain_names = ini_stress
21 use_displaced_mesh = true
22 [./]
23 []
24
25 [Functions]
26 [./rhogf]
27 type = ParsedFunction
28 value = '-0.008338'
29 [./]
30
31 [./weight]
32 type = ParsedFunction
33 value = '-0.008338*(28-z)'
34 [./]
35 []
36
37 [Kernels]
38 [./gravity_y]
39 type = Gravity
40 variable = disp_z
41 value = 1
42 function = rhogf
43 [./]
44 []
45
46 [BCs]
47
48 [./velx]
49 type = PresetBC
50 variable = disp_x
51 boundary = 'bottom front back'
52 value = 0
53 [./]
54 [./vely]
55 type = PresetBC
56 variable = disp_y
57 boundary = 'bottom left right'
58 value = 0
59 [./]
60 [./velz]
61 type = PresetBC
62 variable = disp_z
63 boundary = bottom
64 value = 0
65 [./]
66 []
67
68 [Materials]
69 [./elasticity_tensor]
70 type = ComputeIsotropicElasticityTensor
71 youngs_modulus = 8700
72 poissons_ratio = 0.31
73 [./]
74 [./creep_plas]
75 type = ComputeMultipleInelasticStress
76 tangent_operator = elastic
77 inelastic_models = 'creep'
78 max_iterations = 50
79 absolute_tolerance = 1e-04
80 combined_inelastic_strain_weights = '1'
81 [./]
82 [./creep]
83 type = PowerLawCreepStressUpdate
84 coefficient = 50
85 n_exponent = 3
86 m_exponent = 0
87 activation_energy = 0
88 [./]
89 [./density_ice]
90 type = GenericConstantMaterial
91 prop_names = density
92 prop_values = 1
93 [./]
94
95 [./strain_from_initial_stress]
96 type = ComputeEigenstrainFromInitialStress
97 initial_stress = '0 0 0 0 0 0 weight'
98 eigenstrain_name = ini_stress
99 [./]
100 []
101
102
103 [Executioner]
104 type = Transient
105
106 l_max_its = 50
107 l_tol = 1e-7
108 nl_max_its = 20
109 nl_rel_tol = 1e-7
110 nl_abs_tol = 1e-5
111
112 dtmin = 0.001
113 dtmax = 0.1
114 end_time = 1
115 [./TimeStepper]
116 type = ConstantDT
117 dt = 0.01
118 [./]
119 []

```

Figure C.2 – Part of the model used for the results of Chapter 6.2. The block PostProcessor is missing in the script here.

```
1 [BCs]
2
3 [./velx]
4 type = PresetBC
5 variable = disp_x
6 boundary = 'bottom front back'
7 value = 0
8 [../]
9 [./vely]
10 type = PresetBC
11 variable = disp_y
12 boundary = 'bottom'
13 value = 0
14 [../]
15
16 [./vely_1]
17 type = FunctionDirichletBC
18 variable = disp_y
19 boundary = 'left'
20 function = '-0.1*t'
21 [../]
22
23 [./vely_2]
24 type = FunctionDirichletBC
25 variable = disp_y
26 boundary = 'right'
27 function = '0.1*t'
28 [../]
29
30 [./velz]
31 type = PresetBC
32 variable = disp_z
33 boundary = bottom
34 value = 0
35 [../]
36 []
```

Figure C.3 – Part modified of Fig. C.2 for the results of Chapter 6.3.

```

1 [Mesh]
2 type = AnnularMesh
3 nr = 10
4 nt = 50
5 rmin = 0
6 rmax = 0.0713
7 dmin = 0
8 dmax = 360
9 growth_r = 1
10 []
11 [MeshModifiers]
12 [/extrude]
13 type = MeshExtruder
14 num_layers = 17
15 extrusion_vector = '0 0 0.17'
16 bottom_sideset = 'bottom'
17 top_sideset = 'top'
18 [-/]
19 []
20 [Variables]
21 [/disp_x]
22 order = FIRST
23 family = LAGRANGE
24 [-/]
25 [/disp_y]
26 order = FIRST
27 family = LAGRANGE
28 [-/]
29 [/disp_z]
30 order = FIRST
31 family = LAGRANGE
32 [-/]
33 []
34 [AuxVariables]
35 [/stress_xx]
36 order = CONSTANT
37 family = MONOMIAL
38 [-/]
39 [/strain_xx]
40 order = CONSTANT
41 family = MONOMIAL
42 [-/]
43 [/creep_strain_xx]
44 order = CONSTANT
45 family = MONOMIAL
46 [-/]
47 []
48 []
49 [Kernels]
50 [/gravity_z]
51 type = Gravity
52 variable = disp_z
53 value = -9.81
54 [-/]
55 [/TensorMechanics]
56 displacements = 'disp_x disp_y disp_z'
57 use_displaced_mesh = true
58 [-/]
59 []
60 [AuxKernels]
61 [/stress_xx]
62 type = RankTwoAux
63 variable = stress_xx
64 rank_two_tensor = stress
65 index_j = 0
66 index_i = 0
67 execute_on = timestep_end
68 [-/]
69 [/strain_xx]
70 type = RankTwoAux
71 variable = strain_xx
72 rank_two_tensor = total_strain
73 index_j = 0
74 index_i = 0
75 execute_on = timestep_end
76 [-/]
77 [/creep_strain_xx]
78 type = RankTwoAux
79 variable = creep_strain_xx
80 rank_two_tensor = creep_strain
81 index_j = 0
82 index_i = 0
83 execute_on = timestep_end
84 [-/]
85 []
86 [BCs]
87 [/symm]
88 type = PresetBC
89 variable = disp_y
90 boundary = bottom
91 value = 0
92 [-/]
93 [/symm]
94 type = PresetBC
95 variable = disp_x
96 boundary = bottom
97 value = 0
98 [-/]
99 [/symm]
100 type = PresetBC
101 variable = disp_z
102 boundary = bottom
103 value = 0
104 [-/]
105 [/axial_load]
106 type = NeumannBC
107 variable = disp_z
108 boundary = top
109 value = -9.81e4
110 [-/]
111 []
112 [Materials]
113 [/kelvin_voigt]
114 type = GeneralizedKelvinVoigtModel
115 creep_modulus = '9.06e11 0.81e8 1.02e8'
116 creep_viscosity = '1 3 12 2 2'
117 poisson_ratio = 0.31
118 young_modulus = 8.7e9
119 [-/]
120 [/stress]
121 type = ComputeMultipleInelasticStress
122 inelastic_models = 'creep'
123 [-/]
124 [/creep]
125 type = LinearViscoelasticStressUpdate
126 [-/]
127 [/strain]
128 type = ComputeFiniteStrain
129 #type = ComputeIncrementalSmallStrain
130 displacements = 'disp_x disp_y disp_z'
131 [-/]
132 [/density_ice]
133 type = GenericConstantMaterial
134 prop_names = density
135 prop_values = 850 #kg/m^3
136 [-/]
137 []
138 [UserObjects]
139 [/update]
140 type = LinearViscoelasticityManager
141 viscoelastic_model = kelvin_voigt
142 [-/]
143 []
144 [Postprocessors]
145 [/stress_xx]
146 type = ElementAverageValue
147 variable = stress_xx
148 block = 'ANY_BLOCK_ID 0'
149 [-/]
150 [/strain_xx]
151 type = ElementAverageValue
152 variable = strain_xx
153 block = 'ANY_BLOCK_ID 0'
154 [-/]
155 [/creep_strain_xx]
156 type = ElementAverageValue
157 variable = creep_strain_xx
158 block = 'ANY_BLOCK_ID 0'
159 [-/]
160 []
161 [Preconditioning]
162 [/smp]
163 type = SMP
164 full = true
165 [-/]
166 []
167 [Executioner]
168 type = Transient
169 [-/]
170 l_max_its=50
171 l_tol = 1e-8
172 nl_max_its = 20
173 nl_rel_tol = 1e-8
174 nl_abs_tol = 1e-6
175 [-/]
176 dtmin = 0.01
177 dtmax = 10
178 end_time = 1000
179 [/TimeStepper]
180 type = LogConstantDT
181 first_dt = 0.01
182 log_dt = 100.0
183 [-/]
184 []
185 [Outputs]
186 file_base = v1
187 exodus = true
188 csv = true
189 [-/]
190 []

```

Figure C.4 – Model used for the ice experiment.

C.1 Profile K_3

Start point	End point	Distance	Start point	End point	Distance
[–]	[–]	[mm]	[–]	[–]	[mm]
04.12.19	04.12.19	04.12.19	06.02.20	06.02.20	06.02.20
2	6	2682	1	3	2383
1	6	2081	1	4	2451
7	6	1437	1	5	2573
7	5	2286	1	6	2058
1	5	2611	2	4	1671
2	5	2546	2	5	2526
2	6	2683	2	6	2660
1	4	2491	6	3	2433
7	4	2646	6	4	1844
6	4	1862	6	5	970
2	4	1691	7	2	2464
2	3	1117	7	3	2845
1	3	2418	7	4	2609
7	3	2874	7	5	2245
6	3	2450	7	6	1418

Table C.1 – Profile K_3 : Mean measurements of distance from 04.12.19 to 06.02.20

C.2 Profile K_4

Start point	End point	Distance	Start point	End point	Distance
[-]	[-]	[mm]	[-]	[-]	[mm]
04.12.19	04.12.19	04.12.19	06.02.20	06.02.20	06.02.20
7	6	1484	1	4	2660
2	6	2963	1	5	2703
2	5	2864	2	4	1993
1	5	2719	2	6	2962
7	5	2355	3	4	1297
7	4	2826	3	5	2503
1	4	2676	6	3	2936
6	4	2060	6	4	2053
2	4	2005	7	3	3088
7	3	3097	7	4	2810
6	3	2939	7	5	2340
2	3	1015	7	6	1478
6	2	2964	2	5	2865
3	6	2943			

Table C.2 – Profile K_4 : Mean measurements of distance from 04.12.19 to 06.02.20

Appendix D

Data

D.1 Profile K_1

D.1.1 Positions and displacements of the survey points

Date	20.02.1951		13.09.1951		08.01.1953	
Point	X_1	Y_1	X_2	Y_2	X_3	Y_3
[–]	[mm]	[mm]	[mm]	[mm]	[mm]	[mm]
1	315	-970	326	-915	371	-697
2	0	0	30	24	55	21
3	584	1055	589	981	565	791
4	1592	1283	1595	1209	1637	1034
5	2533	857	2512	827	2505	765
6	2947	22	2898	5	2888	20
7	2559	-989	2566	-911	2587	-697
8	1562	-1307	1570	-1251	1606	-987

Table D.1 – Coordinates of the survey points of the circular profile K_1 at three different time periods (20.02.1951, 13.09.1951, 08.01.1953).

The three following tables describe the displacements and the velocity of displacement of each survey points from 20.02.1951 to 13.09.1951 (205 days) (Table D.2), from 13.09.1951 to 08.01.1953 (483 days) (Table D.3), from 20.02.1951 to 08.01.1953 (688 days) (Table D.4).

Point	ΔX_{12}	ΔY_{12}	D	$v_{x_{12}}$	$v_{y_{12}}$	v
[–]	[mm]	[mm]	[mm]	[mm/day]	[mm/day]	[mm/day]
1	-11	-55	56.1	-0.05	-0.27	0.27
2	-30	-24	38.4	-0.15	-0.12	0.19
3	-5	74	74.2	-0.02	0.36	0.36
4	-3	74	74.1	-0.01	0.36	0.36
5	21	30	36.6	0.10	0.15	0.18
6	49	17	51.9	0.24	0.08	0.25
7	-7	-78	78.3	-0.03	-0.38	0.38
8	-8	-56	56.6	-0.04	-0.27	0.28

Table D.2 – Profile K_1 : Displacements, velocity of displacement of each survey points from 20.02.1951 to 13.09.1951.

Point	ΔX_{23}	ΔY_{23}	D	$v_{x_{23}}$	$v_{y_{23}}$	v
[—]	[mm]	[mm]	[mm]	[mm/day]	[mm/day]	[mm/day]
1	-45	-218	222.6	-0.09	-0.45	0.46
2	-25	3	25.2	-0.05	0.01	0.05
3	24	190	191.5	0.05	0.39	0.40
4	-42	175	180.0	-0.09	0.36	0.37
5	7	62	62.4	0.01	0.13	0.13
6	10	-15	18.0	0.02	-0.03	0.04
7	-21	-214	215.0	-0.04	-0.44	0.45
8	-36	-264	266.4	-0.07	-0.55	0.55

Table D.3 – Profile K_1 : Displacements, velocity of displacement, strain and strain rate of each survey points from 13.09.1951 to 08.01.1953.

Point	ΔX_{13}	ΔY_{13}	D	$v_{x_{13}}$	$v_{y_{13}}$	v
[—]	[mm]	[mm]	[mm]	[mm/day]	[mm/day]	[mm/day]
1	-56	-273	278.7	-0.08	-0.40	0.41
2	-55	-21	58.9	-0.08	-0.30	0.09
3	19	264	264.7	0.03	0.38	0.38
4	-45	249	253.0	-0.07	0.36	0.37
5	28	92	96.2	0.04	0.13	0.14
6	59	2	59.0	0.09	0.003	0.09
7	-28	-292	293.3	-0.04	-0.42	0.43
8	-44	-320	323.0	-0.06	-0.47	0.47

Table D.4 – Profile K_1 : Displacements, velocity of displacement, strain and strain rate of each survey points from 20.02.1951 to 08.01.1953.

D.1.2 Vertical deformation

The initial vertical deformation between the survey points 3 and 1 is 2042.8mm (Table D.5). In 688 days, the length shortens of 413.6 mm, approximately 26.5% of its initial length. The mean strain rate is $-26.5\%/688 \text{ days} = -0.04\%/day = -14.1\%/year$.

The initial vertical deformation between the survey points 4 and 8 is 2590.2 mm (Table D.5). The length shortens of 568.9mm, approximately 22.0% of its initial length. The mean strain rate is $-22.0\%/688 \text{ days} = -0.03\%/day = -11.7\%/year$. There are differences between the measured and digitized vertical deformations between the survey points 4 and 8. The differences are 13.8mm for 20.02.1951, 38.1mm for 13.09.1951, and 48.8mm for 08.01.1953. These differences come from the georeferencing of the map and the accuracy of the coordinates of each survey point.

The initial length between the survey points 5 and 7 is 1846.2 mm (Table D.5). The length shortens of 381.9 mm, nearly 20.7% of its initial length. The mean strain rate is $-20.7\%/688 \text{ days} = -0.03\%/day = -11.0\%/year$.

D.1.3 Horizontal deformation

The initial horizontal deformation between the survey points 3 and 5 is 1959.0 mm (table D.6). In 688 days, the length shortens of 18.9mm, approximately 1.0% of its initial length. The mean strain rate is $-1.0\%/688 \text{ days} = -0.001\%/day = -0.5\%/year$.

The initial horizontal deformation between the survey points 2 and 6 is 2947.1 mm (table D.6). In 688 days, the length shortens of 114.1 mm, approximately 3.9% of its initial length. The mean strain rate is $-3.9\%/688 \text{ days} = -0.006\%/day = -2.1\%/year$. There are differences between the measured and digitized horizontal deformations between the survey points 2 and 6. The differences are 16.1 mm for 20.02.1951, 121 mm for 13.09.1951, and 40 mm for 08.01.1953. These differences come from the georeferencing of the map and the accuracy of the coordinates of each survey point.

The initial horizontal length between the survey points 1 and 7 is 2244.1 mm (table D.6). In 688 days, the length shortens of 28.1 mm, approximately 1.3% of its initial length. The mean strain rate is $-1.3\%/688 \text{ days} = -0.002\%/day = -0.7\%/year$.

i	T	ΔT	D_{31}	ΔD_{31}	$\Delta D_{31,cum}$	δD_{31}	$\delta \dot{D}_{31}$
[-]	[-]	[days]	[mm]	[mm]	[mm]	[%]	[%/day]
1	20.02.51	0	2042.8	0.0	0.0	0.0	0.00
2	13.09.51	205	1914.2	-128.6	-128.6	-6.3	-0.03
3	08.01.1953	483	1500.6	-413.6	-542.2	-26.5	-0.05

i	T	ΔT	D_{48}	ΔD_{48}	$\Delta D_{48,cum}$	δD_{48}	$\delta \dot{D}_{48}$
[-]	[-]	[days]	[mm]	[mm]	[mm]	[%]	[%/day]
1	20.02.51	0	2590.2	0.0	0.0	0.0	0.00
2	13.09.51	205	2460.1	-130.0	-130.0	-5.0	-0.02
3	08.01.53	483	2021.2	-483.9	-568.9	-22.0	-0.05

i	T	ΔT	D_{57}	ΔD_{57}	$\Delta D_{57,cum}$	δD_{57}	$\delta \dot{D}_{57}$
[-]	[-]	[days]	[mm]	[mm]	[mm]	[%]	[%/day]
1	20.02.51	0	1846.2	0.0	0.0	0.0	0.00
2	13.09.51	205	1738.8	-107.3	-107.3	-5.8	-0.03
3	08.01.51	483	1464.3	-274.5	-381.9	-20.7	-0.04

Table D.5 – Profile K_1 : Vertical deformation determined from the digitization from 20.02.1951 to 08.01.1953

i	T	ΔT	D_{35}	ΔD_{35}	$\Delta D_{35,cum}$	δD_{35}	$\delta \dot{D}_{35}$
[-]	[-]	[days]	[mm]	[mm]	[mm]	[%]	[%/day]
1	20.02.51	0	1959.0	0.0	0.0	0.0	0.00
2	13.09.51	205	1929.2	-29.9	-29.9	-1.5	-0.01
3	08.01.1953	483	1940.2	11.0	-18.9	-1.0	-0.002

i	T	ΔT	D_{26}	ΔD_{26}	$\Delta D_{26,cum}$	δD_{26}	$\delta \dot{D}_{26}$
[-]	[-]	[days]	[mm]	[mm]	[mm]	[%]	[%/day]
1	20.02.51	0	2947.1	0.0	0.0	0.0	0.00
2	13.09.51	205	2868.1	-79.0	-79.0	-2.7	-0.01
3	08.01.53	483	2833.0	-35.1	-114.1	-3.9	-0.01

i	T	ΔT	D_{57}	ΔD_{57}	$\Delta D_{57,cum}$	δD_{57}	$\delta \dot{D}_{57}$
[-]	[-]	[days]	[mm]	[mm]	[mm]	[%]	[%/day]
1	20.02.51	0	2244.1	0.0	0.0	0.0	0.00
2	13.09.51	205	2240.0	-4.1	-4.1	-0.2	-0.001
3	08.01.51	483	2216.0	-24.0	-28.1	-1.3	-0.003

Table D.6 – Profile K_1 : Horizontal deformation determined from the digitization from 20.02.1951 to 08.01.1953

D.1.4 Oblique deformation

The initial oblique deformation between the survey points 3 and 7 is 2842.3 mm (table D.7). In 688 days, the length shortens of 331.8 mm, the 11.7% of its initial length. The mean strain rate is $-11.7\%/688 \text{ days} = -0.02\%/day = -6.2\%/year$.

The initial oblique deformation between the survey points 5 and 1 is 2873.6 mm (table D.7). In 688 days, the length shortens of 286.6 mm, 10.0% of its initial length. The mean strain rate is $-10.0\%/688 \text{ days} = -0.01\%/day = -5.3\%/year$.

i	T	ΔT	D_{37}	ΔD_{37}	$\Delta D_{37,cum}$	δD_{37}	$\delta \dot{D}_{37}$
[–]	[–]	[days]	[mm]	[mm]	[mm]	[%]	[%/day]
1	20.02.51	0	2842.3	0.0	0.0	0.0	0.00
2	13.09.51	205	2736.5	-105.8	-105.8	-3.7	-0.02
3	08.01.1953	483	2510.5	-226.0	-331.8	-11.7	-0.024

i	T	ΔT	D_{51}	ΔD_{51}	$\Delta D_{51,cum}$	δD_{51}	$\delta \dot{D}_{51}$
[–]	[–]	[days]	[mm]	[mm]	[mm]	[%]	[%/day]
1	20.02.51	0	2873.6	0.0	0.0	0.0	0.00
2	13.09.51	205	2795.2	-78.4	-78.4	-2.7	-0.01
3	08.01.53	483	2586.8	-208.4	-286.8	-10.0	-0.02

Table D.7 – Profile K_1 : Oblique deformation determined from the digitization from 20.02.1951 to 08.01.1953

D.2 Profile K_2

D.2.1 Positions and displacements of the survey points

Date	29.08.1954		04.01.1954		06.09.1955		07.02.1956	
Point	X_1	Y_1	X_2	Y_2	X_3	Y_3	X_4	Y_4
[–]	[mm]	[mm]	[mm]	[mm]	[mm]	[mm]	[mm]	[mm]
1	-	-	-1116	-1963	-1103	-1964	-1089	-1960
2	1096	-1870	1091	-1866	1072	-1867	1060	-1867
3	1285	-1003	1258	-1006	1232	-1014	1218	-1020
4	1174	-587	1139	-606	1101	-626	1086	633
5	30	70	-22	5	-4	-1	-44	-21
6	-1137	-581	-1150	-572	-1132	-560	-1104	-613
7	-	-	-1307	-1049	-1279	-1046	-1267	-1055
8	-	-	-	-	-121	-2222	-1211	-2213

Table D.8 – Coordinates of the survey points of the circular profile K_2 at four different time periods (29.08.1954, 04.01.1954, 06.09.1955, 07.02.1956).

The following tables describe the displacements and the velocity of each survey points from 29.08.1954 to 04.11.1954 (67 days) (Table D.9), from 04.11.1954 to 06.09.1955 (306 days) (Table D.10), from 06.09.1955 to 07.02.1956 (154 days) (Table D.11) and from 29.08.1954 to 07.02.1956 (527 days) (Table D.12).

Point	ΔX_{12}	ΔY_{12}	D	$v_{x_{12}}$	$v_{y_{12}}$	v
[–]	[mm]	[mm]	[mm]	[mm/day]	[mm/day]	[mm/day]
1	-	-	-	-	-	-
2	5	-4	6.5	0.08	-0.06	0.10
3	27	3	27.1	0.40	0.04	0.40
4	36	19	40.3	0.53	0.28	0.60
5	52	16	54.6	0.78	0.24	0.82
6	13	-9	14.8	0.19	-0.13	0.23
7	-	-	-	-	-	-
8	-	-	-	-	-	-

Table D.9 – Profile K_2 : Displacements and velocity of displacement of each survey points from 29.08.1954 to 04.11.1954.

Point	ΔX_{23}	ΔY_{23}	D	$v_{x_{23}}$	$v_{y_{23}}$	v
[–]	[mm]	[mm]	[mm]	[mm/day]	[mm/day]	[mm/day]
1	-12	-2	12.5	-0.04	0.01	0.04
2	19	1	18.8	0.06	0.01	0.09
3	26	8	27.7	0.09	0.03	0.09
4	38	20	42.8	0.12	0.07	0.14
5	16	55	57.6	0.05	0.18	0.19
6	-18	28	33.1	-0.06	0.09	0.11
7	-28	-3	27.8	-0.09	-0.01	0.09
8	-	-	-	-	-	-

Table D.10 – Profile K_2 : Displacements and velocity of displacement of each survey points from 04.11.1954 to 06.09.1955.

Point	ΔX_{34}	ΔY_{34}	D	$v_{x_{34}}$	$v_{y_{34}}$	v
[–]	[mm]	[mm]	[mm]	[mm/day]	[mm/day]	[mm/day]
1	-15	-4	15.5	-0.10	-0.03	0.10
2	12	0	12.5	0.08	-0.002	0.08
3	14	6	14.9	0.09	0.04	0.22
4	15	7	16.5	0.10	0.05	0.11
5	6	20	20.7	0.04	0.13	0.14
6	-29	14	31.8	0.19	0.09	0.21
7	-13	8	15.3	-0.08	0.06	0.10
8	0	-9	9.1	0.001	-0.06	0.06

Table D.11 – Profile K_2 : Displacements and velocity of displacement of each survey points from 06.09.1955 to 07.02.1956.

Point	ΔX_{14}	ΔY_{14}	D	$v_{x_{14}}$	$v_{y_{14}}$	v
[–]	[mm]	[mm]	[mm]	[mm/day]	[mm/day]	[mm/day]
1	-	-	-	-	-	-
2	36	-3	36.5	0.07	-0.01	0.07
3	67	17	69.1	0.13	0.03	0.13
4	88	46	99.6	0.17	0.09	0.19
5	75	91	117.5	0.14	0.17	0.22
6	-34	33	47.0	-0.06	0.06	0.08
7	-	-	-	-	-	-
8	-	-	-	-	-	-

Table D.12 – Profile K_2 : Displacements and velocity of displacement of each survey points from 29.08.1954 to 07.02.1956.

D.2.2 Vertical deformation

The initial vertical deformation between the survey points 1 and 6 is 1392 (Table D.13). In 460 days, the length shortens of 45 mm, 3.2% of its initial length. The mean strain rate is $-3.2\%/460$ days = $0.007\%/day$ = $2.5\%/year$.

The vertical deformation between the survey points 5 and 8 on 06.09.1955 is 2223 mm (Table D.13). In 154 days, the length shortens of 29mm, 1.3% of its initial length. The mean strain rate is $-1.3\%/154$ days = $-0.008\%/day$ = $-3.1\%/year$. There are differences between the measured and digitized vertical deformations between the survey points 5 and 8. The differences are 12mm for 07.02.1956. These differences come from the georeferencing of the map and the accuracy of the coordinates of every survey point.

The initial vertical deformation between the survey points 3 and 4 is 1261mm (Table D.13). In 460 days, the length shortens of 27 mm, 2.1% of its initial length. The mean strain rate is

$-2.1\%/460 \text{ days} = 0.005\%/day = 1.7\%/year$.

i	T	ΔT	D_{61}	ΔD_{61}	$\Delta D_{61,cum}$	δD_{61}	$\delta \dot{D}_{61}$
[–]	[–]	[days]	[mm]	[mm]	[mm]	[%]	[%/day]
1	29.08.54	0	-	0	0	0	0
2	04.11.54	0	1392	0	0	0	0
3	06.09.55	306	1365	-27	-27	-1.9	-0.006
4	07.02.56	154	1347	-18	-45	-1.3	-0.008
i	T	ΔT	D_{58}	ΔD_{58}	$\Delta D_{58,cum}$	δD_{58}	$\delta \dot{D}_{58}$
1	29.08.54	0	-	0	0	0	0
2	04.11.54	0	-	0	0	0	0
3	06.09.55	306	2223	0	0	0	0
4	07.02.56	154	2194	-29	-29	-1.3	-0.009
i	T	ΔT	D_{57}	ΔD_{57}	$\Delta D_{57,cum}$	δD_{57}	$\delta \dot{D}_{57}$
1	29.08.1954	0	1285	0	0	0	0
2	04.11.1954	0	1261	0	0	0	0
3	06.09.1955	306	1240	-19	-19	-1.5	-0.005
4	07.02.1956	154	1234	-6	-25	-0.6	-0.0004

Table D.13 – Profile K_2 : Vertical deformation determined from the digitisation from 04.11.1954 to 07.02.1956

D.2.3 Horizontal deformation

The initial horizontal deformation between the survey points 4 and 6 is 2289 mm (Table D.14). In 460 days, the length shortens of 99 mm, 4.3% of its initial length. The mean strain is $-4.3\%/460 \text{ days} = -0.009\%/day = 3.4\%/year$.

The initial horizontal deformation between the survey points 3 and 7 is 2565mm (Table D.14). In 460 days, the length shortens of 81mm, 3.2% of its initial length. The mean strain rate is $-3.2\%/460 \text{ days} = 0.007\%/day = 2.5\%/year$. There are differences between the measured and digitized horizontal deformations between the survey points 3 and 7. The differences are 20mm for 04.11.1954, 12mm for 06.09.1955, and 12mm for 07.02.1956. These differences come from the georeferencing of the map and the accuracy of the coordinates of every survey point.

The initial horizontal deformation between the survey points 1 and 2 is 2209 mm (Table D.14). In 460 days, the length shortens of 59mm, 2.7% of its initial length. The mean strain rate is $-2.7\%/460 \text{ days} = -0.006\%/day = 2.1\%/year$.

D.2.4 Oblique deformation

The initial oblique deformation between the survey points 1 and 4 is 2632 mm (Table D.15). In 460 days, the length shortens of 84mm, 3.2% of its initial length. The mean strain rate is $-3.2\%/460 \text{ days} = -0.007\%/day = 2.5\%/year$. There are differences between the measured and digitized oblique deformations between the survey points 1 and 4. The differences are 48mm for 04.11.1954, 51mm for 06.09.1955, and 50mm for 07.02.1956.

The initial oblique deformation between the survey points 2 and 6 is 2588 mm (Table D.16). In 460 days, the length shortens of 87mm, 3.4% of its initial length. The mean strain rate is $-3.4\%/460 \text{ days} = -0.007\%/day = 2.7\%/year$. There are differences between the measured and digitized oblique deformations between the survey points 2 and 6. The differences are 16mm for 29.08.1954, 27mm for 04.11.1954, 25mm for 06.09.1955, and 37mm for 07.02.1956.

i	T	ΔT	D_{64}	ΔD_{64}	$\Delta D_{64,cum}$	δD_{64}	$\delta \dot{D}_{64}$
[–]	[–]	[days]	[mm]	[mm]	[mm]	[%]	[%/day]
1	29.08.54	0	2312	0	0	0	0
2	04.11.54	0	2289	0	0	0	0
3	06.09.55	306	2233	-56	-56	-2.4	-0.008
4	07.02.56	154	2190	-43	-99	-1.9	-0.012

i	T	ΔT	D_{73}	ΔD_{73}	$\Delta D_{73,cum}$	δD_{73}	$\delta \dot{D}_{73}$
[–]	[–]	[days]	[mm]	[mm]	[mm]	[%]	[%/day]
1	29.08.54	0	-	0	0	0	0
2	04.11.54	0	2565	0	0	0	0
3	06.09.55	306	2511	-54	-54	-2.1	-0.007
4	07.02.56	154	2485	-26	-80	-1.0	-0.007

i	T	ΔT	D_{12}	ΔD_{12}	$\Delta D_{12,cum}$	δD_{12}	$\delta \dot{D}_{12}$
[–]	[–]	[days]	[mm]	[mm]	[mm]	[%]	[%/day]
1	29.08.1954	0	-	0	0	0	0
2	04.11.1954	0	2209	0	0	0	0
3	06.09.1955	306	2178	-31	-31	-1.4	-0.005
4	07.02.1956	154	2150	-28	-59	-1.2	-0.008

Table D.14 – Profile K_2 : Horizontal deformation determined from the digitisation from 29.08.1954 to 07.02.1956

i	T	ΔT	D_{14}	ΔD_{14}	$\Delta D_{14,cum}$	δD_{14}	$\delta \dot{D}_{14}$
[–]	[–]	[days]	[mm]	[mm]	[mm]	[%]	[%/day]
1	29.08.54	0	-	0	0	0	0
2	04.11.54	0	2632	0	0	0	0
3	06.09.55	306	2579	-53	-53	-2.0	-0.007
4	07.02.56	154	2548	-31	-84	-1.2	-0.008

Table D.15 – Profile K_2 : Oblique deformation determined from the digitization from 04.11.1954 to 07.02.1956

i	T	ΔT	D_{62}	ΔD_{62}	$\Delta D_{62,cum}$	δD_{62}	$\delta \dot{D}_{62}$
[–]	[–]	[days]	[mm]	[mm]	[mm]	[%]	[%/day]
1	29.08.54	0	2579	0	0	0	0
2	04.11.54	0	2588	0	0	0	0
3	06.09.55	306	2543	-45	-45	-1.7	-0.009
4	07.02.56	154	2485	-58	-103	-1.7	-0.011

Table D.16 – Profile K_2 : Oblique deformation determined from the digitisation from 29.08.1954 to 07.02.1956

Personal Declaration

I hereby declare that the submitted thesis is the result of my own independent work. All external sources are explicitly acknowledged in the thesis.

Sarah Morard
Sarah Morard
Zurich, 22.09.2020